Learning about the magnetar Swift J1834.9−0846 from its wind nebula

Jonathan Granot,[1][★] Ramandeep Gill,[1][★] George Younes,[2] Josef Gelfand,[3] Alice Harding,[4] Chryssa Kouveliotou[2] and Matthew G. Baring[5]

[1]*Department of Natural Sciences, The Open University of Israel, 1 University Road, PO Box 808, Raanana 4353701, Israel*
[2]*Department of Physics, The George Washington University, Washington, DC 20052, USA*
[3]*NYU Abu Dhabi, PO Box 903, New York, NY 10276, USA*
[4]*Astrophysics Science Division, NASA Goddard Space Flight Center, Greenbelt, MD 20771, USA*
[5]*Department of Physics and Astronomy, Rice University, MS-108, PO Box 1892, Houston, TX 77251, USA*

ABSTRACT
The first wind nebula around a magnetar was recently discovered in X-rays around Swift J1834.9−0846. We study this magnetar's global energetics and the properties of its particle wind or outflows. At a distance of ∼4 kpc, Swift J1834.9−0846 is located at the centre of the supernova remnant (SNR) W41 whose radius is ∼19 pc, an order of magnitude larger than that of the X-ray nebula (∼2 pc). The association with SNR W41 suggests a common age of ∼5–100 kyr, while its spin-down age is 4.9 kyr. A small natal kick velocity may partly explain why a wind nebula was detected around this magnetar but not around other magnetars, most of which appear to have larger kick velocities and may have exited their birth SNR. We find that the GeV and TeV source detected by *Fermi*/Large Area Telescope (LAT) and High Energy Spectroscopic System (H.E.S.S.), respectively, of radius ∼11 pc is most likely of hadronic origin. The dynamics and internal structure of the nebula are examined analytically to explain the nebula's current properties. Its size may naturally correspond to the diffusion-dominated cooling length of the X-ray emitting e^+e^- pairs. This may also account for the spectral softening of the X-ray emission from the nebula's inner to outer parts. The analysis of the X-ray synchrotron nebula implies that (i) the nebular magnetic field is $\gtrsim 11$ μG (and likely $\lesssim 30$ μG), and (ii) the nebula is not powered predominantly by the magnetar's quiescent spin-down-powered MHD wind, but by other outflows that contribute most of its energy. The latter are most likely associated with the magnetar's bursting activity, and possibly dominated by outflows associated with its past giant flares. The energy source for the required outflows cannot be the decay of the magnetar's dipole field alone, and is most likely the decay of its much stronger internal magnetic field.

Key words: diffusion – hydrodynamics – magnetic fields – stars: magnetars – stars: winds, outflows – ISM: supernova remnants.

1 INTRODUCTION

Pulsar wind nebulae (PWNe) can act as excellent calorimeters as they radiate over a broad energy range, from radio to TeV gamma-rays, and directly reflect the power injected by their central pulsars in the form of a relativistic MHD wind (see review by e.g. Gaensler & Slane 2006). Observations of the Crab nebula, a prototype of this class of objects, have provided invaluable insight into the physics of highly magnetized relativistic outflows and their interaction with the surrounding supernova remnant (SNR; in the case of the Crab the SNR is fragmented due to the Rayleigh–Taylor instability).

The defining characteristics of a PWN is a centrally filled nebula – sometimes referred to as a plerion, within the much larger SNR, along with power-law X-ray emission and flat radio spectrum (polarized in some cases). Its interior is filled with relativistically hot particles that cool both adiabatically as the nebula expands and radiatively by emitting synchrotron radiation in the relatively weak (typically between a few μG and ∼ mG, determined using various techniques; see for e.g. Reynolds, Gaensler & Bocchino 2012, and references therein) nebular magnetic field, and by inverse-Compton scattering on soft Cosmic Microwave Background (CMB) and/or infrared starlight photons. Its bolometric power is supplied by the loss of rotational kinetic energy ($\dot{E}_{\rm rot} = -I\Omega\dot{\Omega} = L_{\rm sd}$) of the spinning down pulsar (Gold 1969) with a broad range in X-ray

★ E-mail: granot@openu.ac.il (JG); rsgill.rg@gmail.com (RG)

efficiency $\eta_X = L_{X,\,PWN}/L_{sd} \sim 10^{-5} - 10^{-1}$ (e.g. see Kargaltsev & Pavlov 2008, for a catalogue of PWNe properties).

PWNe are typically observed down to $L_{sd} \sim 10^{33}$ erg s^{-1}. As pulsars spin down to longer periods, P, their rotational energy drops as $\dot{E}_{rot} \propto \dot{P}/P^3$, until they eventually become too dim to be detected in X-rays. Moreover, the pulsar's aging and spin down are also accompanied by a drop in the open magnetic-field line voltage $V_0 \propto |\dot{E}_{rot}|^{1/2}$ over which particles can potentially be accelerated. High angular resolution observations with *Chandra* have further revealed that PWNe that are still embedded in their host SNRs, thus forming a composite morphology, are typically associated with younger pulsars with high spin-down power $L_{sd} \gtrsim 10^{36.3}$ erg s^{-1}, whereas older pulsars typically power bow-shock PWNe. This is likely since for a given natal kick velocity the pulsar overtakes its SNR at a finite time (shortly after the SNR's velocity drops below the pulsar's velocity), so that younger pulsars are still inside their SNRs, which helps trap their wind and form a PWN, while older pulsars have already overtaken their SNRs, and thus form a bow shock instead of a PWN. Majority of the pulsars powering observed PWNe are known to be run-of-the-mill rotation-powered pulsars with equatorial surface dipole magnetic fields $B_s \sim 10^{12} - 10^{13}$ G, which begs the question: does the incidence of wind-nebulae continue up to the strongly magnetized neutron stars (NSs)?

Magnetars are slowly rotating ($P \sim 2$–12 s) NSs with super-QED (i.e. above $B_Q = m_e^2 c^3/e\hbar = 4.414 \times 10^{13}$ G) surface fields $B_s \sim 10^{14}$–10^{15} G as inferred from the magnetic dipole radiation (MDR) spin down, given in equation (11) (see review by e.g. Turolla, Zane & Watts 2015). Compared to rotation-powered pulsars with X-ray PWNe, the magnetars have similarly large period-derivatives $\dot{P} \sim 10^{-13}$–10^{-11} s s^{-1}, but due to slower rotation, having spin periods in the range $\sim 2 - 12$ s, their spin-down power is significantly less, $L_{sd} \sim 10^{30}$–10^{34} erg s^{-1}. Therefore, for comparable X-ray efficiencies η_X they would be dimmer and harder to detect, despite their small average characteristic ages ($\tau_c \sim 10^3$–10^5 yr; e.g. Olausen & Kaspi 2014), indicative of their youth, which might suggest otherwise. The empirical limit on L_{sd} mentioned above for Crab-like PWNe alone makes observations of X-ray wind-nebulae

around magnetars (hereafter magnetar wind nebulae – MWNe) challenging.

In contrast with rotation-powered pulsars, magnetars have a high quiescent X-ray luminosity (from the NS surface and/or magnetosphere) that is in excess of their spin-down power, $L_X \sim 10^{33}$–10^{36} erg s$^{-1} > L_{sd}$. Moreover, magnetars display a range of bursting activity, from the more common short bursts (lasting $\sim$0.1 s with observed luminosities $L \sim 10^{39}$–10^{41} erg s^{-1}) to the rare and highly super-Eddington giant flares (with an initial spike of luminosity $L \sim 10^{44}$–10^{47} erg s^{-1} over a fraction of a second, followed by a less luminous pulsating tail lasting hundreds of seconds). If the power in particle outflows is at least comparable to that in radiation, it is not inconceivable that the accumulated effect of many outbursts over the lifetime of magnetars, that have not yet escaped from their host SNRs, can give rise to a synchrotron bubble of relativistic particles. However, it has proven difficult to find wind-nebulae around magnetars, perhaps at least partly because most magnetars ($\sim$75 per cent) lack a clear SNR association (see Table 1). The status quo changed with the discovery of diffuse X-ray emission around one of the recently discovered magnetars (Younes et al. 2012).

Swift J1834.9−0846 (referred to as Swift J1834 hereafter) was discovered on 2011 August 7 by *Swift* and *Fermi* when it went into outburst (D'Elia et al. 2011; Guiriec, Kouveliotou & van der Horst 2011). Later observations by *RXTE* and *Chandra* established its magnetar nature by measuring a spin period $P \simeq 2.48$ s (e.g. Göğüş & Kouveliotou 2011) and period-derivative $\dot{P} \simeq 7.96 \times 10^{-12}$ s s^{-1} (Kuiper & Hermsen 2011; Kargaltsev et al. 2012). This implies an equatorial surface dipole magnetic-field strength $B_s \simeq 1.16 \times 10^{14}f^{-1/2}$ G [1.4×10^{14} G for $f = 2/3$, see equation (12) for the definition of f], spin-down power $L_{sd} \simeq 2.05 \times 10^{34}$ erg s^{-1}, and characteristic age $\tau_c \simeq 4.9$ kyr.

Swift J1834 is positioned very close to the geometrical centre of its host SNR W41, which might suggest that the magnetar has a small space velocity. Out of the total 29 magnetars (Olausen & Kaspi 2014), which includes 15 soft-gamma repeaters (SGR; including four candidate sources) and 14 anomalous X-ray pulsars (AXP, including two candidate sources), only seven, other than

Table 1. Magnetar–SNR associations.

Source	SNR	Distance (kpc)	$\theta_{1/2}$ SNR	Location	Off-centre angle	Association secure?	V_T (km s^{-1})	MWN	Refs.
SGR 0501+4516	HB9	0.8 ± 0.4	62.5 arcmin	E	$\sim$80 arcmin	No	$(1.7$–$4.3)\times 10^3$	No	1, 2, 3, 4
SGR 0526−66	N49	$\sim$50	$\sim$35 arcsec	E	22 arcsec	No	$\sim$1100	No	5, 6, 7
SGR 1627−41	G337.0+0.1	11.0 ± 0.3	45 arcsec	E	105 ± 26 arcsec	No	$\sim 10^3$	No	8, 9, 10, 11
SGR 1935+2154	G57.2+0.8	–	6 arcmin	C	–	Yes	–	Maybe	12, 13
1E 1547.0−5408	G327.24−0.13	6 ± 2	2 arcmin	C	$\lesssim 13$ arcsec	Yes	280^{+130}_{-120}	No	14, 15
1E 1841−045	Kes 73	$\sim$8.5	2.5 arcmin	C	-	Yes	$\lesssim 160$	No	16, 17, 18
1E 2259+586	CTB 109	3.2 ± 0.2	18 arcmin	OC	$\sim$4 arcmin	Yes	$\sim$157	No	19, 20, 21
AX J1845.0−0258	G29.6+0.1	$\sim$8.5	2.5 arcmin	OC	$\lesssim 40$ arcsec	Yes	–	No	22, 23, 24, 25
CXOU J171405.7**	CTB 37B	$\sim$13.2	2.5 arcmin	OC	2.17 arcmin	Yes	$\sim 10^3$	No	26, 27, 28
PSR J1622−4950	G333.9+0.0	$\sim$9	–	–	–	No	–	No	29, 30
PSR J1846−0258	Kes 75	$6.0^{+1.5}_{-0.9}$	1.75 arcmin	C	<1 arcmin	Yes	–	Yes*	31, 32, 33

Notes. $\theta_{1/2}$ is the angular radius of the SNR. E – source near the edge of the SNR, C – source near the centre of the SNR, OC – source slightly off-centred. *PSR J1846−0258 is a 0.326 s rotation-powered pulsar, but with a high surface dipole field $B_s = 4.9 \times 10^{13}$ G. The classification of this source as a magnetar, due to an episode of bursting activity, is not yet clear. ** Source name: CXOU J171405.7−381031. Refs. – (1) Barthelmy et al. (2008); (2) Göğüş et al. (2010); (3) Gaensler & Chatterjee (2008); (4) Leahy & Tian (2007); (5) Mezets et al. (1979); (6) Cline et al. (1980); (7) Park et al. (2012); (8) Kouveliotou et al. (1998); (9) Watcher et al. (2004); (10) Corbel et al. (1999); (11) Sarma et al. (1997); (12) Israel et al. (2016); (13) Hurley-Walker et al. (2009); (14) Camilo et al. (2007); (15) Deller et al. (2012); (16) Vasisht & Gotthelf (1997); (17) Tendulkar (2013); (18) Tian & Leahy (2008); (19) Fahlman & Gregory (1981); (20) Tendulkar et al. (2013); (21) Kothes & Foster (2012); (22) Gotthelf & Vasisht (1998); (23) Gaensler et al. (1999); (24) Vasisht et al. (2000); (25) Torii et al. (1998); (26) Aharonian et al. (2008); (27) Halpern & Gotthelf (2010); (28) Tian & Leahy (2012); (29) Levin et al. (2010); (30) Anderson et al. (2012); (31) Gotthelf et al. (2000); (32) Leahy & Tian (2008b); (33) Gelfand et al. (2014); For further details, see the magnetar catalogue (Olausen & Kaspi 2014): http://www.physics.mcgill.ca/pulsar/magnetar/main.html
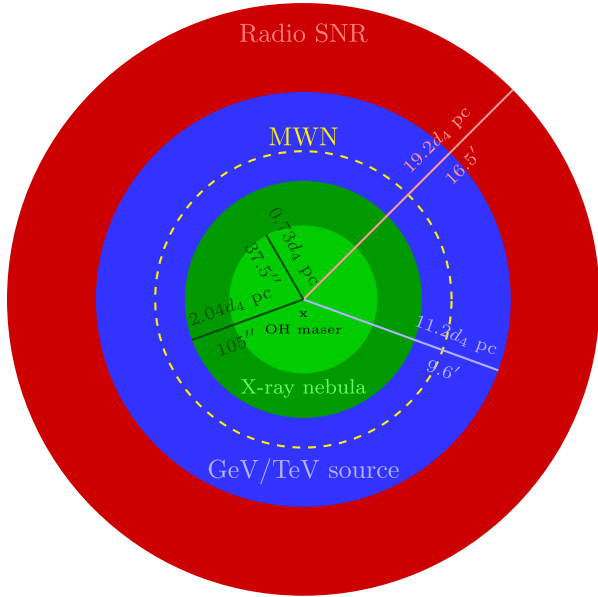
Figure 1. Physical setup of the system showing the radio SNR W41, GeV/TeV source detected by H.E.S.S and *Fermi*, OH maser emission near the centre of the GeV/TeV region, and (inner and outer) X-ray bright region of the MWN powered by Swift J1834. This figure is not to scale, and for simplicity, the different emission regions have been approximated here by circular regions with approximate radial extents shown in the figure; the true geometry is irregular.

Swift J1834, have secure SNR associations. In all of these cases, the magnetar (or candidate source) is positioned very close to the centre of the SNR, and has a low measured transverse velocity $<400\,\mathrm{km\,s^{-1}}$ (e.g. Gaensler et al. 2001). We list the magnetar–SNR associations, along with the distance to the SNR, its angular radius ($\theta_{1/2}$), the location of the magnetar with respect to the SNR centre and its off-centre angle, the measured or inferred transverse velocities of magnetars, and whether they power an MWN in Table 1.

By analysing two deep *XMM–Newton* observations post-outburst of Swift J1834 and its extended X-ray emission, the existence of a first ever wind-nebula around a magnetar was confirmed by Younes et al. (2016). They have dismissed the dust-scattering halo interpretation (e.g. Esposito et al. 2013), based on the fact that the X-ray flux of the diffuse emission has remained almost unchanged since the 2011 outburst and its spectrum is inconsistent with the much softer spectrum expected from scattering by dust. Fig. 1 summarizes the measured sizes of the entire system. The spectral appearance of the X-ray nebula changes with distance from the central magnetar (Younes et al. 2016), where the inner X-ray nebula, with angular size 37.5 arcsec and radial extent $R_{\mathrm{X,\,in}} = 0.73d_4$ pc (for a distance of $d = 4d_4$ kpc to the source), is spectrally harder than the outer X-ray nebula (105 arcsec and $R_{\mathrm{X}} = 2.04d_4$ pc). The size of the overlapping GeV/TeV source observed by *Fermi*/Large Area Telescope (LAT) and High Energy Spectroscopic System (H.E.S.S.) is 9.6 arcmin or $R_{\mathrm{GeV/TeV}} = 11.2d_4$ pc, and the radio SNR extends to an angular size 16.5 arcmin with $R_{\mathrm{SNR}} = 19.2d_4$ pc.

The various symbols that appear in the paper are collected in Table 2 for convenience.

Plan of the paper

The observation of a wind-nebula around Swift J1834 presents a rare opportunity to study the global energetics of magnetars and

Table 2. Various symbols with their meanings that appear in this work.

Symbol	Meaning
a	MWN radial expansion temporal power-law index
α	Inverse of magnetic-field decay power-law index
B	Nebular magnetic field
B_0	Initial surface dipole magnetic field
B_s	Equatorial surface dipole magnetic field
B_{int}	Internal magnetic field inside the magnetar
β_{TS}	The flow's v/c behind the wind termination shock
χ	MWN compression ratio at reverse shock passage
d	Distance to the source from observer
E	Total energy in the MWN
E_0	Initial rotational kinetic energy injected by proto-NS
E_B	Magnetic energy of the X-ray nebula
$E_{B,\,\mathrm{dip}}$	Energy in magnetar's dipolar magnetic field
$E_{B,\,\mathrm{int}}$	Energy in magnetar's internal magnetic field
E_{f}	Total energy in the nebula after crushing
E_γ	Photon energy
E_{i}	Total energy in the nebula before crushing
E_{inj}	Spin-down energy injected into MWN
E_{p}	Proton energy
E_{rot}	Rotational kinetic energy
E_{SN}	Supernova energy
ϵ_{e}	Ratio of total energy in power-law electrons to that in the matter component of MHD wind
ϵ_{X}	Ratio of energy in X-ray radiating electrons to total energy in power-law electrons
η_{X}	X-ray efficiency of the nebula
f	Parameter to distinguish between vacuum and force-free spin-down law
g	Ratio of long-term mean energy injection rate into the nebula by the magnetar to L_{sd}
γ_{c}	Lorentz factor of electrons cooling at the dynamical time
γ_{e}	Lorentz factor of electrons
γ_{max}	Maximal electron Lorentz factor, $eV_0/m_{\mathrm{e}}c^2$
Γ	Photon spectral index (whole nebula)
Γ_{in}	Photon spectral index (inner nebula)
k	ISM density radial power-law index
L_{sd}	Spin-down power
L_0	Initial spin-down power
l_{adv}	Characteristic advection length scale
l_{diff}	Characteristic diffusion length scale
L_{GeV}	GeV luminosity
L_{TeV}	TeV luminosity
L_{X}	(0.5–10 keV, *XMM*) X-ray luminosity of the entire nebula
$L_{\mathrm{X,\,in}}$	(0.5-30 keV, *XMM*+NuSTAR) X-ray luminosity of the inner nebula
$L_{\mathrm{X,\,tot}}$	(0.5–30 keV, *XMM*+NuSTAR) X-ray luminosity of the entire nebula
M_{ej}	SN ejecta mass
n	Braking index (assuming constant B_s)
n'	Measured braking index
n_{ext}	Number density of ISM gas
N_{HI}	Neutral hydrogen column density
n_{p}	Proton power-law distribution
ν_{i}	Characteristic synchrotron frequency corresponding to electron Lorentz factor γ_{i}
Ω	Spin angular frequency
Ω_0	Initial spin angular frequency
s	Electron distribution power-law index
P	Spin period
P_0	Initial spin period
p_{i}	Total pressure inside the nebula before crushing
p_{f}	Total pressure inside the nebula after crushing

Table 2 – *continued*

Symbol	Meaning
p_S	Central pressure interior to a Sedov blast wave
r	Radial distance from the centre of the nebula
R	Radius of MWN
R_0	Radius of MWN at time t_0
r_{adv}	Advection distance of nebular flow
R_b	Radius below which the nebular flow is in steady-state
R_c	Density core crossing radius of MWN outer shell
$r_{c, adv}$	Max. advection distance of particles over their synchrotron cooling times
$r_{c, diff}$	Max. diffusion distance of particles over their synchrotron cooling times
R_f	Radius of MWN after crushing
$R_{GeV/TeV}$	Radius of the GeV/TeV energy region
R_i	Radius of MWN before crushing
R_{NS}	Neutron star radius
R_{SNR}	Radius of the SNR W41
R_{ST}	Radius of SNR at Sedov–Taylor onset
r_*	Radius beyond which diffusion dominates over advection
$R_{TS, p}$	Magnetars wind termination shock radius
R_X	Radius of the entire X-ray nebula
$R_{X, in}$	Radius of the inner X-ray nebula
ρ_{ext}	Mass density of the surrounding ISM
σ	Magnetization of nebular plasma
σ_e	Magnetization of power-law electrons
$\tilde{t}$	System's age t normalized by t_0
$\hat{t}$	System's age t normalized by t_{ST}
t_0	Initial spin-down time
t_B	Characteristic initial magnetic-field decay time
t_c	Density core crossing time of MWN outer shell
τ_c	Characteristic spin-down age
t_{SNR}	Age of the SNR
t_{ST}	Sedov–Taylor onset time
t_{syn}	Synchrotron cooling time of electrons
θ_X	Mean angular size of X-ray nebula
V_0	Polar cap voltage difference
ξ	Ratio of the total energy in electrons to the energy in the X-ray emitting electrons
ξ_{in}	ξ derived for the inner nebula
ζ	Ratio of particle deflection length to its Larmor radius

properties of their particle wind or outflows, both in quiescence and during outbursts. In this work we consider in detail the implications of the discovery of this first-confirmed MWN. Here, we briefly outline the structure of the paper along with our main line of reasoning for each part.

In Section 2 we consider the implications of the association of Swift J1834 with the SNR. In particular, the magnetar's systemic velocity on the plane of the sky is constrained to be at most tens of km/s. Its age is more uncertain (Section 2.1) and depends mainly on the uncertain external density (and to a lesser extent on the somewhat uncertain SNR energy), but for reasonable parameter values it is in the range $5\,\mathrm{kyr} \lesssim t_{SNR} \lesssim 100\,\mathrm{kyr}$. Reconciling the upper age estimate ($\sim100\,\mathrm{kyr}$) of the radio SNR with the SGR's spin-down age of $\tau_c \simeq 4.9\,\mathrm{kyr}$ (Section 2.2) suggests either a braking index of $n \simeq 1.1$ (corresponding to an initial surface dipole field well below its current value) or a braking index of $n \approx 3$ but with a current value of $\dot{P}$ that is anomalously high, well above its long-term mean value (by a factor of ~20). The evolution of the spin period and braking

index for an evolving surface dipole field strength is considered in detail in Appendix A.

In Section 3 we consider the energetics of the X-ray nebula. First, we use its observed size (R_X) and luminosity (L_X) to constrain the magnetic-field strength B within the X-ray nebula, assuming that the observed X-rays are synchrotron emission. From regular equipartition arguments we find $B \sim (4-30)\sigma_e^{2/7}\,\mu\mathrm{G}$, where $\sigma_e = \frac{2}{3}\sigma/\epsilon_e$ is the ratio of energy in the magnetic field and in the X-ray emitting power-law electron energy distribution that holds a fraction ϵ_e of the total energy in particles, and σ is the magnetic to particle enthalpy density ratio in the MWN. For PWNe traditional 1D modelling typically implies $10^{-3} \lesssim \sigma \lesssim 10^{-2}$ (e.g. Kennel & Coroniti 1984; De Jager & Harding 1992; Hillas et al. 1998; Meyer, Horns & Zechlin 2010), while more recent 2D or 3D could allow for slightly higher mean values of $10^{-2} \lesssim \sigma \lesssim 10^{-1}$ in the nebula (e.g. Mizuno et al. 2011; Porth, Komissarov & Keppens 2013, 2014). Secondly, by assuming that the maximal electron energy cannot exceed that corresponding to the maximal voltage across the magnetar's open magnetic-field lines (e.g. De Jager & Harding 1992), we derive a more robust limit (independent of σ or the global electron energy distribution) of $B \gtrsim 11\,\mu\mathrm{G}$, which corresponds to a lower limit on the MWN magnetic energy that scales with its volume (i.e. as the cube of its radius). Moreover, our results imply that for any value of σ, the long-term time averaged energy output from the SGR into the MWN significantly exceeds (by a factor of $g > 3.1$) its current spin-down power L_{sd}. The most likely candidates for such energy injection from the SGR into the MWN are the outflows associated with its bursting activity.

The MWN's dynamical evolution is outlined in Section 4 and related to the energy injection by the magnetar's quiescent rotation-powered MHD wind, where some of the details are expanded upon in Appendix B. The MWN's dynamics and energy injection by the wind together determine the MWN's current energy, considering adiabatic evolution of the electrons. The additional effects of radiative energy losses together with adiabatic cooling or heating are briefly considered in Appendix C, and neglecting them results in a fairly robust upper limit on the MWN's current energy.

The internal structure within the MWN is considered in Section 5, in order to calculate the resulting synchrotron cooling length. We find that there is an inner quasi-steady-state region (discussed in Section 5.1) and an outer uniformly expanding region (Section 5.2). This structure is discussed in the context of the observed spectral softening within the X-ray nebula with distance from the magnetar (Section 5.3). Advection alone generally leads to a sharper spectral softening with radius than observed. Therefore, we also consider the effects of diffusion (Section 5.4) and find that diffusion dominates over advection throughout most of the nebula. Moreover, the effects of diffusion can likely account for the more gradual observed spectral softening and naturally explain the nebula's observed size.

In Section 6 we show that the X-ray emitting e^+e^- pairs are fast cooling, which allows us to write their detailed energy balance. This results in a lower limit on $g = \langle\dot{E}\rangle/L_{sd} \gtrsim 3.1(1+\sigma)/\sigma$, which is the ratio of the magnetar's long-term mean energy output in outflows (quiescent MHD wind + sporadic outbursts), $\langle\dot{E}\rangle$, to its spin-down luminosity. This clearly implies that the MWN is not powered predominantly by the magnetar's spin-down-powered wind, and an alternative dominant energy source is required, most likely the decay of the magnetar's magnetic field. We show that the decay of its dipole field alone is not enough, and a significantly larger (by a factor of $\sim10^2$–10^3) energy reservoir is needed. The most plausible candidate is the magnetar's internal magnetic field, which has to be $\gtrsim 10 - 30$ times larger than its dipole field. Finally, by assuming

a maximum allowed initial internal field strength (on theoretical grounds) of $B_{\rm int,\,max} \sim 10^{16}$–$10^{16.5}$ G we obtain an upper limit on $g \lesssim 5 \times (10^2$–$10^3)$.

In Section 7 we consider the possible origin of the GeV/TeV emission observed by *Fermi*/LAT and H.E.S.S. In Section 7.1 we consider the possibility of a hadronic origin for the GeV/TeV emission. While inverse-Compton emission by electrons in the MWN is energetically very challenging, we find a much more plausible and energetically reasonable alternative to be the decay of neutral pions that are produced by the interaction of cosmic rays (CR) accelerated in the shock driven by the SNR into the external medium, with nuclei in the nearby giant molecular cloud (GMC). In Section 7.2, we consider the possibility of inverse-Compton emission by relativistic electrons in the MWN that upscatter seed photons from the NIR Galactic background and the CMB. For Galactic NIR seed photons we find it extremely difficult to account for the observed GeV/TeV luminosity. For CMB seed photons it is also very difficult to account for the GeV/TeV luminosity, and moreover, together with the power-law MWN electron energy distribution (as reflected by their X-ray synchrotron emission) one would expect a much broader spectral peak at TeV energies, which is hard to reconcile with the *Fermi*/LAT and H.E.S.S. observations. Therefore, we find this option implausible. Finally, we also consider emission from relativistic non-thermal bremsstrahlung from electrons accelerated at the SNR forward shock.

Our conclusions are discussed in Section 8. Our main findings are that the MWN is powered predominantly by outflows from the magnetar, whose main energy source is most likely the decay of its strong internal magnetic field. These conclusions became possible because of the discovery of this first MWN. The outflows from the magnetar accumulate inside the MWN, which therefore serves as a calorimeter that helps us study the system's history.

2 IMPLICATIONS OF THE ASSOCIATION WITH THE SNR

The location of Swift J1834 at the very centre of the SNR W41 strongly supports their association. Moreover, it can also constrain the SGR's proper velocity on the plane of the sky, $v_{\perp,\rm SGR}$. Its location can be constrained to be $\lesssim (0.05 - 0.1)R_{\rm SNR}$ from the centre of the SNR, which for an SNR/SGR age of $t_{\rm SNR}$ implies $v_{\perp,\rm SGR} \lesssim (30 - 60)d_4(t_{\rm SNR}/10^{4.5}\,{\rm yr})^{-1}\,{\rm km\,s^{-1}}$. Below we discuss how $t_{\rm SNR}$ may be estimated, and how it can be reconciled with the SGR's measured spin-down age.

2.1 Age of SNR W41

By using the Very Large Array Galactic Plane Survey (VGPS), Tian et al. (2007) found strong evidence of H I emission at 1420 MHz associated with the SNR W41 in the radial velocity range of 53–63 km s^{-1}. The SNR is also coincident with a GMC positioned just behind the SNR, as inferred from the ^{13}CO emission lines, in the radial velocity range of 61–66 km s^{-1}, that trace molecular hydrogen H$_2$ (Tian et al. 2007). For a mean radial velocity of 58 km s^{-1}, galactic longitude of $l = 23°.24$, and under the assumption of a flat rotation curve with $v_\odot \simeq 220\,{\rm km\,s^{-1}}$ at $d_\odot \simeq 8.5$ kpc, we find a galactocentric distance to SNR W41 of $d_{\rm G} \simeq 5.1$ kpc, which corresponds to a distance of $d \simeq 3.97$ kpc or $d \simeq 11.65$ kpc. The H I absorption spectrum of SNR W41 suggests a tangent point velocity $V_t \simeq 112\,{\rm km\,s^{-1}}$ and constrains W41 to be on the near side of the distance ambiguity (Leahy & Tian 2008a). It has an average angular diameter of 33 arcmin (Tian et al. 2007) which gives a

radial extent of $R_{\rm SNR} \simeq 19.2d_4$ pc, for a distance of $d = 4d_4$ kpc to the source. The H I column density maps from the VGPS suggest values in the range $1 \lesssim N_{\rm HI,21} \lesssim 2$ in the surrounding GMC, where $N_{\rm HI,21} = N_{\rm HI}/(10^{21}\,{\rm cm}^{-2})$. Moreover, there is a significant deficit of up to $\Delta N_{\rm HI,21} \lesssim 1$ in the exact location of the SNR and with its exact shape, which strongly suggests that it originates from the reduction in the $N_{\rm HI}$ column density in the region now occupied by the SNR that was previously part of the surrounding GMC. Therefore, the maximum reduction in column density due to the SNR can be used to estimate the corresponding mean number density in the region that it swept-up within the GMC, $n_{\rm HI} \sim \max(\Delta N_{\rm HI})/(2R_{\rm SNR}) \sim 8.4d_4^{-1}\,{\rm cm}^{-3}$ (see also Tian et al. 2007).

Although the ISM particle density is dominated by the H I component, an estimate of the true total mass density $\rho_{\rm ext}$ should account for the presence of the GMC. Therefore, we express the mass density of the ISM using $\rho_{\rm ext} = \mu n_{\rm HI} m_{\rm p}$, where $m_{\rm p}$ is the proton mass and μ is the mean number of nucleons per neutral hydrogen atom in the ISM. One might expect $\mu \approx 2$ when accounting for helium and metals, in addition to the fact that some of the hydrogen is ionized (H II) or molecular (H$_2$), which would give $n_{\rm ext} = \rho_{\rm ext}/m_{\rm p} \approx 17(\mu/2)d_4^{-1}\,{\rm cm}^{-3}$. The age of the SNR can be estimated from the Sedov–Taylor self-similar solution

$$R(t) = 1.17 \left(\frac{E_{\rm SN}t^2}{\rho_{\rm ext}} \right)^{1/5}, \tag{1}$$

which gives

$$
\begin{aligned}
t_{\rm SNR} &= 97 E_{\rm tot,51}^{-1/2} \left(\frac{n_{\rm ext}}{17\,{\rm cm}^{-3}} \right)^{1/2} d_4^{5/2}\,{\rm kyr}, \\
&= 23.6 E_{\rm tot,51}^{-1/2} n_0^{1/2} d_4^{5/2}\,{\rm kyr}, \\
&= 5.3 E_{\rm tot,52.3}^{-1/2} n_0^{1/2} d_4^{5/2}\,{\rm kyr}, \tag{2}
\end{aligned}
$$

where $n_0 = n_{\rm ext}/(1\,{\rm cm}^{-3})$ [this fiducial value of $n_{\rm ext}$ is chosen due to the inherent uncertainty in determining the true ISM density, which could be in the range $n_{\rm ext} \sim 0.1$–a few $\times 10\,{\rm cm}^{-3}$ (also see below).], $E_{\rm tot,\,51} = E_{\rm tot}/(10^{51}\,{\rm erg})$, and $E_{\rm tot,\,52.3} = E_{\rm tot}/(2 \times 10^{52}\,{\rm erg})$, where $E_{\rm tot}$ is the total energy injected into the system. The motivation for $E_{\rm tot} \sim 2 \times 10^{52}$ erg comes from energy injection by a millisecond magnetar at early times (as explained in more detail below). An estimate of $t_{\rm SNR} \sim 100$ kyr was derived by Tian et al. (2007) ($\sim$60 kyr assuming a Sedov–Taylor expansion, and $\sim$200 kyr accounting for radiative cooling of the SNR). Although according to Cioffi, McKee & Bertschinger (1988), the SNR becomes radiative with its dynamical evolution described by the *pressure-driven snowplow* (PDS) phase at $t_{\rm PDS} = 13.4 E_{\rm SN,51}^{3/14} n_0^{-4/7}$ kyr, the age derived above for the Sedov–Taylor phase serves as a robust lower limit.

The single model parameter with the largest uncertainty affecting the derived age is the density of the external medium $\rho_{\rm ext}$. Although other astronomical methods can be employed to estimate its true value, other than what is used in this work, they all can provide conflicting results (see e.g. Castro & Slane 2010). For instance, the density of the shocked electrons behind the forward blast wave, which are emitting thermal X-rays, can be obtained from spectral fits that yield the volume emission measure, defined as $E.M. \approx n_e^2 V f_V/(4\pi d^2)$ where n_e is the density of the shocked electrons, f_V is the volume filling factor, V is the volume and d is the distance to the source. Alternatively, if the SNR forward blast wave is directly interacting with a neighbouring GMC, the possibility of which is confirmed by the observation of shock-excited OH (1720 MHz) maser emission (Frail et al. 1996; Frail, Claussen & Méhault 2013), then CR protons accelerated at the shock front can

give rise to detectable GeV/TeV radiation. The high-energy flux can then be used to constrain the density of the target protons (see Section 7). However, care must be taken as for the interpretation of such a density estimate since it only reflects the volume-averaged density. Molecular clouds are known to be clumpy with typically large density contrasts ($\rho_c/\rho_{ic} > 10^3$) between the clumpy (ρ_c) and the inter-clump medium (ρ_{ic}), such that the average density is $\langle\rho\rangle = \rho_c[f_V + (\rho_{ic}/\rho_c)(1-f_V)]$, where $f_V \sim 0.02 - 0.08$ (e.g. Blitz 1993) is the volume filling factor of the clumps. For the SNR dynamics the relevant external density is $\rho_{ext} \approx \rho_{ic}$ (since dense clumps are hardly accelerated by the SNR shock and instead penetrate through it like bullets). Therefore, usage of the (generally larger) average density $\langle\rho\rangle$ for calculating the SNR dynamics might offset its size or age estimates considerably. In what follows, we continue to parametrize the external density in terms of $n_0 = n_{ext}/(1\,\mathrm{cm}^{-3})$ where $n_{ext} = \rho_{ext}/m_p$.

2.2 Characteristic age and braking index of Swift J1834

The spin-down law is often expressed as a power law with a general 'braking index' n ($n = 3$ for magnetic dipole braking),

$$\dot{P} \propto P^{2-n}. \tag{3}$$

For magnetic dipole braking this corresponds to the assumption that the strength of the dipole magnetic field and the moment of inertia remain constant over time. Integrating this equation over time gives the time evolution of the spin period

$$P(t) = P_0\left(1 + \frac{t}{t_0}\right)^{\frac{1}{(n-1)}}, \tag{4}$$

where P_0 is the initial spin period, and t_0 is the initial spin-down time. This provides the current age, t, in terms of t_0, P and $\dot{P}$:

$$t = \frac{P}{(n-1)\dot{P}} - t_0 = \frac{2\tau_c}{(n-1)} - t_0, \tag{5}$$

where $\tau_c \equiv P/2\dot{P}$ is the usual characteristic spin-down age. One finds the relation

$$t_0 = \frac{P_0}{(n-1)\dot{P}}\left(\frac{P}{P_0}\right)^{2-n}, \tag{6}$$

which provides t_0 given the current measured values of P and $\dot{P}$, for assumed values of n and P_0.

For $t \gg t_0$, the characteristic spin-down age can be obtained from the measured spin properties, and in the present case, for $n = 3$, it is $t \approx \tau_c = 4.9$ kyr.

If the true age of Swift J1834 is significantly larger than τ_c (as suggested by the estimated age of the SNR $t_{SNR} \sim 100$ kyr), then one way in which this could be reconciled is if $n \approx 1$. This could occur, e.g. if a particle-dominated wind opens up dipole magnetic-field lines, thus increasing the resulting field strength at the light cylinder and enhancing the spin-down torque (e.g. Harding, Contopoulos & Kazanas 1999; Tong et al. 2013; Tong 2016). However, while the likely energy source for driving such a wind is the magnetar's magnetic-field decay, it is not clear what mechanism would naturally produce such a particle-dominated wind. What is more, its required power needs to exceed the current inferred spin-down power L_{sd} by a factor of $g \sim 50$–5000 (Tong 2016), so it would by far dominate the energy injection into the MWN.

Moreover, this has serious implications for the magnetic field $B_{LC} = B(R_{LC})$ at the light cylinder $R_{LC} = c/\Omega$. If the spin-down torque is indeed due to rotational energy loss to Poynting flux of an outgoing MHD wind, then the spin down would be the same as

for magnetic dipole braking with an effective surface dipole field strength of $B_{eff} = (R_{LC}/R_{NS})^3 B_{LC} \propto \sqrt{P\dot{P}}$ that satisfies

$$\dot{P} \propto P^{2-n} \propto B_{eff}^2 P^{-1}, \tag{7}$$

and therefore

$$B_{eff}(t) = B_0\left(\frac{P}{P_0}\right)^{\frac{3-n}{2}} = B_0\left(1 + \frac{t}{t_0}\right)^{\frac{3-n}{2(n-1)}}. \tag{8}$$

For the above-mentioned model where $n \approx 1$ we can see that B_{eff} grows as a high power of time t. However, there is a limited dynamical range over which a particle wind can open up the dipole field lines, corresponding to a field-opening radius in the range $R_{NS} < r_{open} < R_{LC}$, or a factor of R_{LC}/R_{NS} which is $\approx 10^4$ for Swift J1834. Therefore, such a behaviour could last only up to a factor of $\sim(R_{LC}/R_{NS})^{2(n-1)/(3-n)}$ in time, between an age of t_0 and the current age t. For our case and $n \approx 1$ this corresponds to a current age satisfying $t/t_0 \sim 10^{4(n-1)}$ or ~ 2.6 for $n \approx 1.1$ [which would correspond to a true age of $t \approx \tau_c 2/(n-1) \sim 100$ kyr].

The current P and $\dot{P}$ values of Swift J1834 imply a surface magnetic field $B_{eff}(t) = 1.16 \times 10^{14} f^{-1/2}$ G. A braking index $n = 1.1$ would suggest a growing effective magnetic field B_{eff} over time, so that its value at birth should have been much lower, $B_{eff,0} = 6.2 \times 10^{11} f^{-1/2} P_{0,-2}^{0.95}$ G where $P_{0,-2} = P_0/(10^{-2}\,\mathrm{s}) = P_0/(10\,\mathrm{ms})$. One way of interpreting this increase in B_{eff} is that it indeed reflects a growing surface dipole field, which is not easy to account for on physical grounds (see however Muslimov & Page 1996; Ho 2015; Marshall et al. 2016). Since the magnetars' bursting activity and high X-ray luminosity $L_X > L_{sd}$ are thought to be powered by the decay of their magnetic field, this would imply a gradual emergence of a much stronger internal magnetic field, from deep within the NS, out to its surface. This may potentially produce, at least temporarily, a net growth of the surface dipole magnetic field, if some of the strong internal toroidal field is converted to an external poloidal field faster than the latter decays. Axisymmetric magnetic-field stability analysis (see equation 91) yields an internal field strength $B_{int,0} \lesssim 1.6 \times 10^{14} f^{-1/4} P_{0,-2}^{0.475}$ G, which corresponds to the effective surface dipole field $B_{eff,0}$. This estimate is consistent with the current surface dipole field, as inferred from P and $\dot{P}$, and provides further support to the notion of internal field transport to the surface. Still, the underlying mechanism for growth of surface dipole field is uncertain; however, we briefly mention possible channels below.

Now let us consider specifically the case of magnetic dipole braking, which corresponds to $n = 3$ and for which the spin-down power is given by (e.g. Spitkovsky 2006)

$$L_{sd} = f\frac{B_s^2 R_{NS}^6 \Omega^4}{c^3}, \quad f = \begin{cases} \frac{2}{3}\sin^2\theta_B & \text{in vacuum} \\ \\ 1 + \sin^2\theta_B & \text{force free} \end{cases} \tag{9}$$

where $I \simeq 10^{45}\,\mathrm{g\,cm^2}$, $R_{NS} \simeq 10^6$ cm and $\Omega = 2\pi/P$ are the NS's moment of inertia, radius and angular spin frequency, respectively, θ_B is the inclination angle between the magnetic dipole axis and the rotational axis, and B_s is the equatorial surface dipole magnetic-field strength, whose initial value is $B_0 = 10^{14} B_{14}$ G. By comparing the loss of rotational kinetic energy with spin-down power, $-I\Omega\dot{\Omega} = L_{sd}$, and initial spin-down time is given by

$$t_0 = \frac{Ic^3}{2f\Omega_0^2 R_{NS}^6 B_0^2} = 3.4 \times 10^4 \frac{P_{0,-3}^2}{f B_{14}^2}\,\mathrm{s}, \tag{10}$$

where $\Omega_0 = 2\pi/P_0$ is the initial angular spin frequency, and $P_{0,-3} = P_0/(10^{-3}\,\mathrm{s}) = P_0/(1\,\mathrm{ms})$. However, even in this case the spin-down age only reflects the current value of $\dot{P}$, which may be unusually

higher than its long-term mean value, which may account for a true age $t \gg \tau_c$. Several other magnetars have shown large fluctuations in $\dot{P}$ before and after bursting episodes. For example, the average spin-down rate of SGR 1806 − 20 increased by a factor of ∼6 in the 12 yr period prior to the giant flare in 2004 December, with large fluctuations in $\dot{P}$ observed in the months leading up to the flare (Woods et al. 2007; Younes et al. 2015). In the case of SGR 1900 + 14, which emitted a giant flare in 1998 August, the post-flare $\dot{P}$ was higher by a factor of ∼4 compared to the pre-flare long-time average spin-down rate (Woods et al. 2002). Finally, Gavriil & Kaspi (2004) reported a factor of ∼12 increase in the spin-down rate of AXP 1E 1048.1 − 5937 over a time-scale of weeks to months. Such a sudden increase (decrease) in $\dot{P}$ is likely due to the formation (destruction) of magnetospheric currents that enhance the magnetic field near the light cylinder to values above that due to the magnetar's dipole field component that is supported by currents inside the NS. In such a case the usual value of B_s that is inferred from P and $\dot{P}$ is an overestimate of the true surface dipole field strength. Such changes in $\dot{P}$ may also be associated with outflows accompanying the magnetar's bursting activity. Moreover, the cumulative effect of such irregular $\dot{P}$ changes may modify the spin-down histories of magnetars and make them correspondingly irregular and less predictable compared to regular pulsars.

The current surface magnetic field is given by the familiar expression

$$B_s = \sqrt{\frac{I c^3 P \dot{P}}{4\pi^2 f R_{NS}^6}} = 2.61 \times 10^{19} R_6^{-3} \sqrt{\frac{I_{45}}{f}} \sqrt{P_s \dot{P}} \text{ G}, \quad (11)$$

where $I = 10^{45} I_{45}$ g cm^2, $R_{NS} = 10^6 R_6$ cm and $P_s = P/(1 \text{ s})$.

In Appendix A we show that for a more general equation for the magnetar's braking, of the form $\dot{P} \propto B_s^2 P^{2-n}$, where the magnetic field evolves in time as $B_s \propto t^{-1/\alpha}$ at times $t > t_B$, where t_B is the characteristic field growth/decay time-scale, the observable braking index is given by $n' = n + \Delta n$, where the difference from n that appears in this formula is $\Delta n = 2\dot{B}_s P/(B_s \dot{P})$. For $\alpha < 2$ the field decays rapidly enough that spin-down freezes out and the rotation period approaches a constant value at late times (Colpi, Geppert & Page 2000; Dall'Osso, Granot & Piran 2012), in which case the measured braking index would grow at late times as $n' \propto t^{(2-\alpha)/\alpha}$. For $\alpha > 2$ the observed braking index approaches a constant value of $n'_\infty = (n\alpha - 2)/(\alpha - 2)$.

For magnetic dipole braking that is preferred on theoretical grounds, $n = 3$, resulting in $n'_\infty = (3\alpha - 2)/(\alpha - 2)$ and $\alpha = (2n'_\infty - 2)/(n'_\infty - 3)$, which is similar to equation (8) when n is replaced by n'_∞. This may be able to account for the observed values of $n' < 3$, even for pure magnetic dipole braking. While this still requires $\alpha < 0$, i.e. a growth in the surface magnetic dipole field strength, the true value of α may be lower than that inferred possibly from observations, $\alpha' = (2n' - 2)/(n' - 3)$, according to equation (8); see e.g. the upper left panel of Fig. A1. Broadly similar ideas were recently discussed by Rogers & Safi-Harb (2016). In regular pulsars a modest increase in the surface dipole field may potentially be caused by emergence of some of the stronger internal magnetic field from deep inside the NS (e.g. Muslimov & Page 1996) or out of the crust (e.g. Ho 2015) and into the magnetosphere.

2.3 The current age and spin-down power

The pulsar spins down as it injects energy into its environment largely in the form of an MHD wind, also causing its spin-down luminosity to decay over time from its initial value L_0 after an initial spin-down time t_0

$$L_{sd} = L_0 \left(1 + \frac{t}{t_0}\right)^{-m} \approx L_0 \times \begin{cases} 1 & t < t_0, \\ \\ (t/t_0)^{-m} & t > t_0, \end{cases} \quad (12)$$

where n is the braking index and $m = (n + 1)/(n - 1)$. For $n = 3$ and $m = 2$ we have

$$L_0 = 5.78 \times 10^{47} f B_{14}^2 P_{0,-3}^{-4} \text{ erg s}^{-1}. \quad (13)$$

The late time expression for L_{sd} can also be written as

$$L_{sd}(t > t_0) \approx L_{sd}(\text{obs}) \left(\frac{B_0}{B_s(\text{obs})}\right)^{-2} \left(\frac{t}{\tau_c}\right)^{-2}$$

$$= 2.05 \times 10^{34} \left(\frac{B_0}{1.16 \times 10^{14} f^{-1/2} \text{ G}}\right)^{-2} \left(\frac{t}{\tau_c}\right)^{-2} \frac{\text{erg}}{\text{s}}. \quad (14)$$

This demonstrates that for the usual magnetic dipole braking scenario, which assumes a constant surface dipole field, the age must be equal to the characteristic spin-down age in order to reproduce the observed spin-down power.

An older age, $t > \tau_c$, may still be possible if one or more of the underlying assumptions of this popular scenario breaks down. For instance, if there is a strong particle wind that opens up the magnetic dipole field lines above some radius r_{open} (where $R_{NS} < r_{open} < R_{LC}$), then this would correspond to $n = 1$ in equation (3) which would give an exponential growth of P and $t = (P/\dot{P}) \ln(P/P_0) = 2 \ln(P/P_0)\tau_c$, which is larger than $\tau_c = 4.9$ kyr by a factor of ∼11 − 15.6 for $P_0 \sim 1 - 10$ ms.

Another possibility is that the current $\dot{P}$ is larger than its long-term mean value, $\langle \dot{P} \rangle$, so that the true age for dipole braking would be $t \approx P/2\langle \dot{P} \rangle = \tau_c \dot{P}/\langle \dot{P} \rangle$, i.e. a factor of $\dot{P}/\langle \dot{P} \rangle$ larger than τ_c.

A decay of the magnetic dipole field would go in the opposite direction and result in $t < \tau_c$ (e.g. Colpi et al. 2000; Dall'Osso, Granot & Piran 2012, also see Fig. A2).

3 ENERGETICS OF THE X-RAY EMITTING SYNCHROTRON NEBULA

Here we consider the energetics of the X-ray nebula itself, within the observed radius $R_X = 2.04 d_4$ pc (for a mean angular radius of $\theta_X = 105$ arcsec), rather than the entire MWN with radius R. The nebula's X-ray luminosity is $L_X = 2.5 \times 10^{33} d_4^2$ erg s^{-1} in the $(h\nu_m, h\nu_M) = (0.5, 10)$ keV range, with a photon index $\Gamma = 2.2$.

The inner part of the X-ray nebula, of semi-minor and semi-major axis of 25×50 arcsec^2 [$(0.48 \times 0.97)d_4$ pc] or $R_{X, in} \approx 0.73 d_4$ pc, was detected by NuSTAR up to 30 keV. The total X-ray luminosity in this inner nebula combining *XMM–Newton* and NuSTAR observations in the $(h\nu_m, h\nu_M) = (0.5, 30)$ keV energy range is $L_{X, in} \approx 5.0 \times 10^{32}$ erg s^{-1}, with a photon index of $\Gamma_{in} = 1.41 \pm 0.12$.

The magnetic field in the X-ray emitting region can be estimated from the frequency-integrated synchrotron luminosity within the relevant region,

$$B = \left(\frac{L_X \sigma_e}{\mathcal{A} V} \frac{\Gamma - 2}{\Gamma - 1.5} \frac{\nu_1^{1.5-\Gamma} - \nu_2^{1.5-\Gamma}}{\nu_m^{2-\Gamma} - \nu_M^{2-\Gamma}}\right)^{2/7}$$

$$\simeq \begin{cases} 4.0\xi \sigma_e^{2/7} d_4^{-2/7} \text{ μG} & \text{(whole nebula)}, \\ \\ 5.0\xi_{in} \sigma_e^{2/7} d_4^{-2/7} \text{ μG} & \text{(inner nebula)}. \end{cases} \quad (15)$$

Here $\xi^{7/2}$ is the ratio of the total energy in electrons to that in the electrons radiating in the observed frequency range (given below in equation 16), while ν_1 and ν_2 are the characteristic synchrotron frequencies ($\nu_{syn} \simeq eB\gamma^2/2\pi m_e c$) corresponding to the boundary energies ($\gamma_1 m_e c^2$ and $\gamma_2 m_e c^2$) of the electron spectrum in equation (28), $V = 4\pi R_X^3/3$ or $V_{in} = 4\pi R_{X, in}/3$ is the volume filled with radiating plasma, $\sigma_e = E_B/E_e$ is the ratio of energies in the magnetic field ($E_B = VB^2/8\pi$) and in the electrons within the considered power-law energy distribution [$E_e = \int_{\gamma_1}^{\gamma_2} \gamma_e m_e c^2 (dN_e/d\gamma_e) d\gamma_e$, where $dN_e/d\gamma_e \propto \gamma_e^{-s}$ and $s = 2\Gamma - 1$] and $\mathcal{A} = 2^{1/2} e^{7/2}/18\pi^{1/2} m_e^{5/2} c^{9/2}$ (see e.g. Pacholczyk 1970).

We note that the harder photon index in the inner part of the nebula suggests that it may better reflect the true value of power-law index s of the un-cooled electron energy distribution, $s = 2\Gamma_{in} - 1 = 1.82 \pm 0.24$.

For our assumption of a single power-law electron distribution

$$\xi(\nu_1, \nu_2) = \left(\frac{\nu_2^{1.5-\Gamma} - \nu_1^{1.5-\Gamma}}{\nu_M^{1.5-\Gamma} - \nu_m^{1.5-\Gamma}} \right)^{2/7}. \tag{16}$$

In the above, the magnetic field with $\xi = 1$ or $\xi_{in} = 1$ assumes that $(\nu_1, \nu_2) = (\nu_m, \nu_M)$. However, there may be a break in the spectrum at energies lower than 0.5 keV (typically seen in PWNe between the radio and X-rays) corresponding to $\nu_1 < \nu_m$. Taking $\nu_1 = 10^{13}$ Hz, the typical break frequency observed in other PWNe, yields a higher magnetic-field strength in the whole X-ray nebula, $B \simeq 27\mu$G. This corresponds to changing $\xi \approx 6.80$ in the above equation. We define ξ_7 and ξ normalized by this value.

The unknown value of ν_2 is not important when $\Gamma > 1.5$, which corresponds to $s > 2$ for slow electron cooling. In this case most of the energy resides in electrons near the minimal electron Lorentz factor γ_1 with a corresponding synchrotron frequency ν_1, so that one can take $\nu_2 = \nu_M$. For $s < 2$ most of the energy resides in the highest energy electrons near γ_2, and ξ depends mainly on $\nu_2 = \nu_{syn}(\gamma_2)$, so that one can instead take $\nu_1 = \nu_m$. For $s \approx 2$ both boundaries are important and should be taken into account.

Alternatively, a lower bound on the nebular magnetic field can be obtained by requiring that the implied synchrotron frequency of the maximum energy electrons in the injected distribution, γ_2, would be at least as high as the largest observed frequency from the nebula. Electrons are accelerated at or near the wind termination shock and their maximum energy is limited by the size $\lesssim R_{TS}$ of this region over which they are initially confined and accelerated. Confinement of the particles within their acceleration region requires $R_L \simeq \gamma_e m_e c^2/eB(R_{TS}) < R_{TS}$, which implies a maximum energy of $\gamma_e m_e c^2 < \gamma_{max} m_e c^2 = eB(R_{TS})R_{TS} \approx eB(R_{LC})R_{LC}$. The last equality arises since $B \propto 1/r$ beyond R_{LC}, and this relates the confinement condition near R_{TS} in the nebula to the potential difference near R_{LC} and across the open field lines emanating from the NS, near its polar cap. As shown by De Jager & Harding (1992), $\gamma_{max} m_e c^2$ is, to within a factor of the order of unity, similar to the energy gained by electrons while dropping across the polar cap potential V_0, which is given by (Goldreich & Julian 1969)

$$V_0 = \frac{R_{NS}^3 \Omega^2 B_s}{c^2} = \sqrt{\frac{L_{sd}}{fc}}, \tag{17}$$

and can be expressed using the spin-down power. This yields an estimate of the maximum Lorentz factor of the injected electrons

$$\gamma_{max} = \frac{e}{m_e c^2} \sqrt{\frac{L_{sd}}{fc}} \simeq 4.9 \times 10^8 f^{-1/2}. \tag{18}$$

As argued by De Jager & Harding (1992), synchrotron losses will typically limit the maximum Lorentz factor of accelerated electrons to less than γ_{max}. Therefore, $\gamma_{max} \geq \gamma_2$ should be regarded as an absolute upper limit on the Lorentz factor of electrons injected downstream at the termination shock.

Then, in order to account for all of the X-ray emission in the observed range, we need $\gamma_{max} > \gamma_X$ in all of this range, where γ_X is the Lorentz factor of the X-ray emitting electrons. The most constraining condition comes from the upper end of the observed energy range, which is 30 keV from the NuSTAR detection of the inner X-ray nebula, and therefore we use here $E_M = 30E_{M, 30}$ keV. The synchrotron photon energy is $E_{syn}(\gamma_e) \approx \hbar eB\gamma_e^2/(m_e c)$ so that $\gamma_M \propto \sqrt{E_M/B}$. Thus, the nebular magnetic field is bounded from below by

$$B > B_{min} \equiv \frac{m_e^3 c^6 f E_X}{\hbar e^3 L_{sd}} \simeq 11.0 f E_{M,30} \mu G \tag{19}$$

which further constrains the flow magnetization

$$\sigma_e > 35.1 d_4 \left(\frac{f E_{M,30}}{\xi} \right)^{\frac{7}{2}} = 0.043 d_4 \left(\frac{f E_{M,30}}{\xi_7} \right)^{\frac{7}{2}},$$

$$\sigma_{e,in} > 15.4 d_4 \left(\frac{f E_{M,30}}{\xi_{in}} \right)^{\frac{7}{2}} = 0.055 d_4 \left(\frac{f E_{M,30}}{\xi_{in}/5} \right)^{\frac{7}{2}}. \tag{20}$$

The usual plasma magnetization parameter is $\sigma = B^2/4\pi w$ where w is the total particle enthalpy density, where for relativistically hot plasma $w = (4/3)e \gg \rho c^2$, where e is the internal energy density, so that $\sigma = \frac{3}{2} B^2/8\pi e$. This reduces to $\sigma = \frac{3}{2} E_B/E_e = \frac{3}{2}\sigma_e$ or $\sigma_e \to \frac{2}{3}\sigma$ if the electrons in the considered power-law energy distribution hold all of the energy in particles, $E_e = E_m$. If there is another population of electrons or energy in protons etc., so that these electrons hold only a fraction ϵ_e of the total energy in particles or matter, $E_e = \epsilon_e E_m$ with $\epsilon_e \leq 1$, then $\sigma_e \to \frac{2}{3}\sigma/\epsilon_e$.

Equation (20) implies that in order to accommodate values of $\sigma \approx \frac{3}{2}\sigma_e \epsilon_e \sim 10^{-3}$–$10^{-2}$ in the bulk of the nebula, which are suggested by observations (e.g. Chevalier 2004) and appear to be broadly consistent with recent simulations (e.g. Porth et al. 2013), one requires a ξ of at least a few to several,

$$\xi > 2.76 f E_{M,30} \left(\frac{d_4}{\sigma_e} \right)^{\frac{2}{7}} = 16.1 f E_{M,30} \left(\frac{\epsilon_e d_4}{\sigma_{-2.5}} \right)^{\frac{2}{7}},$$

$$\xi_{in} > 2.18 f E_{M,30} \left(\frac{d_4}{\sigma_{e,in}} \right)^{\frac{2}{7}} = 12.7 f E_{M,30} \left(\frac{\epsilon_e d_4}{\sigma_{in,-2.5}} \right)^{\frac{2}{7}}, \tag{21}$$

where $\sigma_{e, -2.5} = \sigma_e/10^{-2.5}$. In the following we will express the relevant quantities both in terms of ξ and σ_e, and in terms of $B = 15B_{15\mu G} \mu$G.

We note that our analysis assumes a uniform magnetic field in the X-ray nebula. However, it might be plausible that the magnetic field gradually decreases with the distance from the wind termination shock and is higher in its inner parts than in its outer parts. Moreover, the NuSTAR detection up to 30 keV is in the inner nebula, and applying equation (19) to the outer nebula gives $B_{out} > 3.7 f E_{M,10} \mu$G given that the outer nebula is detected only up to 10 keV, which is three times lower than the corresponding lower limit on the magnetic field in the inner nebula, $B_{in} > 11.0 f E_{M,30} \mu$G. However, our main results are not significantly affected by the assumption of a uniform field in the nebula.

The magnetic energy in the X-ray nebula from equation (15) is

$$E_B \simeq 6.4 \times 10^{44} \xi^2 \sigma_e^{4/7} d_4^{17/7} \ \text{erg},$$

$$\simeq 3.0 \times 10^{46} \xi_7^2 \sigma_e^{4/7} d_4^{17/7} \ \text{erg},$$

$$\simeq 9.3 \times 10^{45} B_{15\,\mu G}^2 d_4^3 \ \text{erg}, \tag{22}$$

where the synchrotron cooling time of electrons radiating at $E = 2E_2$ keV is

$$t_{\text{syn}} = \frac{6\pi m_e c}{\sigma_T B^2 \gamma_e} = \frac{6\pi}{\sigma_T} \left(\frac{e \hbar m_e c}{B^3 E_\gamma} \right)^{1/2}$$

$$\simeq 7.56 \xi^{-3/2} \sigma_e^{-3/7} E_2^{-1/2} d_4^{3/7} \ \text{kyr},$$

$$\simeq 0.42 \xi_7^{-3/2} \sigma_e^{-3/7} E_2^{-1/2} d_4^{3/7} \ \text{kyr},$$

$$\simeq 1.02 B_{15\,\mu G}^{-3/2} E_2^{-1/2} \ \text{kyr}. \tag{23}$$

The total energy in the MWN, $E = E_B + E_m = E_B + E_e/\epsilon_e$, can be estimated under the assumption that the pressure is uniform in the region between $R_{\text{TS}} < r < R$, where $R_X < R < R_{\text{SNR}}$, due to the sub-sonic expansion of the nebula

$$E = \left(\frac{1+\sigma}{\sigma} \right) E_B \left(\frac{R}{R_X} \right)^3$$

$$\simeq 1.4 \times 10^{46} \frac{(1+\sigma)}{\sigma^{3/7} \epsilon_e^{4/7}} \xi^2 d_4^{17/7} \left(\frac{R}{3R_X} \right)^3 \ \text{erg},$$

$$\simeq 6.5 \times 10^{47} \frac{(1+\sigma)}{\sigma^{3/7} \epsilon_e^{4/7}} \xi_7^2 d_4^{17/7} \left(\frac{R}{3R_X} \right)^3 \ \text{erg},$$

$$\simeq 2.5 \times 10^{47} \left(\frac{1+\sigma}{\sigma} \right) B_{15\,\mu G}^2 d_4^3 \left(\frac{R}{3R_X} \right)^3 \ \text{erg}. \tag{24}$$

4 MWN DYNAMICS AND ADIABATIC THERMAL HISTORY

Here we consider the dynamical evolution of the MWN, accounting for the energy injection by the magnetar's quiescent spin-down-powered MHD wind, the interaction with the SN ejecta and external medium, and adiabatic cooling or heating of the relativistic electrons in the MWN after they are initially accelerated in the wind termination shock, at radius R_{TS}.

The cumulative injected energy up to a time t can be expressed using the initial rotational energy

$$E_0 = \frac{n \pm 1}{2} L_0 t_0 = \frac{1}{2} I \Omega_0^2 \simeq 2 \times 10^{52} P_{0,-3}^{-2} \ \text{erg}, \tag{25}$$

where the + and − signs are, respectively, for the broken power-law approximation and the smooth form of $L_{\text{sd}}(t)$ in equation (12). The latter implies

$$E_{\text{inj}}(t) = \int_0^t L_{\text{sd}}(t') dt' = E_0 \left[1 - \left(1 + \frac{t}{t_0} \right)^{-\frac{2}{n-1}} \right], \tag{26}$$

while the former is used when deriving equation (32), and implies

$$E_{\text{inj}}(t) = \frac{2E_0}{n+1} \times \begin{cases} t/t_0 & t < t_0, \\\\ 1 + \frac{n-1}{2} \left[1 - \left(\frac{t}{t_0} \right)^{-\frac{2}{n-1}} \right] & t > t_0. \end{cases} \tag{27}$$

Downstream of the termination shock ($r > R_{\text{TS}}$), the injected electrons can be assumed to have a power-law distribution

$$N(\gamma_e) \propto \gamma_e^{-s} \qquad \text{for} \qquad \gamma_1 < \gamma_e < \gamma_2 \tag{28}$$

and they suffer adiabatic losses due to the expansion of the SNR, where their energy drops as $E_e \propto V^{1-\hat{\gamma}}$. For a relativistic gas, the adiabatic index is $\hat{\gamma} = 4/3$, and thus $E_e \propto R^{-1}$. Such an adiabatic index should also hold for a tangled magnetic field and for relativistic protons (or ions) that are also likely to be present in the nebula. The electrons also suffer radiative losses; however this effect is negligible for the majority of them as they are slow cooling; for $s > 1$ most electrons have energies close to the lower end of the distribution since $\gamma_e N(\gamma_e) \propto \gamma_e^{-s+1}$. Therefore we neglect any energy losses and assume the energy is conserved in the system. Under such conditions the total energy in the wind nebula changes adiabatically and when the nebula expands the energy in electrons injected at time t_i decreases with time t, such that

$$E(t) = \int_0^t L(t_i) f_{\text{ad}}(t_i) dt_i, \tag{29}$$

where $f_{\text{ad}}(t_i) = R(t_i)/R(t)$ is the adiabatic energy dilution factor and it depends on the expansion history of the MWN at times $t = t_i$. The fate of the MWN in turn depends on the initial energy E_0 and how it compares to the energy of the SN explosion $E_{\text{SN}} = 10^{51} E_{\text{SN, 51}}$ erg. When the MWN expands the energy it loses is gained by the SNR via pdV work, and if it contracts (when compressed by the reverse shock going into the SNR) it gains energy at the expense of the SNR. Altogether, under our assumption of no energy losses from the system the SNR's energy can be expressed in terms of the other energies in the system,

$$E_{\text{SNR}}(t) = E_{\text{SN}} + E_{\text{inj}}(t) - E(t). \tag{30}$$

We outline two cases in Appendix B based on whether $E_0 \gtrsim E_{\text{SN}}$, for which we choose the initial period $P_0 = 1$ ms, or $E_0 \lesssim E_{\text{SN}}$, which has $P_0 = 10$ ms, while using a fiducial value for the initial surface magnetic field $B_0 = 10^{14}$ G in both cases, and give the size $R(t_i)$ of the MWN in different stages of its evolution. The self-similar expansion of the nebula, shown in Fig. 2, can be generalized as

$$R(t) = R_\star \left(\frac{t}{t_\star} \right)^a \tag{31}$$

where $R_\star$ and $t_\star$ are the power-law break points calculated in Appendix B and summarized in Table 3.

Integration of the injected power, modified by adiabatic losses, then yields the total energy $E_{\text{ST}} \equiv E(t = t_{\text{ST}})$ in the nebula at the start of the Sedov–Taylor phase, shown in Fig. 3, with $\tilde{t} = t/t_0$,

$$E_{\text{ST}} = \frac{2E_0}{(n+1)\tilde{t}_{\text{ST}}} \times \begin{cases} \text{For} \quad E_0 > E_{\text{SN}} \\\\ \frac{3}{55} \tilde{t}_c^{5/2} + \frac{2}{5} + \ln \tilde{t}_{\text{ST}} \quad (m = 2) \\\\ \frac{3}{55} \tilde{t}_c^{5/2} + \frac{2}{5} + \frac{1 - \tilde{t}_{\text{ST}}^{2-m}}{m-2} \ (m \neq 2) \\\\ \text{For} \quad E_0 < E_{\text{SN}} \\\\ \frac{5}{11} + \ln \tilde{t}_{\text{ST}} \qquad (m = 2) \\\\ \frac{5}{11} + \frac{1 - \tilde{t}_{\text{ST}}^{2-m}}{m-2} \qquad (m \neq 2). \end{cases} \tag{32}$$
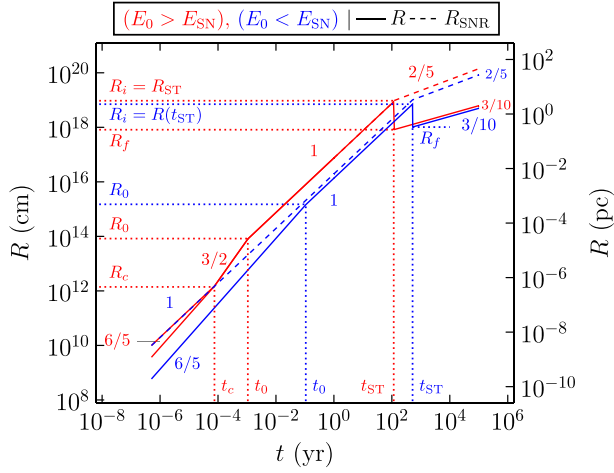
Figure 2. Schematic of the dynamical evolution of the MWN's radius (solid line) as a function of time in a constant density ISM ($k = 0$), with temporal power-law indices specified for the different segments and colour-coded for the two different cases. These are: $E_0 > E_{SN}$ ($P_{0,-3} = 1$, red) and $E_0 < E_{SN}$ ($P_{0,-3} = 10$, blue). The evolution of the SNR size is shown as a dashed line. The dotted lines punctuate special times in the dynamical evolution of the system, where t_c is the density core crossing time by the outer edge of the MWN, t_0 is the initial spin-down time of the magnetar after which its energy injection rate drops significantly, and t_{ST} is the onset time for the Sedov–Taylor phase. All these times have their corresponding radii. R_i and R_f are the radii of the MWN before and after it is crushed by the reverse shock at time $t = t_{ST}$. See Table 3 and text for details of these parameters. The following parameter values are assumed: $B_0 = 10^{14}$ G, $n = 3$, $n_{ext} = 1\,\mathrm{cm}^{-3}$, $M_{ej} = 3M_\odot$, $f = 1$, $E_{SN} = 10^{51}$ erg.

Note that the two expressions for $E_0 > E_{SN}$ and $E_0 < E_{SN}$ are equal at $E_0 = E_{SN}$ for $\tilde{t}_c = E_{SN}/E_0$ (i.e. a factor of 1.32 smaller than in equation B7), which is therefore used when numerically evaluating E_{ST} in order to produce the figures. We give approximate estimates for E_{ST} for the fiducial case of $m = 2(n = 3)$ for the two cases, where we ignore the $\tilde{t}_c$ term as it is small when $E_0 > E_{SN}$, which yields

$$E_{ST} = 1.1 \times 10^{48} \left(\frac{\kappa_1}{5.99}\right) f^{-1} B_{14}^{-2} M_3^{-5/6} E_{tot,52.3}^{1/2} n_0^{1/3} \text{ erg} \quad (33)$$

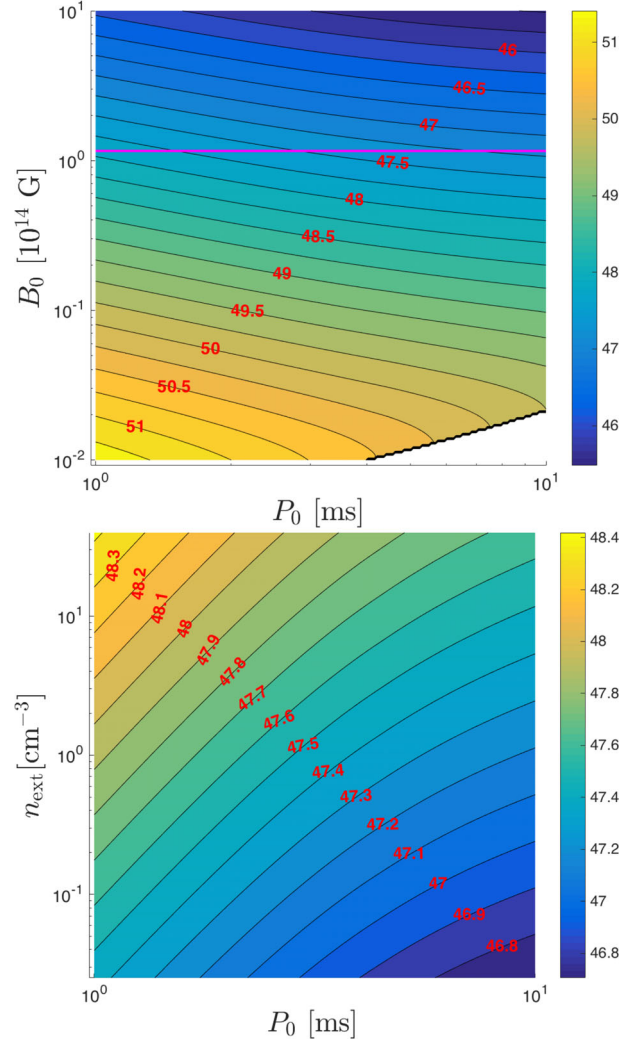with $\kappa_1 = \frac{2}{n+1}(2/5 + \ln \tilde{t}_{ST})$, and when $E_0 < E_{SN}$

$$E_{ST} = 1.8 \times 10^{47} \left(\frac{\kappa_2}{4.47}\right) f^{-1} B_{14}^{-2} M_3^{-5/6} E_{SN,51}^{1/2} n_0^{1/3} \text{ erg} \quad (34)$$

with $\kappa_2 = \frac{2}{n+1}(5/11 + \ln \tilde{t}_{ST})$. Although the dependence on P_0 is not explicit in these estimates, there is a mild dependence on it through κ_1 and κ_2, as can be seen in Fig. 3.

For $t > t_{ST}$ the expansion of the SNR volume follows the Sedov–Taylor solution with $R_{SNR} \propto t^{2/(5-k)}$. Here we have assumed a general density profile for the ISM $\rho_{ext}(R) = AR^{-k}$ where $k = 0(k = 2)$

Figure 3. Contour plot of the total energy $\log_{10}(E_{ST}[\mathrm{erg}])$ in the MWN at time $t = t_{ST}$ before it is crushed by the reverse shock, for the following parameter values: $n = 3$, $M_{ej} = 3M_\odot$, $f = 1$, $E_{SN} = 10^{51}$ erg. Top panel: for $n_{ext} = 1\,\mathrm{cm}^{-3}$ as a function of B_0 and P_0. The empty region in the bottom right is where $t_0 > 0.5t_{ST}$ so that our assumption of $t_0 \ll t_{ST}$ no longer holds. The horizontal magenta line corresponds to the inferred (current) surface dipole field [assuming it remained constant at its initial value, $B_0 = B_s(t) = 1.16 \times 10^{14} f^{-1/2}$ G]. Bottom panel: for $B_0 = B_s(t) = 1.16 \times 10^{14} f^{-1/2}$ G, as a function of n_{ext} and P_0.

applies to a constant density ISM (stellar wind). The onset of the Sedov–Taylor phase is marked by the equality of the swept up ISM mass, which starts to affect the dynamics, and that of the ejecta. It is also the approximate time when the MWN will interact strongly
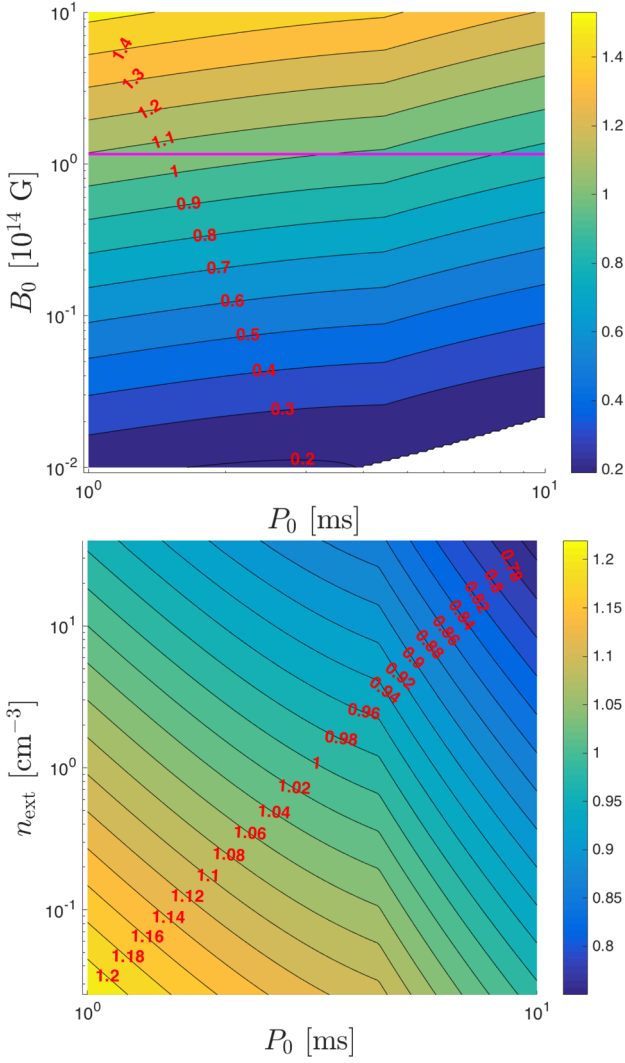
Table 3. Parameters for the dynamical evolution of the MWN in equation (31) and assuming $n = 3$ in two different scenarios, where the magnetar injects more energy than that of the SN ($E_0 > E_{SN}$) or less ($E_0 < E_{SN}$). Here t_c is the density core crossing time, t_0 is the initial spin-down time of the magnetar, and t_{ST} is the Sedov–Taylor phase onset time.

	a	R_*(cm)	t_*(s)	
	$6/5$	$R_c = 1.4 \times 10^{12} P_{0,-3}^4 E_{SN,51}^{3/2} f^{-1} B_{14}^{-2} M_3^{-1/2}$	$t_c = 2.4 \times 10^3 f^{-1} B_{14}^{-2} P_{0,-3}^4 E_{SN,51}$	$t < t_c$
$E_0 > E_{SN}$	$3/2$	R_c	t_c	$t_c < t < t_0$
	1	$R_0 = 8.3 \times 10^{13} f^{-1} B_{14}^{-2} P_{0,-3} M_3^{-1/2}$	t_0	$t_0 < t < t_{ST}$
$E_0 < E_{SN}$	$6/5$	$R_0 = 1.5 \times 10^{15} E_{SN,51}^{3/10} M_3^{-1/2} f^{-1} B_{14}^{-2} P_{0,-2}^{8/5}$	t_0	$t < t_0$
	1	R_0	t_0	$t_0 < t < t_{ST}$

Figure 4. Contour plot of $\log_{10}(\chi)$ (where $\chi = R_i/R_f$ is given in equation 40) for the same parameter values as in Fig. 3. Top panel: for $n_{\rm ext} = 1\,{\rm cm}^{-3}$ as a function of B_0 and P_0. The horizontal magenta line corresponds to the inferred (current) surface dipole field (assuming it remained constant at its initial value, $B_0 = B_{\rm s}(t) = 1.16 \times 10^{14} f^{-1/2}$ G). Bottom panel: for $B_0 = B_{\rm s}(t) = 1.16 \times 10^{14} f^{-1/2}$ G, as a function of $n_{\rm ext}$ and P_0.

with the reverse shock and be compressed by the pressure behind the forward blast wave. This occurs at

$$
\begin{aligned}
t_{\rm ST} &= 519 M_3^{5/6} E_{\rm tot,51}^{-1/2} n_0^{-1/3}\ {\rm yr} \\
&= 116 M_3^{5/6} E_{\rm tot,52.3}^{-1/2} n_0^{-1/3}\ {\rm yr}
\end{aligned}
\tag{35}
$$

where $E_{\rm tot} = E_{\rm SN} + E_0$ is the total mechanical energy imparted to the blast wave, and $M_3 = M_{\rm ej}/3{\rm M}_\odot$. The corresponding radius of the SNR is

$$
R_{\rm ST} = 3.07 M_3^{1/3} n_0^{-1/3}\ {\rm pc}.
\tag{36}
$$

In the following, we consider initial spin periods $P_0 = 10^{-3} P_{0,-3}$ s for which $E_{\rm tot} \simeq E_0 > E_{\rm SN}$, and $P_0 = 10^{-2} P_{0,-2}$ s with $E_{\rm tot} \simeq E_{\rm SN} > E_0$. The compression of the MWN by the reverse shock adiabatically heats the entire nebula, and the ratio of the final and initial energies is given by the ratio of the initial and final size of the nebula, shown in Fig. 4,

$$
\chi = \frac{E_{\rm f}}{E_{\rm i}} = \frac{R_{\rm i}}{R_{\rm f}} = \left(\frac{p_{\rm S}}{p_{\rm i}}\right)^{1/4}.
\tag{37}
$$

Here the total energy in the nebula before it is crushed $E_{\rm i} = E_{\rm ST}$, from equation (32). The nebula compression ratio is determined by the ratio of the pressure behind the Sedov blast wave at $t = t_{\rm ST}$

$$
p_{\rm S} \simeq 0.074 \left(\frac{E_{\rm tot}}{R_{\rm ST}^3}\right),
\tag{38}
$$

approximated here by the central pressure (e.g. Reynolds & Chevalier 1984; Shu 1992), and the initial pressure in the nebula before it is crushed. Since $\sigma \ll 1$ throughout the MWN volume, the total energy and pressure are dominated by that of particles, such that the total initial pressure in the nebula is

$$
p_{\rm i} = \frac{E_{\rm ST}}{4\pi R(t_{\rm ST})^3}.
\tag{39}
$$

Thus $\chi = (0.074 \times 4\pi)^{1/4} (E_{\rm tot}/E_{\rm ST})^{1/4} [R(t_{\rm ST})/R_{\rm ST}]^{3/4}$. In the first case ($E_0 > E_{\rm SN}$), we assume that the size of the MWN $R_i \sim R_{\rm SNR} = R_{\rm ST}$ before it is compressed by the reverse shock, and in the second case ($E_0 < E_{\rm SN}$) $R_i = R(t_{\rm ST}) = 6.3 \times 10^{18} [(n - 1)/2]^{-1/5} M_3^{1/3} E_{\rm SN,51}^{-1/5} n_0^{-1/3} P_{0,-3}^{-2/5}$ cm from equation (31). However, in order for χ to be continuous, we assume a slightly modified expression for $R_i \simeq R_{\rm ST} \times \min[1, (E_0/E_{\rm SN})^{1/5}]$, which is valid for both cases. Furthermore, taking $(0.074 \times 4\pi)^{1/4} \simeq 1$, we obtain for the continuous approximation $\chi \simeq (E_{\rm tot}/E_{\rm ST})^{1/4} \min[1, (E_0/E_{\rm SN})^{3/20}]$, or

$$
\chi = \begin{cases}
\left(\dfrac{E_{\rm tot}}{E_{\rm ST}}\right)^{1/4}, & E_0 > E_{\rm SN} \\[2ex]
\left(\dfrac{E_{\rm tot}}{E_{\rm ST}}\right)^{1/4} \left(\dfrac{E_0}{E_{\rm SN}}\right)^{3/20}, & E_0 < E_{\rm SN}
\end{cases}
\tag{40}
$$

and when inserting in all the relevant scalings,

$$
\chi = \begin{cases}
11.6\, B_{14}^{\frac{1}{2}} M_3^{\frac{5}{24}} E_{\rm tot,52.3}^{\frac{1}{8}} \left(\dfrac{\kappa_1}{6.0f}\right)^{-\frac{1}{4}} n_0^{-\frac{1}{12}}, & E_0 > E_{\rm SN} \\[3ex]
6.76\, \dfrac{B_{14}^{\frac{1}{2}} M_3^{\frac{5}{24}} E_{\rm tot,51}^{\frac{1}{8}}}{E_{\rm SN,51}^{\frac{3}{20}} P_{0,-2}^{\frac{3}{10}} \left(\frac{\kappa_2}{4.47f}\right)^{\frac{1}{4}} n_0^{\frac{1}{12}}}, & E_0 < E_{\rm SN}.
\end{cases}
\tag{41}
$$

After compression, the initial value of the nebula's equilibrium radius (around which the radius oscillates) is $R_{\rm f} \simeq R_{\rm ST}(E_{\rm ST}/E_{\rm tot})^{1/4} \min[1, (E_0/E_{\rm SN}^{1/20})]$, or

$$
R_{\rm f} = R_{\rm ST} \left(\frac{E_{\rm ST}}{E_{\rm tot}}\right)^{1/4} \times \begin{cases}
1, & E_0 > E_{\rm SN} \\[2ex]
\left(\dfrac{E_0}{E_{\rm SN}}\right)^{1/20}, & E_0 < E_{\rm SN}
\end{cases}
\tag{42}
$$

and with numerical values,

$$
R_{\rm f} = \begin{cases}
\dfrac{0.26\ {\rm pc}}{\sqrt{B_{14}}} \left(\dfrac{\kappa_1}{6.0 f n_0}\right)^{\frac{1}{4}} \left(\dfrac{M_3}{E_{\rm tot,52.3}}\right)^{\frac{1}{8}}, & E_0 > E_{\rm SN} \\[3ex]
\dfrac{0.33\ {\rm pc}}{B_{14}^{\frac{1}{2}} E_{\rm SN,51}^{\frac{1}{20}} P_{0,-2}^{\frac{1}{10}}} \left(\dfrac{\kappa_2}{4.5 f n_0}\right)^{\frac{1}{4}} \left(\dfrac{M_3}{E_{\rm tot,51}}\right)^{\frac{1}{8}}, & E_0 < E_{\rm SN}.
\end{cases}
\tag{43}
$$

In reality, and as seen in hydrodynamic simulations (e.g. Blondin, Chevalier & Frierson 2001; Van der Swaluw et al. 2001), the compressed nebula goes through a reverberation phase where its size oscillates before achieving pressure equilibrium. Here we assume that the MWN is compressed to $R_{\rm f}$ and then it begins its slow expansion outwards. Pressure equilibrium dictates that the MWN grows
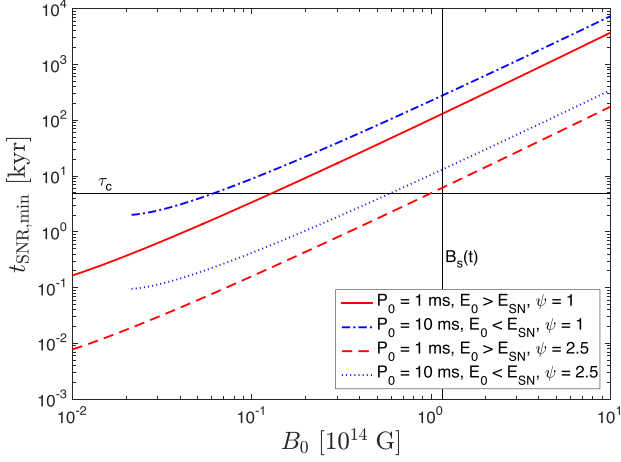
Figure 5. Minimum age of the system if the MWN is at least as large as the X-ray nebula, $R \geq R_X = 2.04d_4$ pc, shown as a function of the initial surface dipole magnetic-field strength, for two dynamical scenarios and two values of ψ. For a fixed B_0 value, the age estimate depends only weakly on P_0. All parameters (except ψ) are the same as given in the caption of Fig. 3. The values of the characteristic spin-down age τ_c and the current inferred surface dipole filed $B_s(t)$ are indicated by the thin black horizontal and vertical lines, respectively.

as $R(t) \propto p_S^{-1/4}$, where the internal pressure in the Sedov phase scales with time as $p_S \propto t^{-6/(5-k)}$, which yields

$$R(t) = \psi(t) R_{eq}(t) = \psi(t) R_f \left(\frac{t}{t_{ST}} \right)^{3/2(5-k)}, \quad (44)$$

where we have introduced the parameter $\psi = 2\psi_2$ below in order to account for the (order unity fractional) oscillations of R around its equilibrium value R_{eq} after the crushing (Blondin et al. 2001; Van der Swaluw et al. 2001). A fiducial value of $\psi = 2$ is used since during the order of unity fractional fluctuations in R it spends most of its time near its maximal value (within a single oscillation), making ψ close to its own maximal value more likely at a given snapshot of the system (corresponding to the present epoch). The current size of the MWN $R(t_{SNR})$ must be larger than that of the X-ray bright region $R_X = 2.04d_4$ pc, which yields an independent constraint on the age of the system,

$$t_{SNR} \gtrsim t_{ST} \left(\frac{R_X}{\psi(t_{SNR}) R_f} \right)^{2(5-k)/3}, \quad (45)$$

which equates to

$$t_{SNR} \gtrsim \begin{cases} \dfrac{10.3 \,\text{kyr}\, d_4^{\frac{10}{3}} B_{14}^{\frac{5}{3}} M_3^{\frac{5}{12}} n_0^{\frac{1}{2}}}{E_{tot,52.3}^{\frac{1}{12}} \left(\frac{\kappa_1}{6.0f} \right)^{\frac{5}{6}} \psi_2^{\frac{10}{3}}}, & E_0 > E_{SN} \\[2em] \dfrac{22.2 \,\text{kyr}\, B_{14}^{\frac{5}{3}} M_3^{\frac{5}{12}} E_{SN,51}^{\frac{1}{6}} d_4^{\frac{10}{3}} P_{0,-2}^{\frac{1}{3}} n_0^{\frac{1}{2}}}{E_{tot,51}^{\frac{1}{12}} \left(\frac{\kappa_2}{4.47f} \right)^{\frac{5}{6}} \psi_2^{\frac{10}{3}}}, & E_0 < E_{SN}. \end{cases} \quad (46)$$

This constraint is shown in Fig. 5 as a function of the initial magnetic-field strength for our two scenarios as well as for $\psi = 1$ and $\psi = 2$.

The total energy is then reduced adiabatically as the MWN re-expands, and if $t_0 \ll t_{ST}$ then the energy injection from the magnetar can be ignored, such that

$$E(R) = \left(\frac{R_f}{R} \right) \chi E_{ST}. \quad (47)$$

On the other hand, if the magnetar continues to inject energy at late times then the total energy in the MWN at $t > t_{ST}$ is given by

$$E(t) = \frac{\chi E_{ST}}{\hat{t}^a \psi(t)} + \frac{E_0 \tilde{t}_{ST}^{1-m}}{\hat{t}^a \bar{\psi}(t)} \times \begin{cases} \dfrac{1 - \hat{t}^{1+a-m}}{m-a-1}, & m \neq 1+a, \\[1.5em] \ln \hat{t}, & m = 1+a, \end{cases} \quad (48)$$

where $a = 3/[2(5-k)]$, $\hat{t} \equiv t/t_{ST}$ and

$$\bar{\psi}(t) = \frac{\psi(t) \int_{t_{ST}}^t dt_i\, t_i^{a-m}}{\int_{t_{ST}}^t dt_i\, t_i^{a-m} \psi(t_i)}$$

$$= \psi(t) \frac{1 - \hat{t}^{1+a-m}}{m-a-1} \left[\int_1^{\hat{t}} d\hat{t}_i\, \hat{t}_i^{a-m} \psi(\hat{t}_i) \right]^{-1} \quad (49)$$

is the effective weighted mean of the fractional change in ψ between t_{ST} and t, which takes into account that the electrons are injected at $R(t_i)$ rather than $R_{eq}(t_i)$ and therefore experience different adiabatic cooling (or heating) as the MWN evolves. The second term, which represents the energy injected by the wind at $t > t_{ST}$, becomes particularly important for $m < 1+a$, i.e. $m < 1.3$ for $k = 0$, in which case $E_{ST} \simeq E_0 \hat{t}_{ST}^{1-m}/(2-m)$ and this term eventually dominates at late times, $\hat{t} = t/t_{ST} > [(1+a-m)\chi/(2-m)]^{1/(1+a-m)}$. Nevertheless, for $m > 1.3$ and in particular for $m = 2$ that corresponds to $n = 3$ expected from magnetic dipole braking, the second term is not very important and can usually be neglected. For $m = 2$ and $n = 3$, the first term is larger than the second term by at least a factor of $0.7\chi\kappa$ where $\chi \sim 5.7 - 9.8$ and $\kappa \sim 8.9 - 12$ so that the second term would at most introduce a small correction of a few per cent, and one can neglect it to obtain a convenient expression,

$$\frac{E(R_X)}{10^{48}\,\text{erg}} \approx \begin{cases} \dfrac{1.66}{B_{14}^2} \left(\dfrac{\kappa_1}{6.0fd_4} \right) \sqrt{\dfrac{E_{tot,52.3}}{M_3}}, & E_0 > E_{SN} \\[2em] \dfrac{0.200}{B_{14}^2} \dfrac{\left(\frac{\kappa_2}{4.47} \right)}{fd_4 E_{SN,51}^{\frac{1}{5}} P_{0,-2}^{\frac{2}{5}}} \sqrt{\dfrac{E_{tot,51}}{M_3}}, & E_0 < E_{SN}. \end{cases} \quad (50)$$

The complete temporal evolution of the total energy in the MWN is shown in Fig. 6 for $\psi(t) = 1$; accurate treatment for the dynamical evolution of $\psi(t)$ during the reverberation phase of the nebula at $t \gtrsim t_{ST}$ is out of the scope of this work. In Fig. 7, the maximum energy in the MWN when its size is at least as large as the X-ray nebula is shown as a function of various parameters.

5 MWN INTERNAL STRUCTURE AND THE SYNCHROTRON COOLING LENGTH

An electron injected with initial energy $\gamma_i m_e c^2$ at the termination shock at time t_i cools due to the adiabatic expansion of the flow and by emitting synchrotron radiation, as governed by

$$\frac{d\gamma_e}{dt} = -\frac{a}{t} \gamma_e - bB^2(t) \gamma_e^2, \quad (51)$$

for $R \propto t^a$ as defined in equation (31), and where $b = \sigma_T/6\pi m_e c$. We assume that the magnetic field is spatially homogeneous but varies temporally due to the injection of magnetic energy by the central source and its adiabatic evolution driven by the expansion of the SNR volume,

$$B(t) \approx \sqrt{\frac{6E_B(t)}{R^3(t)}}, \quad (52)$$
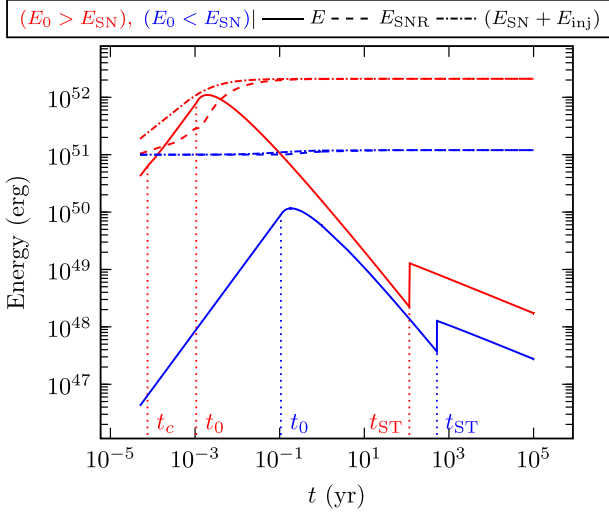
Figure 6. Total energy in the MWN as a function of its time. Two cases are shown: ($E_0 > E_{SN}$, with $E_0 = 2 \times 10^{52}$ erg, $P_0 = 1$ ms, and $B_{14} = 1$, solid red line) the magnetar injects more energy than the kinetic energy of the SN ejecta, thus seriously affecting the dynamical evolution of the SNR + MWN system, and ($E_0 < E_{SN}$, with $E_0 = 2 \times 10^{50}$ erg, $P_0 = 10$ ms, and $B_{14} = 1$, solid blue line) for which the magnetar is dynamically unimportant and the evolution of the SNR + MWN system mirrors that of canonical PWNe observed around regular radio pulsars. The dashed lines show the energy in the SNR from equation (30) and the dotted lines show the total energy in the system. Following parameter values are assumed: $\psi(t) = 1$, $n = 3$, $n_{ext} = 1$ cm^{-3}, $M_{ej} = 3$M$_\odot$, $f = 1$, $E_{SN} = 10^{51}$ erg, and $k = 0$.

where the expression we have used for the MWN's volume is valid as long as its radius satisfies $R(t) \gg R_{TS}$. The magnetic-field strength when $R(t) = R_X$ is

$$\frac{B(R_X)}{1\,\mu G} \approx \begin{cases} \dfrac{11.3}{B_{14} d_4^2} \sqrt{\dfrac{\kappa_1 \sigma_{-2.5}}{6.0 f(1+\sigma)}} \dfrac{E_{tot,52.3}^{\frac{1}{4}}}{M_3^{\frac{1}{4}}}, & E_0 > E_{SN} \\[14pt] \dfrac{3.92}{B_{14} d_4^2} \dfrac{\sqrt{\dfrac{\kappa_2 \sigma_{-2.5}}{4.47 f(1+\sigma)}} E_{tot,51}^{\frac{1}{4}}}{E_{SN,51}^{\frac{1}{10}} P_{0,-2}^{\frac{1}{5}} M_3^{\frac{1}{4}}}, & E_0 < E_{SN}. \end{cases}$$ (53)

One can express the field as $B(t) = [\sigma/(1+\sigma)]^{1/2} B_{max}(t)$, in terms of the maximal value of the field corresponding to all of the MWN energy being in magnetic form ($\sigma \to \infty$),

$$\frac{B_{max}(R_X)}{1\,\mu G} \approx \begin{cases} \dfrac{201}{B_{14} d_4^2} \sqrt{\dfrac{\kappa_1}{6.0 f}} \dfrac{E_{tot,52.3}^{\frac{1}{4}}}{M_3^{\frac{1}{4}}}, & E_0 > E_{SN} \\[14pt] \dfrac{69.6}{B_{14} d_4^2} \dfrac{\sqrt{\dfrac{\kappa_2}{4.47 f}} E_{tot,51}^{\frac{1}{4}}}{E_{SN,51}^{\frac{1}{10}} P_{0,-2}^{\frac{1}{5}} M_3^{\frac{1}{4}}}, & E_0 < E_{SN}. \end{cases}$$ (54)

We solve equation (51) in Appendix C and show the temporal evolution of the maximum electron Lorentz factor $\gamma_{max,\,inj}$ in Fig. 8 for both $E_0 > E_{SN}$ and $E_0 < E_{SN}$ cases. In the first case, we assume that the magnetar was born as a fast rotator with $P_0 \sim 1$ ms and surface magnetic field as inferred from the measured P and $\dot{P}$, $B_0 \sim 1.16 \times 10^{14}$ G (for $f = 1$), which remains constant over the age of the system $t_{SNR} = \tau_c = 4.9$ kyr. Alternatively, in the second case, we look at a field growth scenario where the nascent NS had a spin period $P_0 \sim 10$ ms and surface field $B_0 \sim 10^{12}$ G which then grows to the same strength as in the previous case over $t_{SNR} = 26.3$ kyr (see equation 2 for choice of age). Electrons injected at earlier times

cool rapidly to lower Lorentz factors as they are in the fast-cooling regime when their $\gamma_e(t) > \gamma_c(t) = 6\pi m_e c/\sigma_T B(t)^2 t$, where $\gamma_c(t)$ is the Lorentz factor of electrons that are cooling at the dynamical time t. When $R(t) = R_X$ then (neglecting the oscillations)

$$\frac{\gamma_c(R_X)}{10^6} \approx \begin{cases} 1.85 \dfrac{(1+\sigma)}{\sigma_{-2.5}} \dfrac{B_{14}^{\frac{1}{3}} d_4^{\frac{2}{3}} M_3^{\frac{1}{12}}}{\left(\dfrac{\kappa_1}{6.0 f}\right)^{\frac{1}{6}} n_0^{\frac{1}{2}} E_{tot,52.3}^{\frac{5}{12}}}, & E_0 > E_{SN} \\[18pt] 7.14 \dfrac{(1+\sigma)}{\sigma_{-2.5}} \dfrac{B_{14}^{\frac{1}{3}} d_4^{\frac{2}{3}} E_{SN,51}^{\frac{1}{30}} M_3^{\frac{1}{12}} P_{0,-2}^{\frac{1}{15}}}{\left(\dfrac{\kappa_1}{4.47 f}\right)^{\frac{1}{6}} n_0^{\frac{1}{2}} E_{tot,51}^{\frac{5}{12}}}, & E_0 < E_{SN} \end{cases}$$ (55)

is the Lorentz factor of electrons that are cooling at the dynamical time. However, majority of the particles in the MWN were injected at earlier times but they now have $\gamma_e(t) < \gamma_c(t)$, and thus are slow cooling. Yet, freshly injected electrons over the last dynamical time, which are contributing to the X-ray emission, are presently fast cooling.

5.1 Quasi-steady state: the inner region

Assuming that the particle's overall motion is dominated by advection, the distance r it travels over the time interval $\Delta t = t - t_i$ can be used to establish the cooling length of the X-ray emitting electrons. The flow speed downstream of the termination shock is governed by the magnetization of the wind. Observations of many PWNe suggest that the magnetization of the shocked pulsar wind is small, $\sigma \ll 1$, suggesting that the magnetic field is not dynamically important in the inner regions of the nebula where particle pressure dominates over magnetic pressure. Therefore, we use the hydrodynamic equations to describe the nebula's dynamics. The shocked wind in the nebula is relativistically hot, with its energy density e, pressure p, and proper rest mass density ρ satisfying $p = e/3 \gg \rho c^2$. For such a relativistically hot fluid of proper number density $\tilde{n}$ one obtains under spherical symmetry (Blandford & McKee 1976)

$$\frac{\partial}{\partial t}(\tilde{n}\gamma) + \frac{c}{r^2}\frac{\partial}{\partial r}(r^2 \tilde{n}\gamma\beta) = 0,$$

$$\frac{d}{dt}\left(\frac{p}{\tilde{n}^{4/3}}\right) = 0,$$

$$\frac{d}{dt}(p\gamma^4) = \gamma^2 \frac{\partial p}{\partial t},$$ (56)

where $\frac{d}{dt} = \frac{\partial}{\partial t} + \beta c \frac{\partial}{\partial r}$. Approximating the flow in the nebula as a steady state, we have $\frac{\partial}{\partial t} \to 0$ and $\frac{d}{dt} \to \beta c \frac{d}{dr}$ so that

$$\frac{d}{dr}(r^2 \tilde{n}\gamma\beta) = 0, \quad \frac{d}{dr}\left(\frac{p}{\tilde{n}^{4/3}}\right) = 0, \quad \frac{d}{dr}(p\gamma^4) = 0,$$ (57)

which imply that $r^2 \tilde{n}\gamma\beta$, $\tilde{n}^{-4/3}p$, and $p\gamma^4$ are all uniform (i.e. independent of r) within the nebula. Since the flow in the nebula is, to a good approximation, Newtonian ($\beta \lesssim 1/3$) we have $\gamma^4 \approx 1$ and therefore an approximately uniform pressure, $p \approx$ const, and density, $\tilde{n} \approx$ const. Finally, $r^2\beta \approx$ const is also uniform, implying a velocity profile,

$$\beta(r) = \beta_{TS}\left(\frac{r}{R_{TS}}\right)^{-2},$$ (58)

where the normalization is obtained by matching the flow speed at the termination shock.

In the low-σ limit, MHD shock jump conditions for orthogonal shocks dictate that $\beta_{TS} \approx \frac{1}{3}\sqrt{1 + 8\sigma}$ just downstream of the
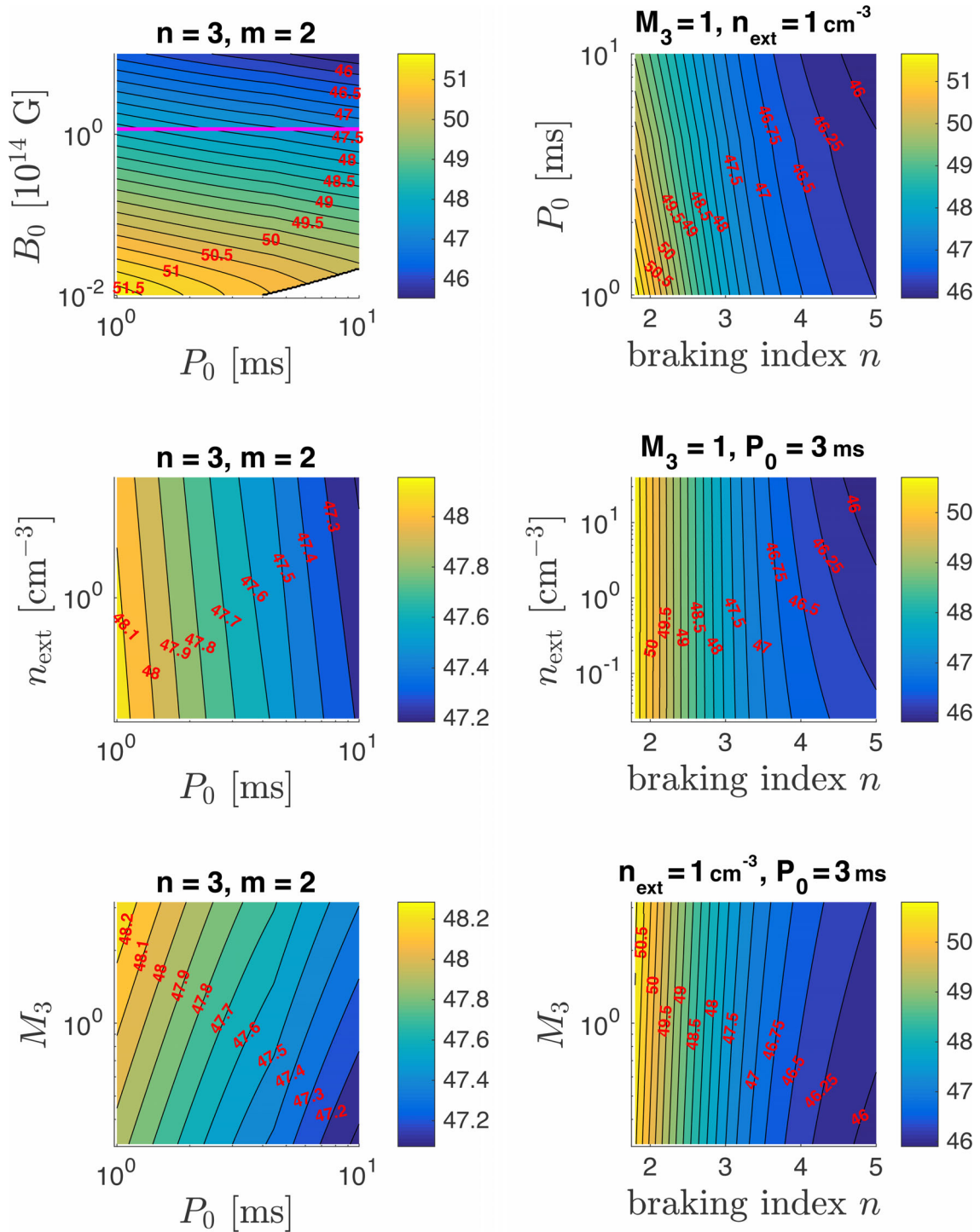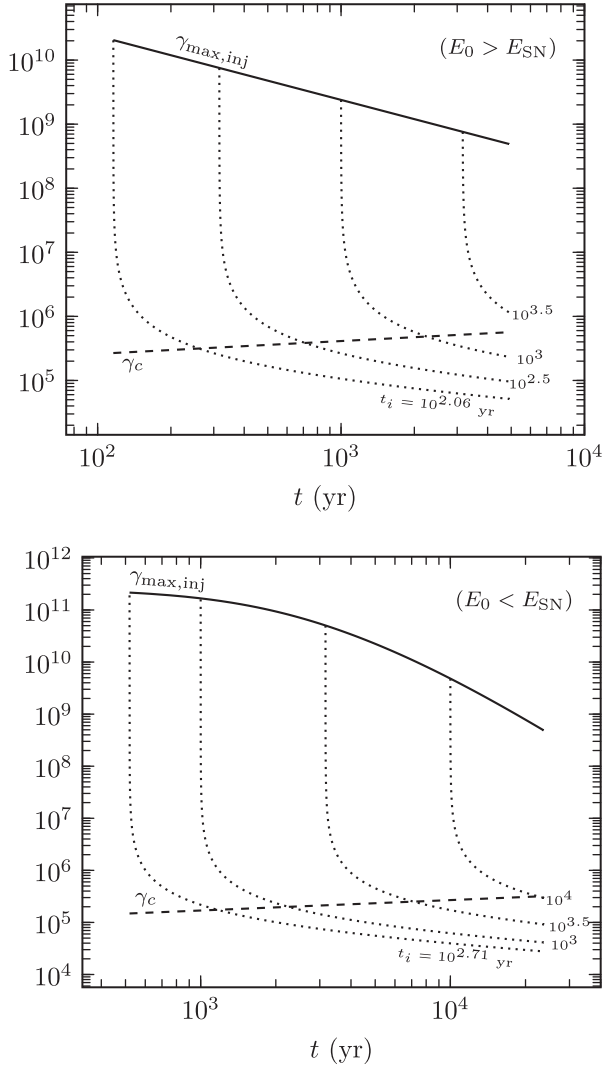
Figure 7. Contour plots of the log of the maximum total energy in the MWN, $\log_{10}(E[\text{erg}])$ from equation (48), under the condition that $R_{\text{MWN}} \geq R_X$. The left panels are for magnetic dipole spin down ($n = 3$ and $m = 2$), and show the dependence on the following parameters: top panel – the initial spin period P_0 and the equatorial surface dipole magnetic field B_0, where the horizontal magenta line corresponds to its inferred (current) value (which for $n = 3$ also corresponds to its initial value, $B_0 = B_s(t) = 1.16 \times 10^{14} f^{-1/2}$ G, which is also used in the two panels below this one); middle panel – P_0 and the external number density n_{ext}; bottom panel – P_0 and the $M_3 = M_{\text{ej}}/3\,\text{M}_\odot$. The right panels show the dependence on the braking index n (defined by equation 3), as well as P_0 (top panel), n_{ext} (middle panel), and M_3 (bottom panel). The remaining default parameter values used here are $n_{\text{ext}} = 1\,\text{cm}^{-3}$, $M_{\text{ej}} = 3\text{M}_\odot$, $P_0 = 3$ ms, $E_{\text{SN}} = 10^{51}$ erg.

termination shock (Kennel & Coroniti 1984). Furthermore, from magnetic flux conservation,

$$\frac{\text{d}}{\text{d}r}(r\beta B) = 0, \tag{59}$$

where the magnetic field is assumed to be purely toroidal, its strength initially increases $B(r) \propto r$. This would suggest that the magnetic pressure dominates at large distances from the termination shock, such that the flow speed asymptotes to the terminal speed

throughout the volume of the PWN which significantly reduces the magnetization of the flow.

Self-consistently assuming a steady state as described by equation (58) with $R_{TS} = R_{TS}(t_i)$ and $\beta_{TS} = 1/3$, which upon integration over time yields

$$r_{adv}(t_i, t) = R_{TS}(t_i) \left[1 + \frac{c\Delta t}{R_{TS}(t_i)} \right]^{1/3}, \tag{60}$$

where $\Delta t \equiv t - t_i$. For $r \gg R_{TS}(t_i)$ this leads to a simple analytic scaling for the advection length and time, $r_{adv} \approx (R_{TS}^2 c\Delta t)^{1/3} \propto (\Delta t)^{1/3}$ and $\Delta t_{adv} \approx r^3/cR_{TS}^2 \propto r^3$.

5.2 The non-steady outer region

The velocity boundary condition $\beta(r) = \beta_{MWN}$ at $r = R(t)$, from equation (31), gives the time evolution of the termination shock radius,

$$R_{TS,v}(t) = \sqrt{\frac{aR(t)^3}{\beta_{TS}ct}}. \tag{61}$$

However, this heavily relies on the steady-state assumption which is not valid throughout the nebula. A more realistic estimate for R_{TS} may be obtained through replacing the steady-state assumption by a balance at R_{TS} between the winds ram pressure, $L_{sd}/4\pi R_{TS}^2 c$, and the almost uniform pressure in the MWN, $p = e/3 = E(t)/3V(t) = E(t)/4\pi R(t)^3$, which yields

$$R_{TS,p}(t) = \sqrt{\frac{R(t)^3 L_{sd}(t)}{cE(t)}} \propto \psi(t)^2 t^{(4a-m)/2}$$

$$\approx \begin{cases} \dfrac{3.28\times10^{-3}\,\mathrm{pc}\ B_{14}d_4^2 M_3^{\frac{1}{4}}}{\sqrt{\frac{\kappa_1}{6.0f}}E_{tot,52.3}^{\frac{1}{4}}}, & E_0 > E_{SN} \\[3mm] \dfrac{9.44\times10^{-3}\,\mathrm{pc}\ B_{14}d_4^2 M_3^{\frac{1}{4}}E_{SN,51}^{\frac{1}{10}}P_{0,-2}^{\frac{1}{5}}}{\sqrt{\frac{\kappa_2}{4.47f}}E_{tot,51}^{\frac{1}{4}}}, & E_0 < E_{SN} \end{cases} \tag{62}$$

where $R \propto 1/E \propto t^a$ and $L_{sd} \propto t^{-m}$ was used to derive its scaling with the age of the system, t, and the numerical estimates are for $R = R_X$ and $a = 0.3$. The square of the ratio of these two estimates at equilibrium for this radius is

$$\left(\frac{R_{TS,p}(t)}{R_{TS,v}(t)} \right)^2_{eq} = \frac{tL_{sd}(t)}{3aE(t)} \propto t^{1+a-m}$$

$$\approx \begin{cases} \dfrac{0.0452\, B_{14}^{\frac{11}{3}}d_4^{\frac{13}{3}}M_3^{\frac{11}{12}}n_0^{\frac{1}{2}}}{\left(\frac{\kappa_1}{6.0f}\right)^{\frac{11}{6}}E_{tot,52.3}^{\frac{7}{12}}}, & E_0 > E_{SN} \\[3mm] \dfrac{0.806\, B_{14}^{\frac{11}{3}}d_4^{\frac{13}{3}}M_3^{\frac{11}{12}}E_{SN,51}^{\frac{11}{30}}n_0^{\frac{1}{2}}P_{0,-2}^{\frac{11}{15}}}{\left(\frac{\kappa_2}{4.47f}\right)^{\frac{11}{6}}E_{tot,51}^{\frac{7}{12}}}, & E_0 < E_{SN} \end{cases} \tag{63}$$

This shows that the approximation behind $R_{TS,v}$ is reasonable if the current energy in the MWN, $E(t)$, is dominated by the energy injected by the magnetar's spin-down wind by the last dynamical time, $\sim L_{sd}t$, but breaks down significantly when the MWN energy is dominated by energy injected at much earlier times that even after suffering adiabatic losses significantly exceeds the energy injected in the last dynamical time, $E(t) \gg tL_{sd}(t)$.

Nonetheless, near $R_{TS,p}$ where the flow was injected during the last dynamical time (roughly the time-scale over which the nebula

Figure 8. Temporal evolution of maximum electron Lorentz factor. $\gamma_{max,inj}$ (solid) is the maximum electron Lorentz factor injected at time t_i at the termination shock radius $R_{TS,p}$. Its magnitude is governed by the maximum polar cap voltage $V_0(t_i)$ which in turn depends on the surface magnetic field $B_s(t_i)$ and the spin period $P(t_i)$, as given in equation (92). The dotted lines show the cooling evolution of maximum energy electrons as a function of the dynamical time up to the current time. γ_c is the Lorentz factor of electrons that are cooling at the dynamical time. Top: the magnetar is born as a fast rotator with $P_0 = 1\,\mathrm{ms}$ and high surface magnetic field $B_0 = 1.16 \times 10^{14}\,\mathrm{G}$ which remains constant over the lifetime of the system $t_{SNR} = \tau_c = 4.9\,\mathrm{kyr}$. Bottom: the magnetar is born as a typical radio pulsar with $P_0 = 10\,\mathrm{ms}$ and surface field $B_0 = 10^{12}\,\mathrm{G}$ but experiences field growth so that its current field is $B_s = 1.16 \times 10^{14}\,\mathrm{G}$ as inferred from its P and $\dot{P}$ at its model age $t = t_{SNR} = 23.6\,\mathrm{kyr}$. In both cases, the nebular field strength at $t = t_{SNR}$ is $B = 15\,\mu\mathrm{G}$, for which $\sigma = 5.6 \times 10^{-3}$ when $E_0 > E_{SN}$ and $\sigma = 4.7 \times 10^{-2}$ when $E_0 < E_{SN}$. See Appendices A and C for more details.

given by $\beta_\infty \approx \sigma(1 + \sigma)^{-1}$. However, this is a serious artefact of the ideal MHD spherically symmetric model and has been shown to contradict observations and 3D numerical simulations. In fact, 3D numerical relativistic MHD simulations of Porth et al. (2013, see e.g. their fig. 5) show that PWNe are mostly isobaric and filled with low magnetization ($10^{-2} \lesssim \sigma \lesssim 10^{-1}$) plasmas with particle pressure governing the bubble dynamics. Their simulations show that the magnetic field is efficiently dissipated due to its randomization

doubles its age or size) one still expects the steady-state approximation of equations (58) and (60) to hold. This inner region extends out to a radius R_b that can be estimated as follows. At $R_b < r < R$ we expect a uniform and isotropic expansion of the plasma, with a velocity $v = dr/dt \propto r$ at any given time t. Matching the velocity at the MWN's outer boundary, $v(R) = \dot{R} = aR/t$ for $R \propto t^a$ implies a velocity $v = \dot{R}r/R = ar/t$ in this region. Therefore, it is natural to define R_b through the continuity of the velocity between the inner (equation 58) and outer regions, $v_{\mathrm{TS}}(R_{\mathrm{TS}}/R_b)^2 = aR_b/t$, which for $v_{\mathrm{TS}} = c/3$ implies (at equilibrium)

$$R_b(t) = \left(\frac{R_{\mathrm{TS,p}}^2 ct}{3a}\right)^{\frac{1}{3}} = R(t)\left(\frac{tL_{\mathrm{sd}}(t)}{3aE(t)}\right)^{\frac{1}{3}} \propto \psi(t)^{\frac{4}{3}} t^{\frac{1+4a-m}{3}}$$

$$\approx \begin{cases} \dfrac{0.336\,\mathrm{pc}\, B_{14}^{\frac{11}{9}}\, d_4^{\frac{22}{9}}\, M_3^{\frac{11}{36}}\, n_0^{\frac{1}{6}}}{\left(\frac{\kappa_1}{6.0f}\right)^{\frac{11}{18}} E_{\mathrm{tot,52.3}}^{\frac{7}{36}}\psi_2^{\frac{10}{9}}}, & E_0 > E_{\mathrm{SN}} \\[3mm] \dfrac{0.887\,\mathrm{pc}\, B_{14}^{\frac{11}{9}}\, d_4^{\frac{22}{9}}\, M_3^{\frac{11}{36}}\, E_{\mathrm{SN,51}}^{\frac{11}{90}} n_0^{\frac{1}{6}} P_{0,-2}^{\frac{11}{45}}}{\left(\frac{\kappa_2}{4.47f}\right)^{\frac{11}{18}} E_{\mathrm{tot,51}}^{\frac{7}{36}}\psi_2^{\frac{10}{9}}}, & E_0 < E_{\mathrm{SN}}. \end{cases} \tag{64}$$

Altogether, the velocity profile as shown in Fig. 9 is given by

$$v(r,t) = \begin{cases} \dfrac{cR_{\mathrm{TS,p}}^2(t)}{3r^2} = \dfrac{aR_b^3(t)}{tr^2}, & R_{\mathrm{TS,p}}(t) < r < R_b(t) \\[3mm] \dfrac{ar}{t}, & R_b(t) < r < R(t) \end{cases} \tag{65}$$

We can verify that the advection time out to R_b is close to the dynamical time, and indeed $\Delta t_{\mathrm{adv}}(R_b) \approx R_b^3/cR_{\mathrm{TS,p}}^2 = t/3a \sim t$. As this time is estimated using the velocity derived in the steady-state approximation, which is valid for $\Delta t \ll t \Leftrightarrow t_i \approx t$, this implies that $\Delta t_{\mathrm{adv}}(R_b) \sim t_i$ or that the fluid element is advected to R_b by the time $t_b(t_i) = t_i + \Delta t_{\mathrm{adv}}(R_b) \sim 2t_i$. At a time t, the fluid that is at $R_b(t)$ was injected at $t_i \sim t/2$, so that $r < R_b$ corresponds to $t_i \gtrsim t/2 \Leftrightarrow \Delta t \lesssim t/2$ while $r > R_b$ corresponds to $t_i \lesssim t/2 \Leftrightarrow \Delta t \gtrsim t/2$. Once the fluid element enters the outer region, $r > R_b$, its fractional radial location in the nebula, $r(t)/R(t)$, becomes constant, since both r and R scale as t^a. Therefore, in this picture the outer nebula is gradually filled from its inner boundary [$R_b(t)/R(t) \propto t^{(1+a-m)/3}$ decreases with time for $m > 1 + a$ that is needed in order to have such an outer region] as it expands uniformly ($\Delta V \propto r^3 \propto t^{3a}$ for any fluid element whose radial coordinate is r) and isotropically. Adiabatic cooling becomes significant only in the outer part of the nebula, over times that are at least comparable to the dynamical time.

The uniform pressure and energy density in the MWN imply that $E(< R_b)/E = (R_b/R)^3 = L_{\mathrm{sd}}t/3aE = (R_{\mathrm{TS,p}}/R_{\mathrm{TS,v}})^2 \propto t^{1+a-m}$ and therefore $E(< R_b) \approx L_{\mathrm{sd}}t$, so that indeed the inner region, $R_{\mathrm{TS,p}}(t) < r < R_b(t)$, where the steady-state flow approximation holds, contains the energy and matter that was injected in the last dynamical time. The outer region, $R_b(t) < r < R(t)$, contains energy and matter that were injected before the last dynamical times and suffered significant adiabatic losses. Nonetheless, we find that for most of the relevant parameter space [namely $m = (n+1)/(n-1) > 1 + a \to 1.3$ or $n < (2+a)/a \to 7.67$] it still dominates the total MWN energy $E(t)$.

Using equation (65) for $v(r < R_b, t)$ instead of equation (58) accounts for the gradual evolution between the different instantaneous quasi-steady states of the flow in the inner nebula. It can be used to generalize the expression for $r_{\mathrm{adv}}(t_i, t)$ from equation (60). Denoting $\bar{t} \equiv t/t_i$ and by using the scaling $R_{\mathrm{TS,p}}(t) = R_{\mathrm{TS,p}}(t_i)\bar{t}^{(4a-m)/2}$ it can
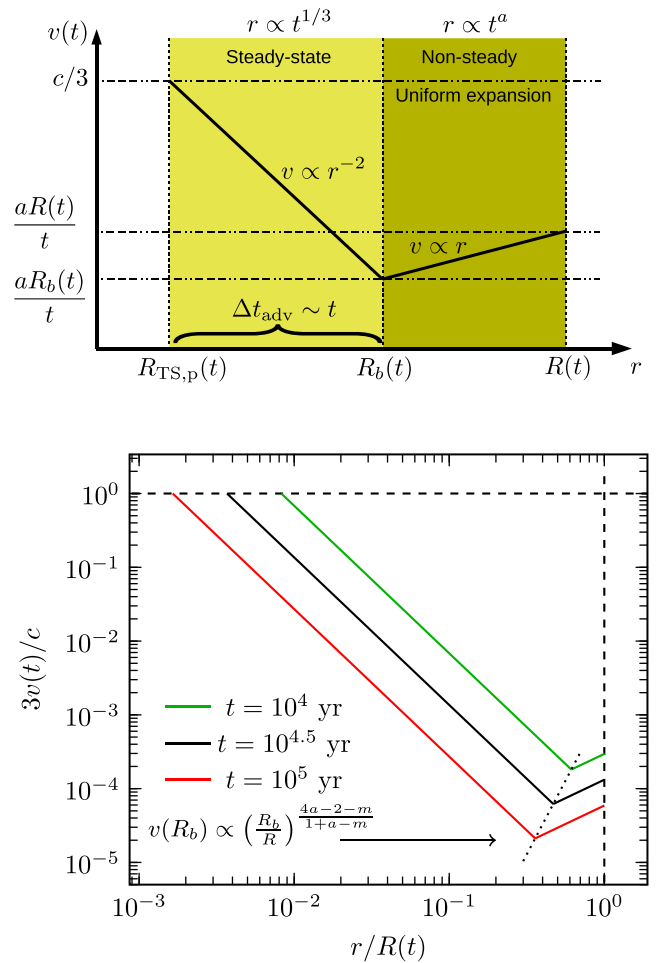
Figure 9. Top: velocity profile (log–log plot) of the advective flow in the nebula shown for both where it assumes a steady-state and where this assumption fails. The flow is launched at the termination shock radius $R_{\mathrm{TS,p}}(t)$ with velocity dropping quadratically with radius at a fixed temporal snapshot of the nebula. The steady-state region terminates at radius $R_b(t)$ beyond which the flow expands uniformly with radius out to the edge of the MWN at $R(t)$. Bottom: velocity profiles at three different temporal snapshots, $t_0 < t_1 < t_2$ with fiducial values assumed for $m = 2$ and $a = 0.3$ (when $k = 0$). The dotted line shows the dependence of the velocity on R_b at different snapshots in time.

be integrated to obtain

$$r_{\mathrm{adv}} = R_{\mathrm{TS,p}}(t_i)\left(1 + \frac{ct_i}{R_{\mathrm{TS,p}}(t_i)}\left[\frac{\bar{t}^{1+4a-m} - 1}{1 + 4a - m}\right]\right)^{\frac{1}{3}}$$

$$= R_{\mathrm{TS,p}}(t)\left(\bar{t}^{-\frac{3(m-4a)}{2}} + \frac{ct}{R_{\mathrm{TS,p}}(t)}\left[\frac{1 - \bar{t}^{m-4a-1}}{1 + 4a - m}\right]\right)^{\frac{1}{3}}. \tag{66}$$

It can be seen that $r_{\mathrm{adv}}(t_i = t) = R_{\mathrm{TS}}(t) = R_{\mathrm{TS}}(t_i)$.

The expression for $r_{\mathrm{adv}}(t_i, t)$ can be used to find the distance travelled by particles over their cooling times, which is then used to express $\gamma_e = \gamma_e(r, t)$.

For a uniform magnetic field in the nebula in steady state (neglecting adiabatic cooling due to the expansion of the nebula, which is a reasonable approximation if the cooling time is shorter than the dynamical times) the cooling time is $t_{\mathrm{syn}} = t_{c,0}/\gamma_e \propto E_{\mathrm{syn}}^{-1/2}$. The cooling length r_c is obtained by equating $t_{\mathrm{syn}}(\gamma_e) = \Delta t \approx r^3/cR_{\mathrm{TS,p}}^2$, which implies a weak dependence of the cooling length on the

observed synchrotron frequency,

$$
\begin{aligned}
r_{\mathrm{c,adv}} &\approx \left(R_{\mathrm{TS,p}}^2 c t_{\mathrm{c,0}}\right)^{\frac{1}{3}} \gamma_{\mathrm{e}}^{-\frac{1}{3}} = \left(R_{\mathrm{TS,p}}^2 c t_{\mathrm{c,0}}\right)^{\frac{1}{3}} \left(\frac{E_{\mathrm{syn}}}{h\nu_0}\right)^{-\frac{1}{6}} \\
&= \begin{cases} \dfrac{0.150\,\mathrm{pc}\; B_{14}^{\frac{2}{3}} d_4^{\frac{4}{3}} M_3^{\frac{1}{6}}}{\left(\frac{\kappa_1}{6.0f}\right)^{\frac{1}{3}} E_{\mathrm{tot},52.3}^{\frac{1}{6}} B_{15\,\mu\mathrm{G}}^{\frac{1}{2}} E_2^{\frac{1}{6}}}, & E_0 > E_{\mathrm{SN}} \\[2em]
\dfrac{0.303\,\mathrm{pc}\; B_{14}^{\frac{2}{3}} d_4^{\frac{4}{3}} M_3^{\frac{1}{6}} P_{0,-2}^{\frac{2}{15}} E_{\mathrm{SN},51}^{\frac{1}{15}}}{\left(\frac{\kappa_2}{4.47f}\right)^{\frac{1}{3}} E_{\mathrm{tot},51}^{\frac{1}{6}} B_{15\,\mu\mathrm{G}}^{\frac{1}{2}} E_2^{\frac{1}{6}}}, & E_0 < E_{\mathrm{SN}}, \end{cases}
\end{aligned}
\tag{67}
$$

where $t_{\mathrm{c,0}} = 6\pi m_{\mathrm{e}} c / \sigma_T B^2$ and we have conveniently expressed $E_{\mathrm{syn}} = h\nu_0 \gamma_{\mathrm{e}}^2$ with $\nu_0 = eB/2\pi m_{\mathrm{e}} c$. This implies that if the observed size is determined by the cooling length, i.e. by synchrotron burn-off, then the energy dependence of the observed size should be rather weak. Moreover, in our case the ratio $r_{\mathrm{c,adv}}$ is too small to account for the observed size of the X-ray nebula, $r_{\mathrm{c,adv}}/R_X \sim 0.06 - 0.12 \ll 1$.

5.3 Comparison with observations

The most relevant observation for the synchrotron cooling length is the spatial distribution of the spectral slope within the X-ray nebula. The photon index softens with distance from the magnetar (Younes et al. 2016), from $\Gamma_{\mathrm{in}} = 1.41 \pm 0.12$ in the inner ellipse of size (semi-minor and semi-major axes) 25×50 arcsec^2 [$(0.48 \times 0.97)d_4$ pc] using *XMM*+NuSTAR data, to $\Gamma_{\mathrm{out}} = 2.5 \pm 0.2$ in the outer ellipse of size 80×130 arcsec^2 (($1.55 \times 2.52)d_4$ pc) using *XMM* data. It is still not clear whether this softening, by $\Delta\Gamma = 1.09 \pm 0.38$, reflects the MWN's intrinsic emission spectrum or is alternatively at least partly caused by a spatially varying absorption column N_{H} through the nearby GMC. If the photon index of the inner ellipse is interpreted as representing that of the intrinsic emission spectrum of the uncooled shock accelerated electron distribution, $\mathrm{d}N_{\mathrm{e}}/\mathrm{d}\gamma_{\mathrm{e}} \propto \gamma_{\mathrm{e}}^{-s}$, this leads to $F_\nu \propto \nu^{(1-s)/2} = \nu^{1-\Gamma_{\mathrm{in}}}$ and $s = 2\Gamma_{\mathrm{in}} - 1 = 1.82 \pm 0.24$, which is rather hard but with a rather large uncertainty. Values of $s \sim 1.5$ or so are inferred in PWNe at lower energies, but usually in the X-ray energy range the inferred values are around $s \sim 2 - 2.5$, which is also consistent with the uncertainties. Moreover, the additional uncertainty due to the possible spatially varying N_{H} makes it even harder to draw any strong conclusions from the measured value of Γ.

In the following we will assume that the intrinsic spectral softening is at most similar to the observed one. The relatively gradual and modest degree of spectral softening ($\Delta\Gamma \lesssim 1.1$ when the size of the region grows by a factor of ~ 3 in terms of the distance from the magnetar) would be hard to reconcile with the weak dependence of the cooling length on the observed synchrotron photon energy, $r_{\mathrm{c,adv}} \propto E_{\mathrm{syn}}^{1/6}$ that we derived, if the observed size of the X-ray nebula, R_X, is indeed determined by synchrotron burn-off. One way around this is if R_X is instead limited by the sensitivity of our observation and the background, and is somewhat smaller than the cooling length of the electrons emitting in the observed energy range, which results in a smaller and more gradual softening of the photon index with the distance from the magnetar. However, this requires $r_{\mathrm{c,adv}}(E_X) > R_X$, while for typical parameters we obtain that $r_{\mathrm{c,adv}}(E_X) \ll R_X$.

5.4 The role of diffusion

This might still be reconciled with the observations if the effects of particle diffusion within the nebula are important and cannot be

neglected as we did so far, when we considered only the particle advection with the bulk flow in the nebula. This would also tend to moderate the spectral softening with the distance from the magnetar.

After injection at the termination shock ($r = R_{\mathrm{TS,p}}$), the particles start to both diffuse and advect downstream. We define their distance travelled over time Δt due to advection as the advection length, l_{adv}, and their typical distance travelled by diffusion as the diffusion length, l_{diff}. For $c\Delta t \ll R_{\mathrm{TS,p}}$ we have $l_{\mathrm{adv}} \approx c\Delta t/3$ as $c/3$ is the flow velocity just behind the wind termination shocks. For $c\Delta t \gg R_{\mathrm{TS,p}}$ the advection length is given by $l_{\mathrm{adv}} \sim r(\Delta t) \approx (R_{\mathrm{TS,p}}^2 c\Delta t)^{1/3}$, while the diffusion length is[1] $l_{\mathrm{dif}} \approx (2\lambda_{\mathrm{def}} c\Delta t)^{1/2} \approx (2\lambda_{\mathrm{def}} R_{\mathrm{TS,p}}^{-2} r^3)^{1/2}$ where $\lambda_{\mathrm{def}}(\gamma_{\mathrm{e}})$ is the deflection length of an electron of Lorentz factor γ_{e}. The ratio of these two lengthscales is

$$
\frac{l_{\mathrm{dif}}}{l_{\mathrm{adv}}} \approx \left(\frac{8\lambda_{\mathrm{def}}^3 c\Delta t}{R_{\mathrm{TS,p}}^4}\right)^{1/6} \approx \frac{\sqrt{2\lambda_{\mathrm{def}} r}}{R_{\mathrm{TS,p}}} \equiv \sqrt{\frac{r}{r_*}},
\tag{68}
$$

and it grows as $\Delta t^{1/6} \propto r^{1/2}$ so that diffusion dominates at large radii $r > r_*$ where

$$
r_* = \frac{R_{\mathrm{TS,p}}^2}{2\lambda_{\mathrm{def}}} = \frac{R(t)^3 L_{\mathrm{sd}}(t)}{2c E(t) \lambda_{\mathrm{def}}(\gamma_{\mathrm{e}}, t)}.
\tag{69}
$$

Since the advection and diffusion start just downstream of the shock, at $r = R_{\mathrm{TS,p}}$, then l_{adv} or l_{dif} corresponds to $\Delta r = r - R_{\mathrm{TS,p}}$, rather than to r. While for $c\Delta t \gg R_{\mathrm{TS,p}} \Leftrightarrow r \gg R_{\mathrm{TS,p}}$ we have $\Delta r \approx r$ and this distinction is not very important, in our case for the X-ray emitting electrons we have $\Delta r_* \lesssim R_{\mathrm{TS,p}}$, which makes this distinction very important. This can be seen when writing the numerical values in equation (69), for which one needs to specify the deflection length.

One generally expects λ_{def} to increase with γ_{e} so that r_* decreases with γ_{e}, i.e. increases for lower energy electrons that hence remain advection dominated out to a larger radius. The deflection length should be at least comparable to the electron's Larmor radius, which for the X-ray emitting electrons [$\gamma_{\mathrm{e}} = \gamma_X$ for which $E_{\mathrm{syn}}(\gamma_X) = E_X = 2E_2$ keV] is $R_{\mathrm{L}}(\gamma_X) = \gamma_X m_{\mathrm{e}} c^2/eB$ or

$$
R_{\mathrm{L}}(\gamma_X) = 3.95 \times 10^{-3} B_{15\,\mu\mathrm{G}}^{-3/2} E_2^{1/2} \text{ pc.}
\tag{70}
$$

Using such a parametrization where $\zeta \equiv \lambda_{\mathrm{def}}/R_{\mathrm{L}} \gtrsim 1$ (and $\zeta = 1$ corresponds to Bohm diffusion), we find

$$
\frac{\Delta r_*}{10^{-3}\,\mathrm{pc}} \approx \begin{cases} \dfrac{2.36\, B_{14}^2 d_4^4 B_{15\,\mu\mathrm{G}}^{\frac{3}{2}} M_3^{\frac{1}{2}}}{\left(\frac{\kappa_1}{6.0f}\right) E_{\mathrm{tot},52.3}^{\frac{1}{2}} E_2^{\frac{1}{2}} \zeta}, & E_0 > E_{\mathrm{SN}} \\[2em]
\dfrac{11.3\, B_{14}^2 d_4^4 B_{15\,\mu\mathrm{G}}^{\frac{3}{2}} M_3^{\frac{1}{2}} P_{0,-2}^{\frac{2}{5}} E_{\mathrm{SN},51}^{\frac{1}{5}}}{\left(\frac{\kappa_2}{4.47f}\right) E_{\mathrm{tot},51}^{\frac{1}{2}} E_2^{\frac{1}{2}} \zeta}, & E_0 < E_{\mathrm{SN}}. \end{cases}
\tag{71}
$$

Comparison to equation (62) shows that indeed for our case $\Delta r_* \lesssim R_{\mathrm{TS,p}}$. Because of this, in this case there is no region where advection dominates over diffusion, i.e. diffusion dominates throughout the whole nebula (i.e. $r_* = R_{\mathrm{TS,p}}$). This can be seen in the upper panel of Fig. 10.

Therefore, the expression we derived for the diffusion length, $l_{\mathrm{dif}} \approx (r^3/r_*)^{1/2}$, is no longer valid. Instead, the diffusion length is $l_{\mathrm{dif}} = \Delta r_{\mathrm{dif}} \approx (2\lambda_{\mathrm{def}} c\Delta t)^{1/2}$. The effect of advection can be neglected for the X-ray emitting electrons, so that their number density without accounting for the electron cooling approximately scales as $1/r$,

---

[1] For diffusion in i dimensions the diffusion coefficient is $D = \lambda_{\mathrm{def}} v/i$ and the r.m.s. displacement is $\sqrt{\langle l^2 \rangle} = \sqrt{2iD\Delta t} = \sqrt{2\lambda_{\mathrm{def}} v\Delta t}$, and in our case $v \approx c$.
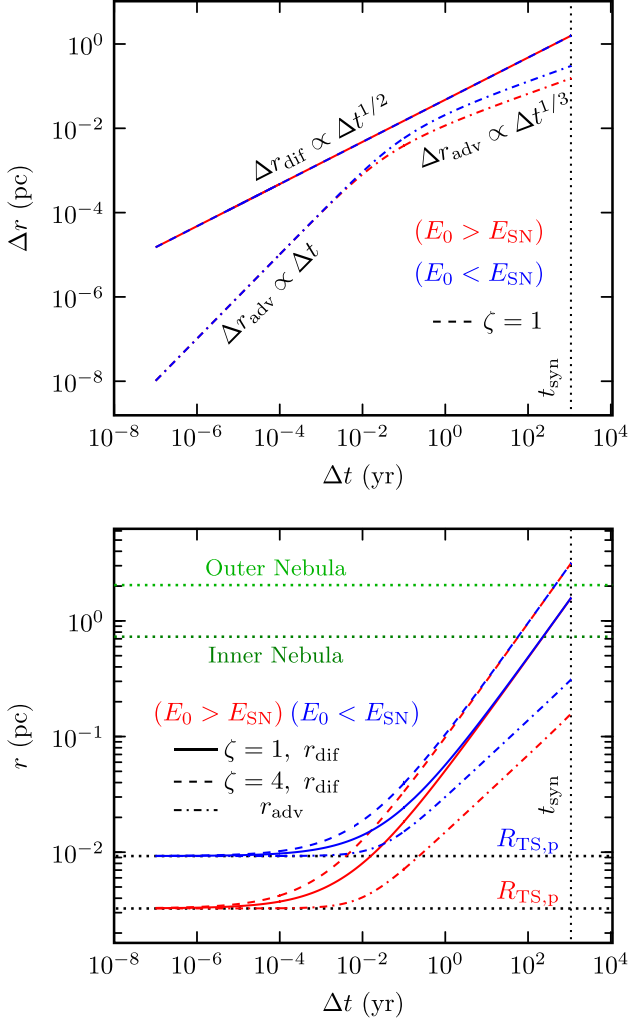
Figure 10. Diffusion and advection distance of fast-cooling particles [$\gamma_e = 10^8 > \gamma_c(t)$] over their cooling times $\Delta t = t - t_i \leq t_{syn}$ (shown by the vertical dotted line) for a system age $t = t_{SNR} = 10.3$ kyr when $E_0 > E_{SN}$ (red, for $\sigma = 5.6 \times 10^{-3}$) and $t_{SNR} = 22.2$ kyr when $E_0 < E_{SN}$ (blue, for $\sigma = 4.7 \times 10^{-2}$). Top: radial distance from the termination shock $R_{TS,p}$: diffusion length (dashed) $\Delta r_{dif} = l_{dif}$ for $\zeta = 1$, and advection length (dot–dashed) $\Delta r_{adv} = l_{adv}$. Bottom: diffusion and advection (dot–dashed) distances $r = R_{TS,p} + \Delta r$. Diffusion length is shown for two cases: (solid) $\zeta \equiv \lambda_{def}/R_L = 1$ (Bohm diffusion) with mean deflection length (λ_{def}) equal to the Larmor radius ($R_L(\gamma_e)$), and (dashed) $\zeta = 4$. The horizontal green dotted lines indicate the radial extents of the inner and outer X-ray nebulae and the black dotted lines show the position of $R_{TS,p}(t_{SNR})$.

following the solution for spherical steady-state diffusion from a steady source, $\tilde{n}(\gamma_e, r > r_*) \approx \tilde{n}(\gamma_e, r_*)\frac{r_*}{r} \to \tilde{n}(\gamma_e, R_{TS,p})\frac{R_{TS,p}}{r}$. Accounting for electron cooling implies that $\tilde{n}(\gamma_e, r)$ starts dropping exponentially with r past the electron's cooling length, which is set by $r_{c,dif} \approx [2\lambda_{def}ct_{syn}(\gamma_e)]^{1/2}$ or

$$r_{c,dif} \approx 1.57\, B_{15\,\mu G}^{-3/2} \zeta^{1/2}\ \text{pc}. \tag{72}$$

Since we derived $B \gtrsim 11\,\mu$G and one expects $\zeta \gtrsim 1$ then this lengthscale might potentially account for the observed size of the X-ray nebula (R_X), e.g. for $B_{15\,\mu G} \sim 1$ and $\zeta \sim 1$–2. Projection effects imply that the surface brightness scales as $r\tilde{n}(r)$, which is roughly uniform at $r < r_{c,dif}$. An energy dependence of $\zeta = \zeta(\gamma_e)$ would introduce a corresponding energy dependence of $r_{c,dif}$. If $\zeta = \lambda_{def}(\gamma_e)/R_L(\gamma_e) \gtrsim 1$ is of the order of unity near γ_X but some-

what increases at lower γ_e this might account for the mild spectral softening with r that was observed (if it is indeed intrinsic and not due to a spatially varying N_H). Improved spatially resolved measurement of the photon index could help pin down its origin and teach us more about the underlying physics of the MWN. Altogether these effects of particle diffusion (and advection in the inner nebula) could potentially account both for the observed size of the nebula and its spatially resolved spectrum, and a detailed fit to a more elaborate model along similar lines might help constrain the underlying physics [e.g. $\zeta(\gamma_e)$].

6 THE QUASI-STEADY-STATE ENERGY BALANCE OF THE X-RAY NEBULA

As we have seen from equations (23), the synchrotron cooling time of the X-ray emitting electrons is much smaller than the dynamical time, $t_{syn} \ll t_{SNR}$. Therefore, for modelling the X-ray nebula it is reasonable to use a steady-state approximation and neglect the expansion of the nebula over the relevant time-scales. The relevant time-scales here are mainly the advection ($\Delta t_{adv}(R_X)$) and diffusion ($\Delta t_{dif}(R_X)$) time-scales from $R_{TS,p}$ to R_X. In steady state (i.e. for $r < R_b(t)$) the energy within that radius satisfies $E(<r) = \langle\dot{E}\rangle\Delta t_{adv}(r)$, where $\langle\dot{E}\rangle$ is the long-term mean (over times larger than our current observations, up to the dynamical time) energy injection rate in outflows from the magnetar into the MWN, and $\Delta t_{adv}(r)$ is the time over which the energy flows from $R_{TS,p}$ to r. We parametrize $\langle\dot{E}\rangle \equiv gL_{sd}$ where L_{sd} is the current spin-down power. Thus defined, $g < 1$ is possible if the current L_{sd} is above its long-term mean value, while the contribution from burst-associated outflows does not compensate for that. On the other hand, $g > 1$ is possible if the long-term mean contribution from burst-associated outflows exceeds the current L_{sd}.

6.1 Magnetic energy balance

We assume that a fraction $\sigma/(1 + \sigma)$ of $\langle\dot{E}\rangle$ is injected in the form of magnetic fields, such that $E_B(<r) = B^2 r^3/6$ satisfies

$$\frac{1+\sigma}{\sigma}E_B(<r) = E(<r) = \langle\dot{E}\rangle\Delta t_{adv}(r) = gL_{sd}\Delta t_{adv}(r). \tag{73}$$

Using the lower limit on B from equation (19), $B > B_{min}$, this can be written as

$$\frac{g\sigma}{1+\sigma} = \frac{E_B}{L_{sd}\Delta t_{adv}(r)} > \frac{B_{min}^2 R_X^3}{6L_{sd}\Delta t_{adv}(r)}. \tag{74}$$

This yields

$$\frac{g\sigma}{1+\sigma} > \frac{\frac{1}{6}B_{min}^2 r^3}{L_{sd}\Delta t_{adv}(r)} = \frac{B_{min}^2 R(t)^3}{6E(t)} = \frac{E_{B,min}(<R)}{E(t)}$$

$$\approx \begin{cases} \dfrac{0.0030\, B_{14}^2 d_4^4 M_3^{\frac{1}{2}} f^3 E_{30}^2}{(\frac{\kappa_1}{6.0})E_{tot,52.3}^{\frac{1}{2}}}, & E_0 > E_{SN} \\[2em] \dfrac{0.0249\, B_{14}^2 d_4^4 M_3^{\frac{1}{2}} P_{0,-2}^{\frac{2}{5}} E_{SN,51}^{\frac{1}{5}} f^3 E_{30}^2}{(\frac{\kappa_2}{4.47})E_{tot,51}^{\frac{1}{2}}}, & E_0 < E_{SN} \end{cases} \tag{75}$$

where the numerical values are estimated for $R = R_X$.

A complimentary constraint can be obtained by using our modelling of the nebula dynamics and the implied magnetic field, e.g. as given by equation (53), which provides $B(t) = [\sigma/(1+\sigma)]^{1/2}B_{max}(t)$ where B_{max} is the upper limit on B for which all of the nebula's energy $E(t)$ resides in its magnetic field. The condition $B > B_{min}$

corresponds to $\sigma/(1+\sigma) > (B_{\min}/B_{\max})^2$ and leads to exactly the same constraint as equation (75) just without the factor g. Indeed, the factor g can be removed from equation (75) due to the following arguments. Taking into account that when the total energy in the nebula is dominated by injection well before the last dynamical time, it also determines the pressure in the nebula (and its energy density, which determines $B_{\max}$), and the condition of pressure equilibrium will determine the small fractional volume, $(R_b/R)^3$, occupied by the plasma injected over the last dynamical time. Varying g will mainly change R_b but as long as $(R_b/R)^3 \approx gL_{sd}t/E(t) < 1$ it will hardly affect the energy density in the nebula. The result $\Delta t_{adv}(R_b)$ $\sim t_i$, which is also $\sim t$ for the plasma currently at R_b, will remain valid (averaging over a sufficiently long time during which the sporadic outflows act together more coherently on the flow in the nebula) so that $\Delta t_{adv} \approx r^3/cR_{TS,p}^2 \rightarrow t(r/R_b)^3 \sim r^3/cR_{TS,p}^2 g$ since $R_b^3 \propto L_{sd} \rightarrow gL_{sd}$. Also, recall that equation (73) that was used for deriving equation (75) relies on an estimate of the energy within a given volume, i.e. the energy density, which is uniform in the nebula and largely independent of g as long as $gL_{sd}t/E(t) < 1$.
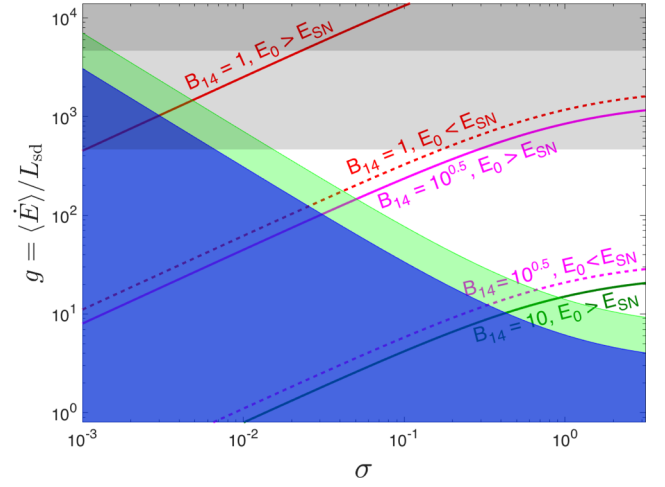
6.2 Energy balance of X-ray emitting electrons

Since the cooling time of the X-ray emitting electrons is much smaller than the dynamical time, $t_{syn} \sim 1$ kyr, we can assume a steady state for their emission and take $\langle \dot{E} \rangle$ as the mean value over the time t_{syn} to obtain an equation for the energy balance of the X-ray emitting electrons,

$$\langle \dot{E} \rangle = gL_{sd} = \frac{(1+\sigma)}{\epsilon_e \epsilon_X} L_{X,tot}, \tag{76}$$

where $L_{X,tot} = 2.74 \times 10^{33}$ erg s^{-1} is the luminosity in the whole X-ray nebula within the detected energy range, i.e. $0.5 - 10$ keV in the outer nebula and $0.5 - 30$ keV in the inner nebula. Here a fraction $1/(1+\sigma)$ of the total energy injected into the nebula goes into particles, a fraction ϵ_e of the latter energy goes into the power-law electron (and positron) energy distribution responsible for the observed X-ray emission, and a fraction ϵ_X of the latter energy is radiated in the observed X-ray energy range (thus contributing to the observed X-ray luminosity L_X between ν_m and ν_M corresponding to $\gamma_m < \gamma_e < \gamma_M$).

As long as $s > 1$ and there are fewer high-energy electrons than low-energy electrons in the initial electron power-law energy distribution (without the effects of electron radiative cooling) then one can neglect the contribution to L_X of electrons initially with $\gamma_e > \gamma_M$ that cool down into the contributing range $\gamma_m < \gamma_e < \gamma_M$ and deposit there a fraction $\sim \gamma_M/\gamma_{e,i}$ of their energy. For $\gamma_M \gg \gamma_m$ each such electron radiates an energy of $\approx \gamma_M m_e c^2$ within the observed range ($\nu_m < \nu < \nu_M$). Therefore, the increase in L_X compared to the contribution of electrons initially in the range $\gamma_m < \gamma_e < \gamma_M$ is by a factor of f_L given by

$$f_L - 1 = \frac{\int_{\gamma_M}^{\gamma_2} d\gamma_e \frac{dN_e}{d\gamma_e} \gamma_M}{\int_{\gamma_m}^{\gamma_M} d\gamma_e \frac{dN_e}{d\gamma_e} \gamma_e} = \frac{\gamma_M \int_{\gamma_M}^{\gamma_2} d\gamma_e \gamma_e^{-s}}{\int_{\gamma_m}^{\gamma_M} d\gamma_e \gamma_e^{1-s}}$$

$$= \begin{cases} \left(\frac{2-s}{s-1}\right) \frac{\gamma_M \left(\gamma_M^{1-s} - \gamma_2^{1-s}\right)}{\left(\gamma_M^{2-s} - \gamma_m^{2-s}\right)}, & s \neq 1, 2 \\[2ex] \frac{\ln(\gamma_2/\gamma_M)}{(1-\gamma_m/\gamma_M)}, & s = 1 \\[2ex] \frac{(1-\gamma_M/\gamma_2)}{\ln(\gamma_M/\gamma_m)}, & s = 2. \end{cases} \tag{77}$$

Figure 11. The excluded parameter space in the g–σ plane, according to equation (80), is the shaded blue region on the bottom left. The shaded green region is excluded if one assumes that the magnetic field in the nebula does not increase with distance from the central magnetar. The grey shaded region is excluded according to equation (92) for $t_{SNR} = 10^{4.5}$ yr and $B_{int, max} = 10^{16}$ G (light grey) or $B_{int, max} = 10^{16.5}$ G (darker grey). The thick solid and dashed lines represent the constraint from equation (83) for a few values of B_0 and for our two cases $E_0 < E_{SN}$ (dashed lines) and $E_0 > E_{SN}$ (solid lines).

In our case $\Gamma_{in} = 1.41 \pm 0.12$ implies $s \gtrsim 1.82 \pm 0.24$ and $\gamma_M/\gamma_m = (\nu_M/\nu_m)^{1/2} \approx 7.746$ while for $h\nu_M = 30$ keV

$$\frac{\gamma_M}{\gamma_2} > \frac{\gamma_M}{\gamma_{\max}} = \frac{0.86}{\sqrt{B_{15\,\mu G}}}, \tag{78}$$

implying $f_L - 1 \ll 1$ and $f_L \approx 1$, so this effect can be ignored.

The fraction of the energy of the electrons in the power-law component that initially radiates in the observed X-ray range ($\gamma_m < \gamma_e < \gamma_M$) is $\xi^{-7/2}$. Therefore, we have $\epsilon_X = f_L \xi^{-7/2} \approx \xi^{-7/2}$ and equation (76) becomes

$$g = \frac{L_{X,tot}}{L_{sd}} \frac{(1+\sigma)\xi^{7/2}}{\epsilon_e} = \frac{\eta_X (1+\sigma)\xi^{7/2}}{\epsilon_e}, \tag{79}$$

where $\eta_X = L_{X,tot}/L_{sd} \simeq 0.13d_4^2$. Now, using the lower limit on ξ that conservatively assumes that the X-ray emission extends up to 30 keV only in the inner nebula where it is detected by NuSTAR up to such energies (i.e. ξ_{in} in equation 21), this yields

$$\frac{g\sigma}{1+\sigma} > 3.07d_4^3 E_{M,30}^{7/2} f^{7/2}, \tag{80}$$

or

$$g > g_{\min} = 3.07 \frac{1+\sigma}{\sigma} d_4^3 E_{M,30}^{7/2} f^{7/2}. \tag{81}$$

Using the lower limit on ξ that assumes the emission extends up to 30 keV in the whole nebula (i.e. ξ in equation 21) or that the magnetic field in the nebula does not increase with distance from the central magnetar gives a numerical coefficient of 7.03 in this equation. The resulting excluded and allowed regions in the g–σ parameter space are shown in Fig. 11.

Equating between the magnetic field in the inner nebula derived from its X-ray emission (equation 15) and the nebular field derived

from modelling its dynamics (equations 52 and 53) results in an expression for $\xi_{\rm in}$,

$$\xi_{\rm in} = \begin{cases} \dfrac{39.8\, E_{\rm tot,52.3}^{\frac{1}{4}} \epsilon_e^{\frac{2}{7}} \sqrt{\frac{\kappa_1}{6.0f}}\, \sigma^{\frac{3}{14}}}{B_{14} d_4^{\frac{12}{7}} M_3^{\frac{1}{4}} \sqrt{1+\sigma}}, & E_0 > E_{\rm SN} \\[20pt] \dfrac{13.8\, E_{\rm tot,51}^{\frac{1}{4}} \epsilon_e^{\frac{2}{7}} \sqrt{\frac{\kappa_2}{4.47f}}\, \sigma^{\frac{3}{14}}}{B_{14} E_{\rm SN,51}^{\frac{1}{10}} d_4^{\frac{12}{7}} M_3^{\frac{1}{4}} P_{0,-2}^{\frac{1}{5}} \sqrt{1+\sigma}}, & E_0 < E_{\rm SN}. \end{cases} \tag{82}$$

Substituting this expression in equation (79) gives an expression for g,

$$g = \begin{cases} \dfrac{1422\, E_{\rm tot,52.3}^{\frac{7}{8}} \left(\frac{\kappa_1}{6.0f}\right)^{\frac{7}{4}}}{B_{14.5}^2 d_4^4 M_3^{\frac{7}{8}}} \left(\dfrac{\sigma}{1+\sigma}\right)^{\frac{3}{4}}, & E_0 > E_{\rm SN} \\[22pt] \dfrac{35.03\, E_{\rm tot,51}^{\frac{7}{8}} \left(\frac{\kappa_2}{4.47f}\right)^{\frac{7}{4}}}{B_{14.5}^2 E_{\rm SN,51}^{\frac{7}{20}} d_4^4 M_3^{\frac{7}{8}} M_3^{\frac{7}{8}} P_{0,-2}^{\frac{7}{10}}} \left(\dfrac{\sigma}{1+\sigma}\right)^{\frac{3}{4}}, & E_0 < E_{\rm SN} \end{cases} \tag{83}$$

where $B_0 = 10^{14.5} B_{14.5}$ G.

This constraint is also shown in Fig. 11. It can be seen that for no evolution of the magnetic field, i.e. $B_0 = B_{\rm s}(t) = 1.16 \times 10^{14} f^{-1/2}$ G, g is very high, arguably unrealistically so, although for our case $B_{14} = 1$ and $E_0 < E_{\rm SN}$, it is still possible (e.g. with $10^{-1.5} \lesssim \sigma \lesssim 10^{-1}$ and $10^2 \lesssim g \lesssim 10^{2.5}$).

Since very high values of g may be hard to produce physically, this may suggest that $B_0 > B_{\rm s}(t)$ and the surface dipole field has decayed since the birth of the magnetar. Following the phenomenological study of Dall'Osso, Granot & Piran (2012), we shall adopt here as an illustrative example their preferred values of $\alpha \approx 3/2$ and $\tau_{d,i} = \alpha t_B \approx 1\,\rm kyr$. Since a dipole field decay implies a true age younger than the characteristic spin-down age, which in our case $\tau_{\rm c} = 4.9\,\rm kyr$ is already barely compatible with the estimates of the SNR age $t_{\rm SNR} \sim 5 - 100\,\rm kyr$, this would in turn suggest that the current $\dot{P}$ is anomalously large compared to its long-term mean value $\langle\dot{P}\rangle$, by a factor of $K = \dot{P}/\langle\dot{P}\rangle$. This would imply a new characteristic spin-down age of $\tau_{\rm c,*} = K\tau_{\rm c}$ and a true surface magnetic field $B_{\rm s,*} = B_{\rm s} K^{-1/2}$. For significant field decay $\tau_{\rm c,*} \approx \tau_{d,i}(2-\alpha)^{-1}(B_0/B_{\rm s,*})^2$, which corresponds to

$$B_0 = B_{\rm s}\sqrt{\dfrac{(2-\alpha)\tau_{\rm c}}{\tau_{d,i}}} \sim \dfrac{(1.15 - 1.82) \times 10^{14}\,\rm G}{f^{1/2}(\tau_{d,i}/1\,\rm kyr)}, \tag{84}$$

where the numerical values are for the favoured values of $1.5 \lesssim \alpha \lesssim 1.8$ (not that K has factored out here, and that this expression is valid only for $t >$). This suggests $1 \lesssim B_{14} \lesssim 2$, which in turn suggests that $g \gtrsim 10^{1.5}$. Moreover, this is a rather low B_0 for a magnetar. However, interestingly enough, this is rather similar to the value of $B_0 \sim 2 \times 10^{14}$ G inferred for transient SGRs/AXPs (Dall'Osso, Granot & Piran 2012). The corresponding true age would retain a dependence of K,

$$t \approx \dfrac{(2-\alpha)^{\frac{\alpha}{2}}\, \tau_{\rm c}^{\frac{\alpha}{2}}\, K^{\frac{\alpha}{2}}}{\alpha\, \tau_{d,i}^{\frac{\alpha-2}{2}}} \sim (4.3 - 7.3) \left(\dfrac{\tau_{d,i}}{1\,\rm kyr}\right)^{\frac{2-\alpha}{2}} \left(\dfrac{K}{10}\right)^{\frac{\alpha}{2}}\,\rm kyr, \tag{85}$$

but $t \gg \tau_{\rm c}$ would require rather extreme values of $K \gg 10$.

6.3 An alternative energy source is required: the decay of magnetar's magnetic field

The natural channel of energy injection into the nebula, in addition to the rotationally powered MHD wind, is the decay of the initial super-QED magnetic field, which powers the sporadic bursting activity of the central magnetar and might also be responsible for the quasi-steady particle wind (e.g. Thompson & Blaes 1998). As mentioned earlier, the internal (predominantly toroidal) magnetic field has $\lesssim 10^2$ times more energy than that in the dipole component. The feasibility of either field component for supplying the requisite energy to the nebula over the last dynamical time can be ascertained using simple arguments.

6.3.1 The dipole field decay is not enough

We first consider the decay of the dipole component and make the assumption that its decay from its initial value $B_{\rm dip,0} > B_{\rm s}(t)$, where $B_{\rm s}(t)$ is the surface dipole field inferred from its current P and $\dot{P}$, is given by a power law in time (see equation A4). The total energy of the dipole component is $E_{B,\rm dip}(t) = B_{\rm s}^2(t) R_{\rm NS}^3/6$ and the power injected by its decay is

$$|\dot{E}_{B,\rm dip}| = \dfrac{2}{\alpha}\dfrac{E_{B,\rm dip,0}}{t_B}\tau^{-1-\frac{2}{\alpha}} = \dfrac{2}{\alpha}\dfrac{E_{B,\rm dip}(t)}{t_B \tau}, \tag{86}$$

where $\tau = 1 + t/t_B$, $E_{B,\rm dip,0} = R_{\rm NS}^3 B_{\rm dip,0}^2/6$, and $\alpha > 0$. For a given current age $t = t_{\rm SNR}$, the value of t_B that maximizes this power is $t_B = 2t/\alpha$ corresponding to $\tau_{\rm max} = 1 + \alpha/2$ and

$$|\dot{E}_{B,\rm dip}|_{\rm max} = \dfrac{2}{2+\alpha}\dfrac{E_{B,\rm dip}(t)}{t}, \tag{87}$$

which, for $B_{\rm s}(t) = 1.16 \times 10^{14} f^{-1/2}$ G implied from the measured P and $\dot{P}$ values, gives

$$\dfrac{|\dot{E}_{B,\rm dip}|_{\rm max}}{g L_{\rm sd}} = 1.25 \times 10^{-3} g_{50}^{-1} f^{-1} t_{4.5}^{-1}, \tag{88}$$

for fiducial parameter values of $g = 50 g_{50}$ (consistent with the lower limit on g from equation 80 for $\sigma < 1$), $t_{\rm SNR} = 10^{4.5} t_{4.5}$ yr, and $\alpha = 3/2$ (e.g. as $3/2 \lesssim \alpha \lesssim 9/5$ was inferred by Dall'Osso, Granot & Piran 2012). Therefore, the decay of the dipole field clearly fails to supply the needed power that is injected in the nebula, $\langle\dot{E}\rangle = g L_{\rm sd}$.

6.3.2 Decay of a much stronger internal field is needed

Supplying the needed $\langle\dot{E}\rangle = g L_{\rm sd}$ requires a significantly larger power, for which the most viable candidate is the decay of a much larger internal magnetic field within the magnetar, which dominates the total decay rate of the magnetic field, $\dot{E}_B = \dot{E}_{B,\rm dip} + \dot{E}_{B,\rm int} \simeq \dot{E}_{B,\rm int}$. Doing a similar analysis for the decay of the internal field, and replacing $E_{B,\rm dip,0} \to E_{B,\rm int,0}$ and $B_{\rm dip,0} \to B_{\rm int,0}$, equation (87) together with the requirement that $\dot{E}_B \simeq \dot{E}_{B,\rm int} \geq \langle\dot{E}\rangle = g L_{\rm sd}$ (where the inequality accounts for some inefficiency in transferring the magnetic power to that supplying the nebular X-ray luminosity) and therefore $|\dot{E}_{B,\rm int}|_{\rm max} \geq g L_{\rm sd}$, implies a lower limit on the current value of the internal field,

$$B_{\rm int}(t) \geq 3.3 \times 10^{15} g_{50}^{1/2} t_{4.5}^{1/2}\,\rm G, \tag{89}$$

which is significantly larger than the inferred surface dipole field,

$$\dfrac{B_{\rm int}(t)}{B_{\rm dip}(t)} > 28.3 f^{1/2} g_{50}^{1/2} t_{4.5}^{1/2}. \tag{90}$$

A useful constraint on g can be obtained by constraining the value of the internal field $B_{\rm int}$ from the stability criterion of magnetic fields in NSs. Numerical simulations by Braithwaite (2009) show that stable axisymmetric magnetic equilibrium is achieved when both poloidal and toroidal field components contribute, and most importantly, when the ratio of the total energy in the poloidal field

component to the total magnetic energy is between $\mathcal{A}E_{B,\mathrm{int}}/E_G \simeq 10^{-3} \lesssim E_{B,\mathrm{dip}}/E_{B,\mathrm{int}} \lesssim 0.8$, where $\mathcal{A} \sim 10^3$ for NSs and $E_G \simeq 3 \times 10^{53}$ erg is the gravitational binding energy (assuming uniform mass density with $M_{\mathrm{NS}} = 1.4M_\odot$ and $R_{\mathrm{NS}} = 10^6$ cm). By using the lower limit on $E_{B,\mathrm{dip}}/E_{B,\mathrm{int}}$, which is relevant here, we find

$$
\begin{aligned}
B_{\mathrm{int}} \lesssim B_{\mathrm{int,max}} &= \left(\frac{6E_G B_{\mathrm{dip,0}}^2}{\mathcal{A}R_{\mathrm{NS}}^3} \right)^{1/4} \\
&= 6.6 \times 10^{15} B_{\mathrm{dip,0,15}}^{1/2} \, \mathrm{G},
\end{aligned} \tag{91}
$$

for a fiducial value of the initial surface dipole field $B_{\mathrm{dip,0}} = 10^{15}$ G. The currently inferred surface dipole field is smaller than its initial value due to field decay over the age of the magnetar.

Combining equations (89) and (91) one obtains a lower limit on the initial dipole field of $B_{0,\mathrm{dip}} \gtrsim 2.6 \times 10^{14} g_{50} t_{4.5}$ G, which is problematic for scenarios in which the dipole field has grown significantly from its initial value to its present value ($B_s = 1.16 \times 10^{14} f^{-1/2}$ G).

Internal fields as high as $B_M = 10^{16}$–$10^{16.5}$ G are suggested by bursting activity in magnetars (e.g. Turolla et al. 2015) and are needed for powering their quiescent X-ray luminosities (e.g. Dall'Osso, Granot & Piran 2012). If this is the maximum internal field afforded by the NS then, equation (89) yields (for $\alpha = 3/2$) an upper limit on g [using equation (87) and the requirements that $|\dot{E}_{B,\mathrm{dip}}|_{\max} \geq g L_{\mathrm{sd}}$ and $B_{\mathrm{int}}(t) \leq B_{\mathrm{int,max}}$],

$$
\begin{aligned}
g \leq g_{\max} &= \frac{2}{2+\alpha} \frac{R_{\mathrm{NS}}^3 B_{\mathrm{int,max}}^2}{6 L_{\mathrm{sd}} t} \\
&\simeq 2.0 \times 10^2 B_{\mathrm{dip,0,15}} t_{4.5}^{-1} \\
&\simeq 4.65 \times 10^2 B_{M,16}^2 t_{4.5}^{-1} \\
&\simeq 4.65 \times 10^3 B_{M,16.5}^2 t_{4.5}^{-1}.
\end{aligned} \tag{92}
$$

Due to the uncertainty in the value of the actual internal field, we show the above three upper limits on g in Fig. 11.

6.4 The radiative efficiency and electron distribution

Finally, we note that equation (79) can be rewritten as

$$
\epsilon_X \simeq \xi^{-7/2} = \frac{\eta_X(1+\sigma)}{\epsilon_e g} \simeq 0.02 \left(\frac{\epsilon_e}{0.13} \right)^{-1} g_{50}^{-1}, \tag{93}
$$

where $\epsilon_e \simeq 0.13$ and $3.07 < g \lesssim 5 \times 10^3$ would correspond to $2 \times 10^{-4} \lesssim \epsilon_X \lesssim 0.33$. It is hard to achieve a very low ϵ_X given the fairly hard inferred electron power-law index $s \simeq 1.82 \pm 0.24$ and given equation (78), which seem to suggest $\epsilon_X \gtrsim 0.1$ or so. This may be achieved for low values of ϵ_e, which may be possible if most of the particle energy is either in electrons not taking part in the power-law energy distribution radiating in X-rays (e.g. an energetically dominant quasi-thermal energy component, below the observed power-law high-energy tail), or if most of the energy in outflows from the magnetar is baryon rich with most of its energy in protons rather than e^+e^- pairs. Finally, equation (21) can be rewritten as

$$
\epsilon_X \simeq \xi^{-7/2} < 0.33\sigma \left(\frac{\epsilon_e d_4}{0.13} \right)^{-1} f^{-7/2} E_{M,30}^{-7/2}, \tag{94}
$$

which suggests that σ cannot be very low unless ϵ_e is correspondingly low (and g is correspondingly high according to equation 81).

It is important to notice that once the total energy injection into the nebula is no longer dominated by the magnetar's spin-down power, i.e. $g > 1$, then η_X no longer represents the true radiative efficiency, $\eta_{X,\mathrm{true}}$. More generally, the injected power is larger by a factor of g, and therefore the overall radiating efficiency is smaller by the same factor,

$$
\eta_{X,\mathrm{true}} = \frac{\eta_X}{g} = \frac{0.0026 d_4^2}{g_{50}} < 0.042 \frac{\sigma}{1+\sigma} d_4^{-1} E_{M,30}^{-\frac{7}{2}} f^{-\frac{7}{2}}. \tag{95}
$$

Note that this significantly lowers the required radiative efficiency of the MWN, making it more compatible with efficiencies inferred for PWNe.

7 THE GEV AND TEV EMISSION

An extended TeV source with radius 9–10.2 arcmin [corresponding to a physical size of $(10.5$–$11.9)d_4$ pc] was discovered at the centre of SNR W41 (Aharonian et al. 2006). Additionally, the *Fermi* Large Area Telescope (LAT) found a high-energy ($E > 100$ MeV) extended source, similar in size to the TeV source, coincident with the same SNR (e.g. Nolan et al. 2012). Spectral analysis of the *Fermi* LAT data showed an approximately flat $E^2 dN/dE \propto E^{2-\Gamma}$ spectrum with photon index $\Gamma \simeq 2.15$ and GeV luminosity $L_{\mathrm{GeV}} \simeq 1.45 \times 10^{35} d_4^2$ erg s^{-1} in the 0.1–100 GeV energy range (Abramowski et al. 2015). The same work shows that the TeV extended region is slightly softer with $\Gamma \simeq 2.6$ and has a (1–30) TeV luminosity $L_{\mathrm{TeV}} \simeq 1 \times 10^{34} d_4^2$ erg s^{-1}.

There are three plausible scenarios that can explain GeV–TeV emission from SNRs, namely (i) hadronic emission by CR protons (CR$p + p \rightarrow p + p + \pi^0$) followed by the decay of neutral pions ($\pi^0 \rightarrow 2\gamma$), (ii) inverse-Compton scattering of soft seed photons (CMB and/or NIR Galactic background) by energetic electrons injected by the magnetar wind ($e + \gamma \rightarrow e + \gamma'$), and (iii) non-thermal bremsstrahlung emission from CR electrons directly accelerated by the SN forward blast wave (CR$e + p \rightarrow e + p + \gamma$). We examine all three cases of γ-ray production next and provide simple estimates of the energetics which are then used to ascertain the feasibility of such processes in the present case.

7.1 Hadronic emission

SNRs are thought to be the dominant contributors to the Galactic CR flux up to the 'knee' at $E = 10^{15}$ eV. The Galactic production rate of CRs can be explained if $\eta_{\mathrm{CR}} \sim 10$ per cent of the SN energy (η_{CR} is the cosmic ray acceleration efficiency and $E_{\mathrm{SN}} \sim 10^{51}$ erg) goes into accelerating CRs at SN blast waves (e.g. Aharonian 2004). Many middle-age SNRs ($t_{\mathrm{SNR}} \sim 10^5$ yr) found in dense environments hosting GMCs have been observed as bright GeV and TeV sources. In fact, SNRs interacting with GMCs, as inferred from the detection of OH masers (e.g. Frail et al. 2013), constitute the dominant fraction of Galactic GeV SNRs (e.g. Thompson, Baldini & Uchiyama 2012). An estimate of the GeV/TeV flux from the hadronic component can be obtained with simple arguments. At high energies ($E_\gamma > 1$ GeV), the γ-ray spectrum is spectrally similar to the parent distribution of CR protons (e.g. Aharonian & Atoyan 1996). Then, for a power-law distribution of CR protons

$$
n_p(E_p) = K_p E_p^{-s_p} \tag{96}
$$

where the normalization K_p is obtained by assuming that the CR energy density $U_{\mathrm{CR}} \sim 3\eta_{\mathrm{CR}} E_{\mathrm{SN}}/4\pi R_{\mathrm{SNR}}^3$ (e.g. Drury, Aharonian &

Völk [1994]), the γ-ray photon emissivity [phs^{-1} cm^{-3} erg^{-1}] is (e.g. Aharonian [2004])

$$J_\gamma(E_\gamma) = \int_{E_{p,\min}}^{\infty} \frac{2cn_{GMC}\sigma_{pp}(E_p)\eta_A n_p(E_p)}{\sqrt{(E_p - m_p c^2)^2 \kappa_\pi^2 - m_\pi^2 c^4}} dE_p \quad (97)$$

where the threshold proton energy for π^0 production is $E_{p,\min} = m_p c^2 + \kappa_\pi^{-1}(E_\gamma + m_\pi^2 c^4/4E_\gamma)$, m_p and m_π are the proton and π^0 masses, $\eta_A \simeq 1.5$ includes the contribution of nuclei other than protons towards the production of γ-rays (Dermer [1986]), $\kappa_\pi = 0.17$ is the mean fraction of proton's kinetic energy transferred to π^0-meson per collision, and n_{GMC} is the target proton number density (assumed uniform) in the GMC. The p–p inelastic collision cross-section is given by (e.g. Cheng & Romero [2004])

$$\sigma_{pp}(E_p) \approx 30 \left[0.95 + 0.06 \ln \left(\frac{E_p}{GeV} \right) \right] \text{mb} \quad (98)$$

which is assumed to vanish below proton kinetic energy $E_p - m_p c^2 < 1$ GeV. Since σ_{pp} only has a weak logarithmic dependence on proton energy, the γ-ray spectrum is expected to reproduce the spectrum of the parent proton population. The integrated γ-ray photon flux in the GeV-region for $s_p = 2.15$, $E_1 = 1$ GeV and $E_2 = 100$ GeV is

$$\Phi_\gamma = \int_{E_1}^{E_2} \frac{J_\gamma(E_\gamma')V_{TeV}}{4\pi d^2} dE_\gamma' \simeq 8.16 \times 10^{-10} A \, \text{cm}^{-2} \, \text{s}^{-1} \quad (99)$$

where $A = \eta_{CR}E_{SN,51}n_{GMC}d_4^{-2}$. This agrees with the photon flux measured by *Fermi* (H.E.S.S. Collaboration [2015]) in the (1–100) GeV region $\Phi \approx 8.93 \times 10^{-9}$ cm^{-2} s^{-1} for $\eta_{CR} \sim 0.1$ and $n_{GMC} \sim 109$ cm^{-3}. This is a reasonable estimate of the target proton number density in light of the fact that Tian et al. ([2007]) find a number density of $\sim 10^3$ cm^{-3} for the GMC associated with W41 from ^{13}CO observations.

Above ~ 1 GeV, CR protons mainly lose energy to inelastic proton–proton collisional interaction over a characteristic time-scale (e.g. Gabici, Aharonian & Casanova [2009])

$$\tau_{pp} = (c\eta_A\sigma_{pp}n_{GMC})^{-1} = 2.3 \times 10^5 n_2^{-1} \, \text{yr}, \quad (100)$$

where $n_{GMC} = 10^2 n_2$ cm^{-3}. The propagation of CR protons, which are accelerated at the SN blast wave, into the ISM is governed by their energy-dependent diffusion, with diffusion coefficient (e.g. Gabici et al. [2009])

$$D(E_p, B_{ISM}) = 10^{28} \left(\frac{E_p}{10 \, \text{GeV}} \right)^{\frac{1}{2}} \left(\frac{B_{ISM}}{3 \, \mu G} \right)^{-\frac{1}{2}} \text{cm}^2 \, \text{s}^{-1}. \quad (101)$$

Assuming the SNR W41 is directly in contact with the nearby GMC, as inferred from the OH maser emission, the penetration depth of CR protons into the GMC is

$$\ell_p \sim \sqrt{6D(E_p, B_{ISM})\tau_{pp}} = \frac{0.2 \, \text{kpc}}{\sqrt{n_2}} \left(\frac{E_p/10 \, \text{GeV}}{B_{ISM}/5 \, \mu G} \right)^{\frac{1}{4}}. \quad (102)$$

The above estimate shows that the CR protons are capable of reaching distances much larger than the size of the SNR (before they lose most of their energy), for the assumed target proton density. As the protons cool only after reaching a large displacement ℓ_p and traversing an even larger distance (of $c\tau_{pp} \sim 72 n_2^{-1}$ kpc), then the relevant density is the mean value over the region they have traversed in, or the cumulative gramage (or path integral over n_{GMC}) along their trajectory. Most of the p–p collisions and corresponding energy loss that goes to producing GeV/TeV emission via neutral pion decay tend to occur in the regions where n_{GMC} is largest, i.e. in dense

clumps within the GMC. Since the CR proton-illuminated high-density clump is located behind the SNR (e.g. Tian et al. [2007]), the smaller ($R_{GeV/TeV} \ll \ell_p$) observed size of the GeV/TeV is consistent with this inference.

The proton energy distribution power-law index $s_p \simeq 2$ agrees with that obtained from *Fermi* acceleration at the SN blast wave. The same applies to accelerated leptons and radio observations of SNR W41 find a photon index of $\Gamma_{rad} \simeq 1.5 - 1.6$ (e.g. Kassim [1992]), which again yields a particle energy distribution power-law index of $s_e = 2\Gamma_{rad} - 1 = 2.0$–2.2. However, at high energies the GeV/TeV spectrum shows a break around ~ 100 GeV, with $\Gamma_{TeV} \simeq 2.6$ in the TeV region. Such breaks are on average observed in other SNRs with associated GeV/TeV emission (e.g. Hewitt, Yusef-Zadeh & Wardle [2009]) where the softening of the high-energy spectrum can be attributed to (i) overlap of π^0-decay and non-thermal bremsstrahlung spectral components, or (ii) diffusion of CR protons in the neighbouring dense molecular clouds. In fact, in the case of SNR W41, using an energy-dependent diffusion coefficient $D(E_p) \propto E_p^{0.6}$, Li & Chen ([2012]) were able to explain the GeV/TeV spectrum with hadronic emission and high target proton density $n_{GMC} \gg 1$ cm^{-3}. Lower energy protons that produce GeV photons experience smaller diffusion lengths as compared to the higher energy TeV producing protons. Thus, their energy distribution remains close to that of freshly accelerated protons, whereas TeV producing protons are subject to diffusive softening.

7.2 Leptonic emission

7.2.1 Inverse Compton

High-energy electrons present in the MWN can also IC scatter softer seed photons with energy E_s to much harder energies. The high-energy γ-ray emission around Swift J1834 is dominated by GeV photons with an order of magnitude larger radiated power than TeV photons. The νF_ν flux for the GeV emission peaks around a few GeV, then the Lorentz factor of the electrons needed to IC scatter softer seed photons such as the CMB, with mean energy $E_{CMB} = 0.63$ meV, and NIR Galactic background, with typical energy $E_{NIR} \simeq 0.1$ eV, must be

$$\gamma_{IC} = \left(\frac{3E_{GeV}}{4E_s} \right)^{1/2} = \begin{cases} 1.2 \times 10^5 E_{2GeV}^{1/2} & (E_s = E_{NIR}) \\ \\ 1.5 \times 10^6 E_{2GeV}^{1/2} & (E_s = E_{CMB}) \end{cases} \quad (103)$$

where we normalized the GeV photon energy $E_{GeV} = 2E_{2GeV}$ GeV. Their inverse-Compton cooling time is $t_{IC} = 3m_e c/(4\sigma_T \gamma_{IC} U_s)$ where U_s is the energy density of the relevant seed photon field, either $U_{CMB} = 4.17 \times 10^{-13}$ erg cm^{-3} or $U_{NIR} \approx 10^{-13}$ erg cm^{-3} (Porter & Strong [2005]), while their energy is $E_e \equiv L_{IC}t_{IC}$ according to the definition of t_{IC}, so that identifying $L_{IC} = L_{GeV}$ we obtain

$$E_e = L_{GeV}t_{IC} = \begin{cases} 3.6 \times 10^{50} d_4^2 E_{2GeV}^{-1/2} \, \text{erg} & \text{(NIR)} \\ \\ 6.9 \times 10^{48} d_4^2 E_{2GeV}^{-1/2} \, \text{erg} & \text{(CMB)}. \end{cases} \quad (104)$$

These requisite energies are larger than the total energy in the nebula (see equation 50) in both scenarios considered in this work, where $E(R_{GeV}) = E(R_X)R_X/R_{GeV} = 0.18E(R_X) < E_e$ for an average GeV region size $R_{GeV} = 11.2d_4$ pc.

Also, X-ray emitting electrons that have Lorentz factors

$$\gamma_X = 1.1 \times 10^8 E_2^{1/2} B_{15 \, \mu G}^{-1/2} \quad (105)$$

can be particularly powerful in boosting seed CMB photons to TeV energies

$$E_\gamma = \frac{4}{3}\gamma_X^2 E_{CMB} = 9.8 B_{15\,\mu G}^{-1} E_2 \text{ TeV} \tag{106}$$

where we have made use of the relation $E_X = \hbar e B \gamma_e^2/(m_e c)$. Note that this energy is still below the Klein–Nishina energy.[2] Given the hard photon index measured in X-rays in the inner nebula, $\Gamma_{in} = 1.41 \pm 0.12$ in the 0.5−30 keV energy range, one would expect a rising or at most flattish νF_ν slope at TeV energies, which is in contrast with the photon index measured by H.E.S.S. of $\Gamma_{TeV} = 2.64 \pm 0.06$ in the 0.2−30 TeV energy range (Abramowski et al. 2015). Moreover, in this picture the size of the TeV source in this case should be much smaller than observed, as the electrons that inverse-Compton scatter the CMB photons into the H.E.S.S. energy range are fast cooling, and their cooling length is $\ll R_{TeV} \approx 11 d_4$ pc (see Fig. 10, bottom panel) and in particular it should be smaller than the GeV source size, while the two are measured to be similar.

7.2.2 Non-thermal bremsstrahlung

SNRs in the Sedov phase are capable of accelerating protons and electrons to TeV energies at the forward blast wave (e.g. Baring et al. 1999). If the ISM density is high enough, then these primary CR electrons can become the dominant contributors to the GeV emission from SNRs that are in close proximity to GMCs. The cooling time of electrons emitting bremsstrahlung radiation only depends on the number density of target protons (e.g. Aharonian 2004)

$$t_{BR} = \gamma_e \left(\frac{d\gamma_e}{dt}\right)^{-1} = \frac{X_0}{c m_p n_{GMC}} = 4.5 \times 10^5 n_2^{-1} \text{ yr}, \tag{107}$$

where we have normalized $n_{GMC} = 10^2 n_2$ cm^{-3} (see Section 7.1), and $X_0 \approx 71$ g cm^{-2} is the radiation length over which the electron loses all but $1/e$ of its energy to bremsstrahlung photons. Comparing this time to the synchrotron cooling time, we find that bremsstrahlung losses are important for electrons below

$$\gamma_{BR} = 2.1 \times 10^6 n_2 \left(\frac{B_{ISM}}{5\,\mu G}\right)^{-2}, \tag{108}$$

where the ISM magnetic field is only a few μG. However, at energies below $\approx 700 m_e c^2$ ionization losses become dominant. For $\gamma_e \gg 1$, the number distribution of CR electrons assumes a power law $N(E_e) = K_e E_e^{-s_e}$, where the normalization can be expressed using the electron-to-proton number ratio $\Phi_{ep} < 1$, such that for $E_{e,\,max} \gg E_{e,\,min}$, $s_e > 1$, and $s_p > 2$,

$$K_e = \frac{(s_e-1)(s_p-2)\Phi_{ep}\eta_{CR} E_{SN}}{(s_p-1)} \left(\frac{E_{e,\,min}^{s_e-1}}{E_{p,\,min}}\right), \tag{109}$$

where $E_{e,\,min}$ and $E_{p,\,min}$ are, respectively, the minimum energies to which electrons and protons are accelerated by the blast wave. Just like the hadronic emission, bremsstrahlung photons retain the same spectral shape as the parent electron distribution. Then for $s_e = 2 \simeq \Gamma_{GeV}$ corresponding to the photon index of the GeV emission,

---

[2] This is the case up to $E_{IC} \sim 310$ TeV that corresponds to $\gamma_e = 6.1 \times 10^8$, which is slightly larger than $\gamma_{max} \simeq 4.9 \times 10^8 f^{-1/2}$, so that Klein–Nishina effects are unimportant here for CMB seed photons. $E_{KN} \sim \gamma_X m_e c^2 = 55 (E_2/B_{15\,\mu G})^{1/2}$ TeV. IC scattering of NIR Galactic background photons by the same X-ray emitting electrons is Klein–Nishina suppressed for $\gamma_e > 3.8 \times 10^6$.

and assuming that after one radiation length the electron energy E_e is converted into photon energy E_γ, the emitted power in the GeV band ($E_1 = 0.35$ GeV and $E_2 = 100$ GeV) is (Gaisser, Protheroe & Stanev 1998)

$$L_{GeV} \approx \int_{E_1}^{E_2} \frac{N(E_\gamma)E_\gamma}{t_{BR}} dE_\gamma = \frac{K_e}{t_{BR}} \ln\left(\frac{E_2}{E_1}\right)$$
$$\approx 1.5 \times 10^{35} \left(\frac{\Phi_{ep} n_{GMC} E_{e,\,min}}{E_{p,\,min}}\right) \text{ erg s}^{-1}. \tag{110}$$

The term in the parenthesis can easily be of the order of unity, in which case the bremsstrahlung emission from CR electrons can power the GeV emission when $n_{GMC} \gg 1$. However, a detailed treatment of particle acceleration and diffusion can shed more light on this possibility.

8 DISCUSSION

The confirmation of the first ever wind nebula around a magnetar in Swift J1834.9−0846 has opened up a new avenue of investigation into the mysterious nature of magnetars. We have carefully analysed the properties of this MWN, along with its central magnetar and associated SNR (W41) and GeV/TeV source, in order to improve our understanding of this system and the magnetar's activity pattern. Our main conclusions can be summarized as follows (while at the end of the discussion we elaborate more on some of these points).

(i) The X-ray nebula emission and energy budget:

(a) Comparison of the energy in the magnetic field and in the X-ray synchrotron emitting $e^+ e^-$ pairs (with Lorentz factor γ_X) in the nebula implies a nebular magnetic field $B \sim (5-30)\sigma_e^{2/7}$ μG.

(b) The maximum magnetar polar-cap voltage difference V_0 implies a maximum electron Lorentz factor $\gamma_{max} \lesssim 10^{8.5}$, so that in order for $E_{syn}(\gamma_{max}) \gtrsim 30$ keV the nebular magnetic field must be $B \gtrsim 11$ μG.

(c) In such a B-field, $t_{syn}(\gamma_X) \ll t_{SNR}$ so we see X-rays from fast-cooling electrons that cool radiatively in much less than the system's age.

(d) This allows us to write the detailed energy balance equation for the X-ray emitting electrons, which leads to a constraint on $g = \langle \dot{E}\rangle/L_{sd} > g_{min} = 3.07 \frac{1+\sigma}{\sigma} d_4^3 E_{M,30}^{7/2} f^{7/2}$ (equation 80 and Fig. 11) where $\langle \dot{E}\rangle$ is the magnetar's long-term mean energy output in outflows (quiescent MHD wind + sporadic outbursts).

(e) Altogether, the result that $g > g_{min} > 3.1$ clearly implies that the MWN is not powered predominantly by the magnetar's spin-down-powered wind, but instead requires an additional energy source that contributes most of its energy.

(f) The most viable candidate energy source is the decay of the magnetar's magnetic field. We show that the decay of its dipole field alone is not enough, and a significantly larger (by a factor of $\sim 10^2$–10^3) energy reservoir is needed. The most natural candidate for the latter is the magnetar's internal magnetic field, which has to be $\gtrsim 30$ times larger than its dipole field.

(g) If the spin-down torque is dominated by a powerful steady particle wind that opens up the dipole field lines thus increasing the field at the light cylinder, then this gives $n \approx 1$ but implies a lower true surface dipole field. However, this would in turn imply an even more extreme ratio for $E_{B,\,dip}/E_{B,\,int} = (B_{dip}/B_{int})^2$, which might be susceptible to instabilities, thus arguing against such a solution.

(h) By assuming a maximum allowed initial internal field strength (on theoretical grounds) of $B_{int,\,max} \sim 10^{16}$–$10^{16.5}$ G we

obtain an upper limit on g of $g \lesssim g_{max} \sim 5 \times (10^2$–$10^3)$ (see equation 92).

(i) The SNR age is inferred to be $t_{SNR} \sim 5 - 100\,$kyr, where the main uncertainty arises from the external density.

However, the magnatar's spin-down age is significantly lower, $\tau_c = 4.9\,$kyr. Reconciling the two ages requires $\langle L_{sd} \rangle / L_{sd} \sim \tau_c / t_{SNR} \sim 0.05 - 1$, suggesting either a low breaking index ($1.1 \lesssim n \lesssim 2$) or a widely fluctuation spin-down torque and thus $\dot{P}$ with $\langle \dot{P} \rangle / \dot{P} \sim 0.05 - 1$.

(ii) The true X-ray radiative efficiency is the fraction of the total injected energy $\langle \dot{E} \rangle = g L_{sd}$ that is radiated in X-rays, and it is smaller than $\eta_X = L_{X,\,tot}/L_{sd} \simeq 0.13$ (which assumes energy input only from the spin-down power) by a factor of g: $\eta_{X,true} = \eta_X/g = 2.6 \times 10^{-3} g_{50}^{-1} < 0.042$. Therefore, while the naive estimate for the efficiency ($\eta_X \simeq 0.13$) appears to be very high as compared to other PWNe, the true efficiency is considerably lower and consistent with that of PWNe.

(iii) The short cooling time of the X-ray synchrotron emitting shock-accelerated e^+e^- pairs implies that their diffusion dominates over their advection throughout almost all of the MWN. Their diffusion-dominated cooling length approximately matches the observed size of the MWN, which may naturally explain the spectral softening between the inner and outer parts of the X-ray nebula.

(iv) It is very hard to explain the GeV/TeV emission as inverse-Compton emission from the MWN:

 NIR Galactic background seed photons require a minimal energy in the GeV emitting electrons of $E_e = 3.6 \times 10^{50} d_4^2 E_{2GeV}^{-1/2}\,$erg, which is very challenging energetically, unless the initial surface field was $B_0 \lesssim 10^{12}\,$G, which would give a much longer initial spin-down time t_0, where most of the energy from the central pulsar would be injected until late times and, consequently, suffer less adiabatic losses.

 For the CMB seed photons this minimal energy is lower, $\simeq 7 \times 10^{48}\,$erg (as both the photon energy density U_γ and the electron Lorentz factor γ_e are higher). Even this energy requires a fairly large initial spin-down time ($t_0 \gtrsim 10^{1.5}\,$yr) and short initial spin period ($P_{0,\,-3} \lesssim$ a few), and in turn an initial dipole field $B_0 \lesssim 10^{12.5}\,$G, which is much less than the current value, and very low for a magnetar. This would require a significant field growth. While such a scenario is discussed in Appendix A, its physical plausibility is highly debated.

 Moreover, even for CMB seed photons, because of the wide power-law electron energy distribution implied when accounting also for the X-ray emission, the inverse-Compton spectral peak should be much wider than observed.

(v) The GeV/TeV emission is much more likely of hadronic origin (e.g. Li & Chen 2012), from interactions of CRs accelerated at the SNR shock with the nearby GMC (which has $n_{GMC} \sim 10^3\,$cm^{-3}). This scenario is also supported by the detection of OH maser emission discovered at the centre of the GeV/TeV region. The energetics and spectrum of the emission, as well as its location and size, find a much more plausible explanation in this scenario.

It is only natural to ask why similar MWNe were not detected so far around other magnetars – is Swift J1834 indeed unique in this respect? One possibility is that such MWNe exist around other magnetars but their detection requires more sensitive observations due to their relatively low X-ray emission level. In particular, an extended X-ray emission was recently reported by Israel et al. (2016) around SGR J1935+2154 and although they favour a dust scattering halo origin, they cannot rule out a MWN origin. The latter option

would represent the detection of a second MWN, which would double the current MWN population due to the currently very small number statistics. This obviously stresses the large observational uncertainty at present on the fraction of magnetars that power a MWN.

Alternatively, MWNe might indeed be intrinsically relatively rare and exist only around a reasonably small fraction of magnetars. Let us therefore consider the possible physical characteristics that might impact the formation of a wind nebula around a magnetar, as well as its X-ray brightness. The factors that might determine the existence of a MWN around a magnetar and its X-ray brightness, and how they vary between different magnetars, may be broadly divided into two main classes: intrinsic magnetar properties and external environmental properties.

Important intrinsic magnetar properties for this purpose are its initial spin period, P_0, which determines its initial spin energy ($E_0 = \frac{1}{2} I \Omega_0^2 = 2\pi^2 I P_0^{-2}$) as well as its initial surface dipole field strength, B_0, and its evolution throughout its lifetime that together determine the rotational energy loss rate, $\dot{E}_{rot}$. The latter is essentially the energy injection rate into a MWN by the magnetar's quiescent rotation-powered MHD wind, $L_{sd} = |\dot{E}_{rot}|$, into which its rotational energy is channelled. In addition, the magnetar's wind pair multiplicity can be very high due to the high magnetic pair opacity in the inner magnetosphere, which enhances the energy in the wind component over radiation. Therefore, the high e^+e^- pair injection rate into the MWN and its evolution over the magnetar's lifetime affect the MWN's radiation and radiative energy loss rate through its effect on the electron energy distribution.

The final intrinsic magnetar property worth mentioning in this context, which naturally leads us to the environmental effects or properties, is its natal kick velocity, v_{SGR}. For Swift J1834 one can constrain its component on the plane of the sky, $v_{\perp,\,SGR}$, through the fact that it is located at the centre of the SNR W41. Its location is constrained to be $\lesssim (0.05 - 0.1) R_{SNR}$ from the SNR's centre, which for an SNR/SGR age of t_{SNR} implies $v_{\perp,\,SGR} \lesssim (30 - 60) d_4 (t_{SNR}/10^{4.5}\,\mathrm{yr})^{-1}\,$km s^{-1}. It is quite reasonable that most magnetars have larger natal kick velocities, and therefore exit their host SNR at a fairly early stage (soon after the SNR's velocity drops below v_{SGR}). In such a case once the magnetar exits its SNR then its wind is no longer confined by the SNR, and it instead forms a bow-shock structure due to its motion relative to the external medium.

This appears to be the case for SGR 1806−20, from a detailed modelling of the radio nebula that was produced by its 2004 Dec. 24 giant flare (Granot et al. 2006). In that system the bright radio emission at ∼1 week after the giant flare is attributed to a collision between a mildly relativistic outflow ejected from the magnetar during the giant flare and the thin bow-shock structure that is produced by its quiescent wind and systemic motion relative to the external medium outside of its birth SNR. Its systemic velocity that is identified with its natal kick velocity was inferred to be $v_{SGR} \sim 250 n_0^{-1/2}\,$km s^{-1} (Granot et al. 2006). Later, the proper velocity of SGR 1806−20 was measured through its near-infrared (NIR) emission (Tendulkar, Cameron & Kulkarni 2012) to be $v_{\perp,\,SGR} = 350 \pm 100\,$km s^{-1} for an assumed distance of $d = 9 \pm 2\,$kpc to this source, which corresponds to $v_{\perp,\,SGR} \approx 580 d_{15}\,$km s^{-1} for a distance of $d = 15 d_{15}\,$kpc to this source that is well within the inferred range. Since $v_{SGR} \geq v_{\perp,\,SGR}$ and one generally expects $v_{SGR} \gtrsim v_{\perp,\,SGR}$, we can parametrize $v_{SGR} = \kappa v_{\perp,\,SGR} \approx 580 \kappa d_{15}\,$km s^{-1}. When combined with the results of Granot et al. (2006), this would imply a density around SGR 1806−20 of $n_0 \sim 0.2 \kappa^{-2} d_{15}^{-2}\,$cm^{-3}, as well as an outflow kinetic energy $E_{ej} \sim 7 \times 10^{45} \kappa^{-2} d_{15}^3\,$erg, and

mass $M_{\rm ej} \sim 5 \times 10^{25} \kappa^{-2} d_{15}$ g. Granot et al. (2006) also obtain an independent limit on the ejected mass of $M_{\rm ej} \gtrsim 10^{25} d_{15}^{0.5}$ g, which implies $\kappa \lesssim 2.2 d_{15}^{0.25}$, $v_{\rm SGR} \lesssim 1300 d_{15}^{1.25}$ km s^{-1}, $n_0 \gtrsim 0.1 d_{15}^{-2.5}$ cm^{-3}, and $E_{\rm ej} \gtrsim 1.4 \times 10^{45} d_{15}^{2.5}$ erg. For SGR 1900+14, Tendulkar et al. (2012) measured in a similar manner a proper velocity of $v_{\perp,\,\rm SGR} = 130 \pm 30$ km s^{-1} for an assumed distance of $d = 12.5 \pm 1.7$ kpc to this source.

This demonstrates that environmental effects can be very important in determining whether a MWN is formed or not, and tightly relate to the magnetar's natal kick velocity, $v_{\rm SGR}$ – an intrinsic property. For a low $v_{\rm SGR}$ the magnetar remains within its parent SNR for a long time, and the SNR confines the magnetar's shocked MHD wind, thus enabling the production of a prominent MWN. On the other hand, for a high $v_{\rm SGR}$ the magnetar exits its parent SNR early on, and then its wind is no longer effectively confined after being shocked due to its interaction with the external medium, and instead it forms a bow-shock structure through which the shocked wind flows at a fraction of its light crossing time.[3] Therefore, there is no efficient accumulation of energy and the emission from the bow-shock system tends to be dimmer and harder to detect than from a MWN for the same wind power. While a good part of the wind power goes into shocking the external medium in a bow-shock system, the composition of the latter is predominantly electrons and protons, and therefore both the overall radiative efficiency and the fraction of the energy that is radiated in the X-ray range, $\eta_{\rm X}$, are typically lower than for a e^+e^- pair plasma composition in the shocked magnetar MHD wind with a MWN. Moreover, the external density affects the evolution of the SNR and MWN as it does for PWNe (in particular affecting their size at a given age or age corresponding to a given size), as well as the size of the bow-shock structure for a given systemic velocity and wind power.

Another case in which it can be hard to confine a MWN is when the initial rotational energy exceeds the initial SN kinetic energy, $E_0 = \frac{1}{2} I \Omega_0^2 > E_{\rm SN}$. For a canonical $E_{\rm SN} \approx 10^{51}$ erg, this corresponds to $P_0 \lesssim 4 - 5$ ms, so it is expected to hold for the α–ω dynamo scenario for the formation of a magnetar strength magnetic field in the newly born NS, which requires $P_0 \lesssim 3$ ms (Duncan & Thompson 1992). For such rapid initial rotation rates the initial spin-down time t_0 is very short for magnetar strength surface dipole fields (see equation 10). For $B_0 \gtrsim 10^{15}$ G it can correspond to the duration of a long GRB, and produce a sufficiently large initial power, $L_0 \approx E_0/t_0 > 10^{50}$ erg s^{-1}, which launches a relativistic jet that can penetrate the stellar envelope and potentially power a long GRB at large distances. Moreover, in such a case the jet channels most of the rotational energy well outside of the stellar envelope (e.g. Bromberg et al. 2014; Granot et al. 2015; Bromberg & Tchekhovskoy 2016) and hence outside of the SNR shell that forms later on after the quasi-spherical supernova shock crosses the stellar envelope, while only a small fraction of the jet's power contributes to enhance the supernova explosion kinetic energy. While the channel initially cleared by the jet might get clogged at later times, enabling the formation of a confined wind nebula, by such a later time only a small fraction of the initial rotational energy is left in the magnetar, so that the energy injected into such a MWN would be correspondingly smaller.

For a lower B_0 and correspondingly higher t_0, the magnetar wind can potentially power other transient events such as ultra-long GRBs

---

[3] Unless shear instabilities across the contact discontinuity separating it from the shocked external medium significantly slow it down to speeds much smaller than its relativistic sound speed.

or ultra-luminous supernovae (e.g. Metzger et al. 2015, and references therein). For sufficiently low B_0 and high t_0 the jet might eventually not be able to penetrate the stellar envelope, and all of the initial rotational energy may be initially channelled into a wind nebula. However, when $E_0 > E_{\rm SN}$ the stellar envelope is initially swept-up by the wind until the cumulative wind energy $L_0 t$ exceeds the envelope's initial kinetic energy $E_{\rm SN}$ at $t_{\rm c}$, and then it is accelerated until it acquires most of the wind energy $\sim E_0$ at $t \sim t_0$. At $t_{\rm c} < t < t_0$ the SNR shell is accelerated as $R_{\rm SNR} \propto t^{3/2}$ and is susceptible to a strong Rayleigh–Taylor instability, which may fragment the SNR shell, potentially to the extent that most of the shocked pulsar wind might be able to penetrate between the fragments and escape out of the SNR shell altogether. While the shell might be mended at later times, most of the initial rotational energy might escape by then, and again this might result in a smaller injected energy that remains in a MWN. Nonetheless, since millisecond initial spin periods correspond to very high $E_0 \simeq 2 \times 10^{52} P_{0,-3}^{-2}$ erg, even a small fraction of such an energy that might remain to power a MWN might still be sufficient for such a MWN to be detectable.

Energy injection by burst-associated outflows is the most natural candidate. This may naturally occur if the mean energy in such outflows is comparable to the radiative energy observed from these bursts. For the latter, the distribution is compatible with $dN/dE \propto E^{-5/3}$ (where N is the number of bursts and E is their radiated energy) expected for self-organized criticality (e.g. Cheng et al. 1996; Göğüş et al. 1999, 2000; Prieskorn & Kaaret 2012). This might suggest that the total energy output (which scales as $E^2 dN/dE$) is dominated by the largest events – the rare giant flares (although it is possible that such giant flares may comprise a separate component that is not the high-energy tail of the self-organized critical phenomenon and are isolated events). However, the uncertainty on the power-law index of dN/dE could accommodate a flat $E^2 dN/dE$ distribution or even one that slightly goes down with energy, so it is not clear whether the radiative energy output, let alone that energy output in the associated outflows, is dominated by a small number of giant flares, or by a much larger number of much weaker events. Such outflows can contribute to the high X-ray efficiency both directly (through X-ray radiation from the outflow itself) and indirectly by mechanically transferring a good part of their energy to the relativistically hot shocked e^+e^- pair wind already present in the MWN, which may be able to radiate this energy more efficiently into the X-ray energy range. The latter potentially higher $\eta_{\rm X}$ in the e^+e^- shocked wind in the MWN compared to the outflow itself is motivated by evidence for a different composition of the outflow itself. A detailed modelling of the radio nebula produced by the outflow from the 2004 Dec. 24 giant flare from SGR 1806−20 (Granot et al. 2006) suggests that this outflow contained a significant mass in baryons, as briefly mentioned above.

The MWN around Swift J1834 can provide an estimate of the long-term mean energy output in outflows, $\langle \dot{E} \rangle \approx g_{50} \times 10^{36}$ erg s^{-1}, which is fairly high. If $\langle \dot{E} \rangle$ is indeed dominated by outflows from giant flares, say each of mean energy $E = 10^{45.5} E_{45.5}$ erg, then this would correspond to a rate for such giant flares of one per $E/\langle \dot{E} \rangle = 100 g_{50}^{-1} E_{45.5}$ yr, which is compatible with the rate estimates of giant flares from the known SGR population given three giant flares observed so far from different SGRs. We note, however, that both the rate of giant flares and their mean energy can gradually change with the SGR's age, and that the three recorded giant flares are from SGRs that appear to be younger than Swift J1834, while $\langle \dot{E} \rangle$ corresponds to the mean over a fraction of its current age and therefore should represent the current mean giant flare rate and energy in outflows. Therefore, detailed studies of MWNe could help

constrain (e.g. through the parameter *g*) the mean energy output in such outflows for a given object at close to its current age, thus effectively averaging over hundreds to thousands of years of its past activity. In this way, the MWN acts as a calorimeter that enables us to probe the history of the magnetar's activity and its energy budget.

The rich information that can be extracted from observations of a MWN provides strong motivation to search for additional MWNe around other known magnetars. We expect better prospect for detection of MWNe around magnetars that are still within their birth SNRs, though it is still worth looking for MWNe also around magnetars without a clear SNR association. Detailed MWN observations are a very promising tool for in-depth studies of magnetar environments, evolutionary links, and past activity, which may shed light on the fundamental differences between magnetars and other types of NSs.

ACKNOWLEDGEMENTS

REFERENCES

Abramowski A. (H.E.S.S. Collaboration) et al., 2015, A&A, 574, 27
Aharonian F., 2004, Very High Energy Cosmic Gamma Radiation: A Crucial Window on the Extreme Universe. World Scientific Publishing, River Edge, NJ
Aharonian F. A., Atoyan A. M., 1996, A&A, 309, 917
Aharonian F. et al., 2008, A&A, 486, 829
Aharonian F. et al., (H.E.S.S Collaboration) 2006, ApJ, 636, 777
Anderson G. E. et al., 2012, ApJ, 751, 53
Atoyan A. M., Aharonian F. A., Völk H. J., 1994, Phys. Rev. D, 52, 3265
Baring M. G., Ellison D. C., Reynolds S. P., Grenier I. A., Goret P., 1999, ApJ, 513, 311
Barthelmy S. D. et al., 2008, The Astron. Telegram, 1676, 1
Blandford R. D., McKee C. F., 1976, Phys. Fluids, 19, 1130
Blitz L., 1993, in Levy E. H., Lunine J. I., eds, Protostars and Planets III. Univ. of Arizona, Tucson, p. 125
Blondin J. M., Chevalier R. A., Frierson D. M., 2001, ApJ, 563, 806
Braithwaite J., 2009, MNRAS, 397, 763
Bromberg O., Tchekhovskoy A., 2016, MNRAS, 456, 1739
Bromberg O., Granot J., Lyubarsky Y., Piran T., 2014, MNRAS, 443, 1532
Camilo F., Ransom S. M., Halpern J. P., Reynolds J., 2007, ApJ, 666, L93
Castro D., Slane P., 2010, ApJ, 717, 372
Cheng K. S., Romero G. E., 2004, in Cheng K. S., Romero G. E., eds, Cosmic Gamma-Ray Sources. Astrophys. Space Sci. Libr. 304, Kluwer, Dordrecht
Cheng B., Epstein R., Guyer R., Young A. C., 1996, Nature, 382, 518
Chevalier R. A., 2004, Adv. Space Res., 33, 456
Cioffi D. F., McKee C. F., Bertschinger E., 1988, ApJ, 334, 252
Cline T. L. et al., 1980, ApJ, 237, L1
Colpi M., Geppert U., Page D., 2000, ApJ, 529, L2
Corbel S., Chapuis C., Dame T. M., Durouchoux P., 1999, ApJ, 526, L29
Dall'Osso S., Granot J., Piran T., 2012, MNRAS, 422, 2878
D'Elia et al., 2011, GRB Coordinates Network, 12253, 1
De Jahar O. C., Harding A. K., 1992, ApJ, 396, 161
Deller A. T., Camilo F., Reynolds J. E., Halpern J. P., 2012, ApJ, 748, L1
Dermer C. D., 1986, A&A, 157, 223
Drury L. O'C., Aharonian F. A., Völk H. J., 1994, A&A, 287, 959
Duncan R. C., Thompson C., 1992, ApJ, 392, L9
Esposito P. et al., 2013, MNRAS, 429, 3123
Fahlman G. G., Gregory P. C., 1981, Nature, 293, 202
Frail D. A., Goss W. M., Reynoso E. M., Giacani E. B., Green A. J., Otrupcek R., 1996, AJ, 111, 1651
Frail D. A., Claussen M. J., Méhault J., 2013, ApJ, 773, L19
Gabici S., Aharonian F. A., Casanova S., 2009, MNRAS, 396, 1629
Gaensler B. M., Chatterjee S., 2008, GRB Coordinates Network, Circular Service, 8149, 1
Gaensler B. M., Slane P. O., 2006, ARA&A, 44, 17G
Gaensler B. M., Gotthelf E. V., Vasisht G., 1999, ApJ, 526, L37
Gaensler B. M., Slane P. O., Gotthelf E. V., Vasisht G., 2001, ApJ, 559, 963
Gaisser T. K., Protheroe R. J., Stanev T., 1998, ApJ, 492, 219
Gavriil F. P., Kaspi V. M., 2004, ApJ, 609, L67
Gelfand J. D., Slane P. O., Temim T., 2014, Astron. Nachr., 335, 318
Göğüş E., Kouveliotou C., 2011, The Astron. Telegram, 3542, 1
Göğüş E., Woods P. M., Kouveliotou C., Kaneko Y., Gaensler B. M., Chatterjee S., 2010, ApJ, 722, 899
Gold T., 1969, Nature, 221, 25
Goldreich P., Julian W. H., 1969, ApJ, 157, 869G
Goldreich P., Reisenegger A., 1992, ApJ, 395, 250
Gotthelf E. V., Vasisht G., 1998, New Astron., 3, 293
Gotthelf E. V., Vasisht G., Boylan-Kolchin M., Torii K., 2000, ApJ, 542, L37
Göğüş E., Woods P. M., Kouveliotou C., van Paradijs Jan, Briggs M. S., Duncan R. C., Thompson C., 1999, ApJ, 526, L93
Göğüş E., Woods P. M., Kouveliotou C., van Paradijs J., Briggs M. S., Duncan R. C., Thompson C., 2000, ApJ, 532, L121
Granot J. et al., 2006, ApJ, 638, 391
Granot J., Piran T., Bromberg O., Racusin J. L., Daigne F., 2015, Space Sci. Rev., 191, 471
Guilbert P. W., Fabian A. C., Rees M. J., 1983, MNRAS, 205, 593
Guiriec S., Kouveliotou C., van der Horst A. J., 2011, GRB Coordinates Network, 12255, 1
H.E.S.S. Collaboration.2015, A&A, 574A, 27
Halpern J. P., Gotthelf E. V., 2010, ApJ, 710, 941
Harding A. K., Contopoulos I., Kazanas D., 1999, ApJ, 525, L125
Hewitt J. W., Yusef-Zadeh H., Wardle M., 2009, ApJ, 706, L270
Hillas A. M. et al., 1998, ApJ, 503, 744
Ho W. C. G., 2015, MNRAS, 414, 2567
Hurley-Walker N. (AMI Consortium) et al., 2009, MNRAS, 396, 365
Israel G. L. et al., 2016, MNRAS, 457, 3448
Kargaltsev O., Pavlov G. G., 2008, in Bassa C., Wang Z., Cumming A., Kaspi V. M., eds, Am. Inst. Phys. Conf. Ser. Vol. 983, 40 Years of Pulsars: Millisecond Pulsars, Magnetars and More. Am. Inst. Phys., New York, p. 171
Kargaltsev O. et al., 2012, ApJ, 748, 26
Kassim N. E., 1992, AJ, 103, 943
Kennel C. F., Coroniti F. V., 1984, ApJ, 283, 694
Kothes R., Foster T., 2012, ApJ, 746, L4
Kouveliotou C., Kippen M., Woods P., Richardson G., Connaughton V., McCollough M., 1998, IAU Circ. 694
Kuiper L., Hermsen W., 2011, The Astron. Telegram, 3577, 1
Leahy D. A., Tian W. W., 2007, ApJ, A&A, 461, 1013
Leahy D. A., Tian W. W., 2008a, ApJ, 135, 167
Leahy D. A., Tian W. W., 2008b, A&A, 480, L25
Levin L. et al., 2010, ApJ, 721, L33
Li H., Chen Y., 2012, MNRAS, 421, 935
Marshall F. E., Guillemot L., Harding A. K., Martin P., Smith D. A., 2016, ApJ, 827, L39
Mazets E. P., Golentskii S. V., Ilinskii V. N., Aptekar R. L., Guryan I. A., 1979, Nature, 282, 587
Metzger B. D., Margalit B., Kasen D., Quataert E., 2015, MNRAS, 454, 3311
Meyer M., Horns D., Zechlin H.-S., 2010, A&A, 523, A2
Mizuno Y., Lyubarsky Y., Nishikawa K.-I., Hardee P. E., 2011, ApJ, 728, 90
Muslimov A., Page D., 1996, ApJ, 458, 347
Nolan P. L. (Fermi Collaboration) et al., 2012, ApJS, 199, 31

Olausen S. A., Kaspi V. M., 2014, ApJS, 212, 6

Ostriker J. P., Gunn J. E., 1971, ApJ, 164, L95

Pacholczyk A. G., 1970, Series of Books in Astronomy and Astrophysics. Astron. Soc. Pac., San Francisco

Park S., Hughes J. P., Slane P. O., Burrows D. N., Lee J.-J., Mori K., 2012, ApJ, 748, 117

Porter T. A., Strong A. W., 2005, in Acharya B. S., Gupta S., Jagadeesan P., Jain A., Karthikeyan S., Morris S., Tonwar S. Proc. 29th Int. Cosmic Ray Conf. Vol. 4, August 3–10, 2005, Pune, India. Tata Institute of Fundamental Research, Mumbai, p. 77

Porth O., Komissarov S. S., Keppens R. 2013, MNRAS 431, L48

Porth O., Komissarov S. S., Keppens R., 2014, MNRAS, 438, 278

Prieskorn Z., Kaaret P., 2012, ApJ, 755, 1

Reynolds S. P., Chevalier R. A., 1984, ApJ, 278, 630

Reynolds S. P., Gaensler B. M., Bocchino F., 2012, Space Sci. Rev., 166, 231

Rogers A., Safi-Harb S., 2016, MNRAS, 457, 1180

Sarma A. P., Goss W. M., Green A. J., Frail D. A., 1997, ApJ, 483, 335

Shu F. H., 1992, The Physics of Astrophysics: Vol II Gas Dynamics. University Science Books, Mill Valley

Spitkovsky A., 2006, ApJ, 648, L51

Tendulkar S. P., 2013, IAUS, 291, 514

Tendulkar S. P., Cameron P. B., Kulkarni S. R., 2012, ApJ, 761, 76

Tendulkar S. P., Cameron P. B., Kulkarni S. R., 2013, ApJ, 772, 31

Thompson C., Blaes O., 1998, Phys. Rev. D, 57, 3219

Thompson C., Duncan R. C., 1993, ApJ, 408, 194

Thompson D. J., Baldini L., Uchiyama Y., 2012, Astropart. Phys., 39, 22

Tian W. W., Leahy D. A., 2008, MNRAS, 391, 54

Tian W. W., Leahy D. A., 2012, MNRAS, 421, 2593

Tian W. W., Li Z., Leahy D. A., Wang Q. D., 2007, ApJ, 657, L25

Tong H., 2016, RAA, 16, 143

Tong H., Xu R. X., Song L. M., Qiao G. J., 2013, ApJ, 768, 144

Torii K., Kinugasa K., Katayama K., Tsunemi H., Yamauchi S., 1998, ApJ, 503, 843

Turolla R., Zane S., Watts A. L., 2015, Rep. Prog. Phys., 78, 116901

Van der Swaluw E., Achterberg A., Gallant Y. A., Tóth G., 2001, A&A, 380, 309

Vasisht G., Gotthelf E. V., 1997, ApJ, 486, L129

Vasisht G., Gotthelf E. V., Torii K., Gaensler B. M., 2000, ApJ, 542, L49

Watcher S. et al., 2004, ApJ, 615, 887

Woods P. M., Kouveliotou C., Göğüş E., Finger Mark H., Swank J., Markwardt C. B., Hurley K., van der Klis M., 2002, ApJ, 576, 381

Woods P. M., Kouveliotou C., Finger M. H., Göğüş E., Wilson C. A., Patel S. K., Hurley K., Swank J. H., 2007, ApJ, 654, 470

Younes G., Kouveliotou C., Kargaltsev O., Pavlov G. G., Göğüş E., Wachter S., 2012, ApJ, 757, 39

Younes G., Kouveliotou C., Kaspi V. M., 2015, ApJ, 809, 165

Younes G. et al., 2016, ApJ, 824, 138

APPENDIX A: BRAKING INDEX WITH MAGNETIC-FIELD DECAY

Equation (3) for the spin-down law can be generalized to allow for a dependence on the (generally time dependent) surface dipole field $B_s(t)$,

$$\dot{\Omega} = -K B_s^2(t) \Omega^n \iff \dot{P} = (2\pi)^{n-1} K B_s^2(t) P^{2-n}. \quad (A1)$$

This equation reduces to magnetic dipole spin down for $n = 3$ and $K = f R_{NS}^6/(Ic^3)$, and it reduces to equation (3) for a constant B_s. In this case the braking index that is inferred from observation is

$$n' \equiv \frac{\ddot{\Omega}\Omega}{\dot{\Omega}^2} = n + \frac{2\dot{B}_s\Omega}{B_s\dot{\Omega}} \equiv n + \Delta n \quad (A2)$$

where the difference from the standard braking index is given by

$$\Delta n = \frac{2\dot{B}_s\Omega}{B_s\dot{\Omega}} = -\frac{2\dot{B}_s P}{B_s\dot{P}} = -\frac{d\log(B_s^2)}{d\log t}\left(\frac{d\log P}{d\log t}\right)^{-1}. \quad (A3)$$

Note the standard spin-down relation is recovered when $\dot{B}$ vanishes. Also, since $\dot{P} > 0$, a decaying magnetic field ($\dot{B}_s < 0$) yields $\Delta n > 0$. However, since it is hard to measure $\dot{\Omega}$ for the majority of pulsars and especially for magnetars due to large timing noise, n' cannot be measured directly. On the other hand, the standard braking index n can be ascertained by comparing the characteristic spin-down age to that of the host SNR.

Assuming a magnetic-field time evolution of the form[4]

$$B_s(t) = B_0\left(1 + \frac{t}{t_B}\right)^{-1/\alpha} = B_0\tau^{-1/\alpha}, \qquad \frac{d\log(B_s^2)}{d\log\tau} = -\frac{2}{\alpha}, \quad (A4)$$

with some characteristic magnetic-field decay time-scale t_B, where we conveniently define $\tau \equiv 1 + t/t_B$, for which

$$\Delta n = -\frac{d\log(B_s^2)}{d\log\tau}\left(\frac{d\log P}{d\log\tau}\right)^{-1}. \quad (A5)$$

Integrating equation (A1) over time gives

$$\frac{P(t)}{P_0} = \frac{\Omega_0}{\Omega(t)} = \left[1 + \frac{\alpha t_B}{(\alpha-2)t_0}\left(\left\{1 + \frac{t}{t_B}\right\}^{\frac{\alpha-2}{\alpha}} - 1\right)\right]^{\frac{1}{n-1}}$$

$$= \left[1 + \frac{\alpha t_B}{(\alpha-2)t_0}\left(\tau^{\frac{\alpha-2}{\alpha}} - 1\right)\right]^{\frac{1}{n-1}}, \quad \text{for} \quad \alpha \neq 2 \quad (A6)$$

where the initial spin-down time

$$t_0 = \frac{1}{(n-1)KB_0^2}\left(\frac{P_0}{2\pi}\right)^{n-1} = \frac{P_0}{(n-1)\dot{P}}\left(\frac{P}{P_0}\right)^{2-n}$$

$$\times \tau^{-\frac{2}{\alpha}} \to |\alpha| \to \infty \frac{P_0}{(n-1)\dot{P}}\left(\frac{P}{P_0}\right)^{2-n}. \quad (A7)$$

This implies the following spin-down luminosity,

$$L_{sd} = 4\pi^2 I \frac{\dot{P}}{P^3} = L_0\left(\frac{P}{P_0}\right)^{-n-1}\tau^{-\frac{2}{\alpha}} = L_0\left\{1 + \frac{t}{t_B}\right\}^{-\frac{2}{\alpha}}$$

$$\times \left[1 + \frac{\alpha t_B}{(\alpha-2)t_0}\left(\left\{1 + \frac{t}{t_B}\right\}^{\frac{\alpha-2}{\alpha}} - 1\right)\right]^{-\frac{n+1}{n-1}} \quad (A8)$$

where $L_0 = f R_{NS}^6 B_0^2\Omega_0^4/c^3$ for magnetic dipole braking ($n = 3$), and more generally $L_0 = 2E_0/(n-1)t_0$.

A1 Spin-down freezeout

Note that when the magnetic field decays rapidly enough, $\alpha < 2$, the spin down freezes out at late times, and the rotational period approaches a constant asymptotic value (Dall'Osso, Granot & Piran 2012),

$$P_\infty = P_0\left[1 + \frac{\alpha t_B/t_0}{(2-\alpha)}\right]^{\frac{1}{n-1}} \iff P_\infty^{n-1}$$

$$= P_0^{n-1} + \frac{(n-1)KB_0^2\alpha t_B}{(2\pi)^{1-n}(2-\alpha)} \longrightarrow P_\infty^2 = P_0^2 + \frac{8\pi^2 f R_{NS}^6 B_0^2\alpha t_B}{(2-\alpha)Ic^3}. \quad (A9)$$

---

[4] This corresponds to the field decay parametrization of Dall'Osso, Granot & Piran (2012) for $\alpha > 0$ and $t_B \to \tau_{d,i}/\alpha$. They consider only a decay of the magnetic field, and for $\alpha \leq 0$ they obtain a different functional form (exponential decay for $\alpha = 0$ and decay to zero over a finite time for $\alpha < 0$). For our parametrization $\alpha < 0$ corresponds to a growth of the magnetic field, which was not considered by Dall'Osso, Granot & Piran (2012), as such a growth is not expected physically under most scenarios.

Equation (A6) implies

$$\frac{d\log P}{d\log \tau} = \frac{t_B/t_0}{n-1}\,\tau^{\frac{\alpha-2}{\alpha}}\left[1+\frac{\alpha t_B}{(\alpha-2)t_0}\left(\tau^{\frac{\alpha-2}{\alpha}}-1\right)\right]^{-1},$$

$$\text{for}\quad \alpha\neq-2,\qquad \text{(A10)}$$

and a difference from the standard braking index of

$$\Delta n = \frac{2\alpha\Omega^{1-n}}{K B_0^2 t_B}\left(1+\frac{t}{t_B}\right)^{-(2\alpha+1)}$$

$$= (n-1)\frac{2t_0}{\alpha t_B}\,\tau^{\frac{2-\alpha}{\alpha}}\left[1+\frac{\alpha t_B}{(\alpha-2)t_0}\left(\tau^{\frac{\alpha-2}{\alpha}}-1\right)\right].\qquad \text{(A11)}$$

Initially, at $t=0$, we have

$$\Delta n_i = (n-1)\frac{2t_0}{\alpha t_B},\quad n_i' = n+\Delta n_i = n+(n-1)\frac{2t_0}{\alpha t_B}.\qquad \text{(A12)}$$

For $\alpha<2$ at late times the braking index grows as a power law, $n\ll n'\approx\Delta n\propto t^{(2-\alpha)/\alpha}$. For $\alpha>2$ the following asymptotic value is approached at late times,

$$\Delta n_\infty = \frac{2(n-1)}{\alpha-2},\qquad n_\infty' = n+\Delta n_\infty = \frac{n\alpha-2}{\alpha-2}.\qquad \text{(A13)}$$

Equation (A1) corresponds to $\dot{P}\propto B^2 P^{2-n}$, and imposing a magnetic dipole braking spin-down rate for which $\dot{P}\propto B^2 P^{-1}$ corresponds to $n=3$. Under this restriction, for $\alpha>2$ one has

$$n_\infty' = \frac{3\alpha-2}{\alpha-2}\quad\Longleftrightarrow\quad \alpha = \frac{2(n_\infty'-1)}{n_\infty'-3},\qquad \text{(A14)}$$

which corresponds to the scaling of equation (8) under the substitution $n\to n_\infty'$. The evolution of the true braking index $n'=n+\Delta n$ for several representative cases is shown in Fig. A1.
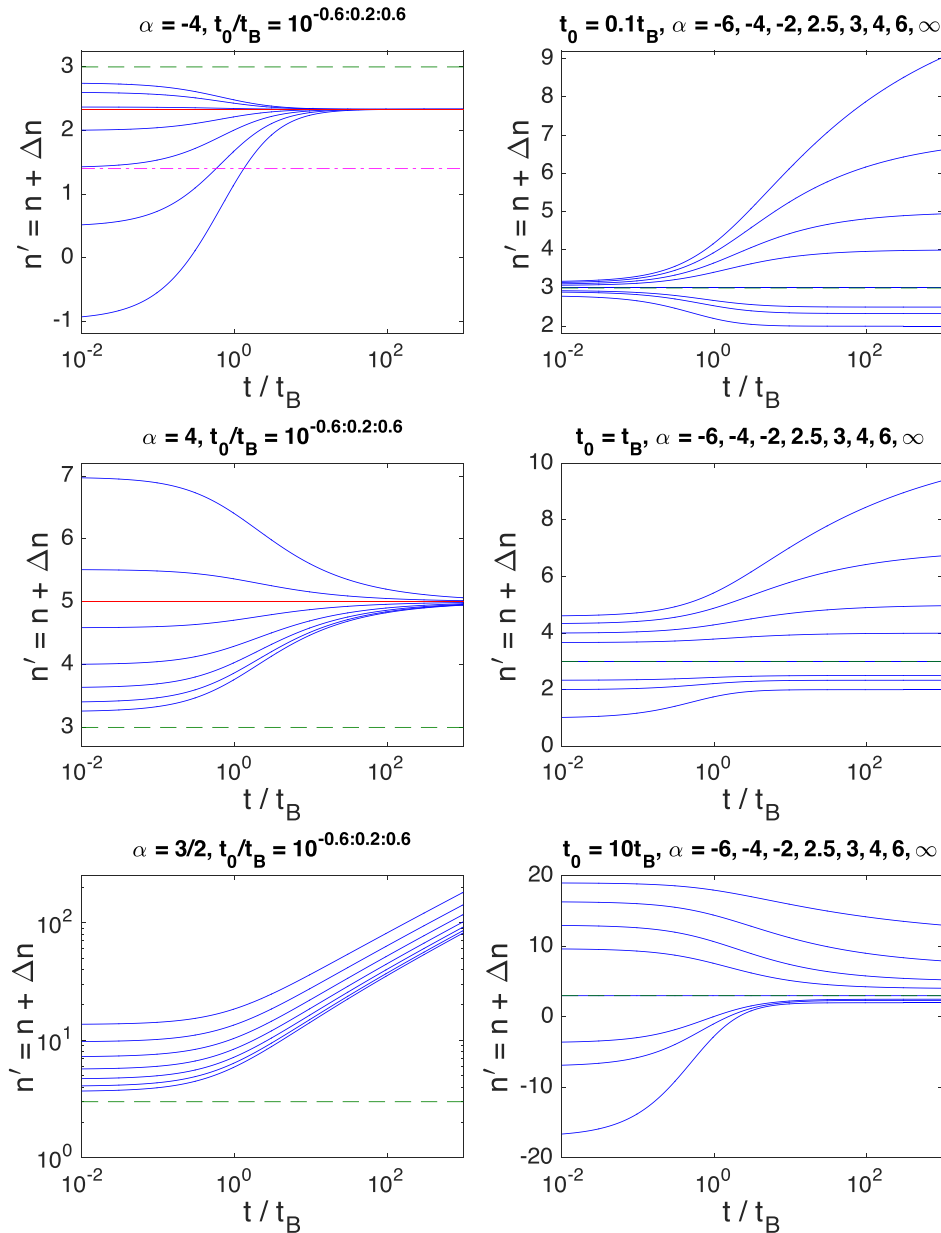
Figure A1. The evolution of the true braking index $n'=n+\Delta n$ as a function of t/t_B is shown for several representative cases, with $n=3$ and varying t_0/t_B and α.
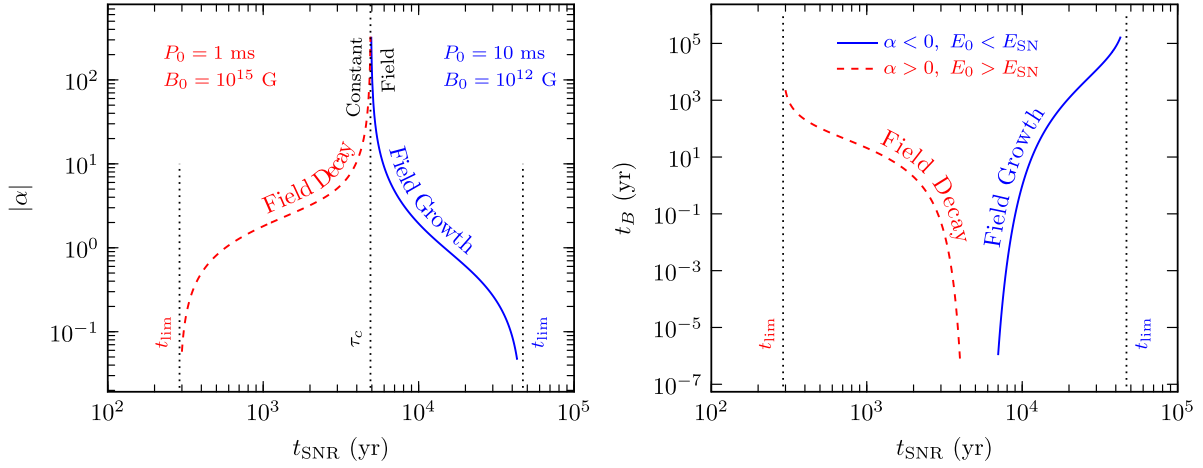
Figure A2. Left: magnetic-field power-law index as a function of the age of the system t_{SNR} for $n = 3$ and $f = 1$. Solid line: the magnetar is born as an ordinary NS whose surface magnetic field grows over its lifetime to the currently inferred value $B_s = 1.16 \times 10^{14}$ G from P and $\dot{P}$. Here $\alpha < 0$, but we plot $|\alpha|$ for clarity. Dashed line: The magnetar is born as a fast rotator with $P_{0,-3} = 1$ and strong surface field $B_0 = 10^{15}$ G which decays over its lifetime to the current surface field B_s. In both scenarios, $|\alpha| \to \infty$ at $t_{SNR} = \tau_c = 4.9$ kyr for which the surface field remains constant at its initial value, $B_s(t) = B_0$. Right: magnetic-field decay/growth time t_B as a function of the age of the system t_{SNR} for the two cases shown on the left. The vertical dashed lines show the limiting value of t_{SNR} for $|\alpha| \to 0$ from equation (A16).

A2 Solving for α and t_B

A useful constraint on the magnetic-field decay index α can be obtained by using the present spin period and inferred surface magnetic field of Swift J1834. By using the magnetic-field time evolution from equation (A4) and the time evolution of the spin period, equation (A6) can be cast into the following form:

$$\frac{P(t)}{P_0}$$

$$= \left[1 + \left\{ \left(\frac{B_s}{B_0} \right)^{-\alpha} - 1 \right\}^{-1} \frac{\alpha t}{(\alpha - 2)t_0} \left\{ \left(\frac{B_s}{B_0} \right)^{2-\alpha} - 1 \right\} \right]^{\frac{1}{n-1}}.$$
(A15)

Here we look at two scenarios and assume standard magnetic dipole braking with $n = 3$: (i) the magnetar begins its life as a regular pulsar with initial spin period $P_0 \sim 10$ ms and surface magnetic field $B_0 \sim 10^{12}$ G, but experiences a growth in surface field by the time $t = t_{SNR}$, or (ii) the proto-NS is a rapid rotator with $P_0 \sim 1$ ms and quickly ramps up its surface magnetic field under the action of the α–ω dynamo mechanism, so that $B_0 \sim 10^{15}$ G, which then decays over the age of the system to its current value. In Fig. A2 we solve equation (A15) for α given that the current spin period $P = 2.48$ s and the surface magnetic field is that inferred from P and $\dot{P}$, $B_s = 1.16 \times 10^{14} f^{-1/2}$ G.

In both cases, as $|\alpha| \ll 1$, the age of the system t_{SNR} in equation (A15) approaches a limiting value for a given set of (P_0, P, B_0, B_s, n) parameters

$$t_{lim} = t_{SNR}(|\alpha| \to 0)$$

$$= 2t_0 \ln \left(\frac{B_s}{B_0} \right) \left[\left(\frac{B_s}{B_0} \right)^2 - 1 \right]^{-1} \left[\left(\frac{P}{P_0} \right)^{n-1} - 1 \right], \quad \text{(A16)}$$

which corresponds to $t_B \to \infty$. In the opposite limit, as $\alpha \to \pm\infty$, which implies constant surface field $B_s(t) = B_0$, $t_B \to 0$ and the age of the system approaches the characteristic age $t_{SNR} \to \tau_c = 4.9$ kyr. We show the values of t_{lim} for different parameter values in Fig. A3.
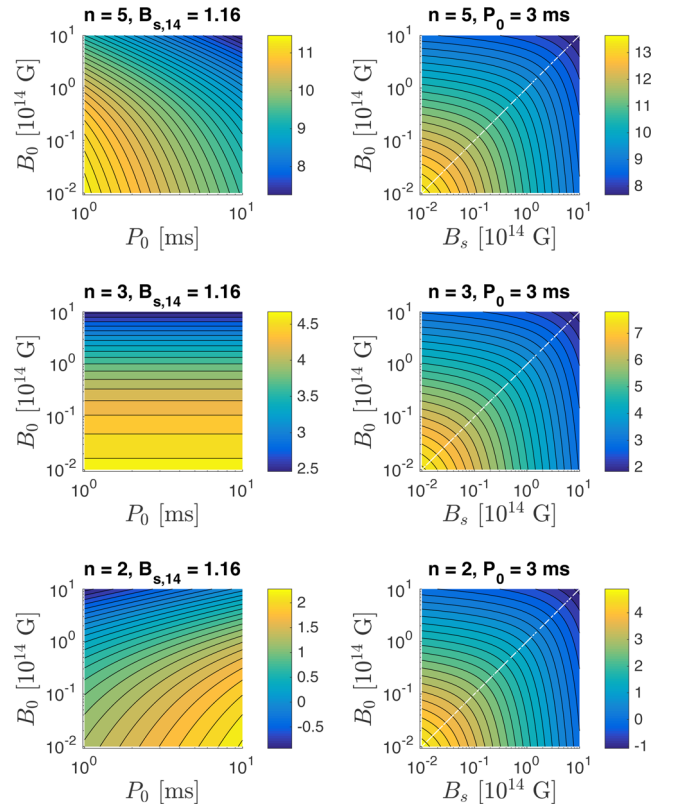
Figure A3. Contour plots of $\log_{10}(t_{lim}[\text{yr}])$ for the limiting time given in equation (A16) for different values of the relevant parameters. The remaining parameters are fixed to their fiducial values from the main text.

The constraint on α can be further used to constrain the characteristic field decay/growth time t_B, as shown in Fig. A2, using

$$\frac{t_B}{t_{SNR}} = \left[\left(\frac{B_s}{B_0} \right)^{-\alpha} - 1 \right]^{-1}. \quad \text{(A17)}$$

For $\alpha > 0$, the corresponding field decay time can be much shorter than 10^3 yr; however, such short decay times are unphysical. Field decay in magnetars is believed to be occurring in their crust due to Hall drift or Ohmic decay modes for which the characteristic decay time is $t_B \sim 10^3$–10^5 yr (e.g. Goldreich & Reisenegger 1992).

APPENDIX B: MAGNETAR WIND NEBULA DYNAMICAL EVOLUTION

We consider the expansion of the MWN inside the freely expanding SNR and its interaction with the ISM. This depends on the density profile of the unshocked SN ejecta and on the details of how energy is exchanged between it and the shocked magnetar wind. Radiative losses play an important role; however for simplicity we only consider the adiabatic expansion of the nebula. Following Blondin et al. (2001), the density can be modelled as two components, separated by a transition radius $r_t = v_t t$, with a spatially flat inner profile given by

$$\rho_{ej}(r, t) = \frac{5q - 25}{2\pi q} E_{SN} v_t^{-5} t^{-3} \qquad \text{for} \quad r < v_t t \tag{B1}$$

and a steep outer profile with $\rho_{ej} \propto r^{-q} t^{q-3}$; we use $q = 10$ as a fiducial index. The ejecta expands ballistically with transition velocity

$$v_t = \left(\frac{10q - 50}{3q - 9} \frac{E_{SN}}{M_{ej}} \right)^{1/2} = 6.3 \times 10^8 E_{SN,51}^{1/2} M_3^{-1/2} \, \text{cm s}^{-1}. \tag{B2}$$

The kinetic energy of the expanding density core

$$E_c = \frac{1}{2} M_c v_t^2 = \left(\frac{q - 5}{q} \right) E_{SN} = \frac{1}{2} E_{SN} \tag{B3}$$

delineates the two scenarios in which the magnetar is either energetically dominant ($E_0 > E_c$) and significantly alters the dynamical evolution of the SNR or sub-dominant ($E_0 < E_c$) and mirrors the standard case of PWNe.

B1 $E_0 > E_c$

The magnetar continues to inject energy for $t < t_0$, and the initial expansion of the MWN is the same for both cases. Ignoring radiative losses, the expansion of the MWN in the *thin-shell* approximation is governed by (e.g. Ostriker & Gunn 1971; Reynolds & Chevalier 1984)

$$LR = \frac{d}{dt}(4\pi p R^4) \tag{B4}$$

$$M_s \ddot{R} = 4\pi R^2 [p - \rho_{ej}(\dot{R} - v_{ej})^2] \tag{B5}$$

where R and p are the radius and pressure inside the MWN, M_s is the swept up ejecta mass, and $L = L_0$ for $t < t_0$ is the power injected by the magnetar. With radius expanding as a power law in time $R \propto t^a$, the internal energy of the MWN increases linearly with time

$$U = 4\pi R^3 p = \frac{L_0 t}{a + 1}. \tag{B6}$$

Using this result in equation (B5) and noting that $v_{ej} = R/t$ for $v_{ej} < v_t$ give $a = 6/5$ (Reynolds & Chevalier 1984; Blondin et al. 2001). The spinning down magnetar injects most of its rotational energy E_0 at $t \sim t_0$, and if $E_0 \gtrsim E_c$, the evolution of the MWN will be significantly different from what is generally observed for PWNe. Whether this is indeed the case can be learned by comparing t_c, the

time at which the MWN reaches the edge of the density core, to t_0, the time after which the rate of energy injection by the magnetar decreases significantly. Then, for $R(t) = R_t = v_t t$, the core crossing time and radius are (Blondin et al. 2001)

$$\frac{t_c}{t_0} = 2.64 \left(\frac{q - 5}{q} \right) \left(\frac{n - 1}{2} \right)$$

$$\frac{E_{SN}}{E_0} = 0.07 \left(\frac{n - 1}{2} \right) P_{0,-3}^2 E_{SN,51} \tag{B7}$$

$$R_c = v_t t_c = 2.64 \left(\frac{n - 1}{2} \right) \left(\frac{q - 5}{q} \right) \left(\frac{10q - 50}{3q - 9} \frac{E_{SN}^3}{M_{ej}} \right)^{1/2}$$

$$\frac{t_0}{E_0} = 1.4 \times 10^{12} P_{0,-3}^4 E_{SN,51}^{3/2} f^{-1} B_{14}^{-2} M_3^{-1/2} \, \text{cm} \tag{B8}$$

For $t < t_c$, the ejecta mass will accumulate in a thin shell at the contact discontinuity that separates the relativistically hot MWN gas and the unshocked SNR ejecta, with its radius growing as

$$R(t) = R_c \left(\frac{t}{t_c} \right)^{6/5}. \tag{B9}$$

For $t_0 > t > t_c$, the expansion of the MWN will accelerate down the steep density gradient while it is still being energized by the magnetar. At this point the swept up mass $\sim M_{ej}$ and it can be shown that the radius of the MWN will grow as (Reynolds & Chevalier 1984)

$$R(t) = R_c \left(\frac{t}{t_c} \right)^{3/2}. \tag{B10}$$

At this point, the dynamical evolution of the SNR differs from the canonical case of a point explosion with no further energy injection. Here the SNR volume is replaced by that of the MWN and the forward blast wave continues to accelerate in the ISM until $t = t_0$. Here, it should be noted that the contact discontinuity between the relativistically hot bubble and the unshocked ISM is highly susceptible to its fragmentation by the Rayleigh–Taylor instability. Consequently, the hot gas will escape through gaps in the fragmented shell and directly interact with the cold ISM. The treatment of this phase is out of the scope of this work and is left for future study.

The MWN blast wave will begin to coast at a constant velocity for $t > t_0$ until the onset of the Sedov–Taylor phase, with

$$R(t) = R_0 \left(\frac{t}{t_0} \right) \tag{B11}$$

where

$$R_0 = \left[\frac{1}{2.64} \left(\frac{2}{n - 1} \right) \left(\frac{q}{q - 5} \right) \left(\frac{10q - 50}{3q - 9} \right) \frac{E_0}{M_{ej}} \right]^{1/2}$$

$$t_0 = 8.3 \times 10^{13} f^{-1} B_{14}^{-2} P_{0,-3} M_3^{-1/2} \, \text{cm}. \tag{B12}$$

B2 $E_0 < E_c$

In this case, the energy injected by the magnetar is not large enough and the MWN never crosses the entire density core, such that $t_0 < t_c$, which translates into a lower bound on the initial spin period and an upper bound on E_0

$$P_0 > 4.1 \left[\frac{n - 1}{2} E_{SN,51} \right]^{-1/2} \, \text{ms} \tag{B13}$$

$$E_0 < 1.2 \times 10^{51} \left(\frac{n-1}{2} \right) E_{\mathrm{SN},51} \, \mathrm{erg}. \tag{B14}$$

This limit is larger (unless $n > 4$) than the upper bound of $P_0 \lesssim 3$ ms conjectured by Duncan & Thompson (1992) and Thompson & Duncan (1993) for the formation of a magnetar by magnetic-field amplification through the action of an $\alpha - \omega$ dynamo, which would operate in the convective and differentially rotating cores of rapidly spinning proto-NSs. However, as shown in Appendix A, magnetic-field decay, which powers the high quiescent luminosity and bursting activity in magnetars, tends to produce high braking indices, $n > 3$. On the other hand, if $n < 3$ then it is unclear how the pulsar evolves into a magnetar. In this case, the wind nebula and its interaction with the SNR ejecta would proceed in a way much similar to the canonical case of PWNe, where its size would grow as

$$R(t) = R_0 \left(\frac{t}{t_0} \right)^a \tag{B15}$$

where $a = 6/5$ for $t < t_0$ and $a = 1$ thereafter, until it is crushed by the reverse shock (Blondin et al. 2001), with

$$R_0 = 1.50 \left(\frac{2q}{(q-5)(n-1)} \right)^{\frac{1}{5}} \left(\frac{q-5}{q-3} \right)^{\frac{1}{2}} \left(\frac{E_{\mathrm{SN}}^3 E_0^2}{M_{\mathrm{ej}}^5} \right)^{\frac{1}{10}}$$

$$t_0 = 1.5 \times 10^{15} E_{\mathrm{SN},51}^{\frac{3}{10}} M_3^{-\frac{1}{2}} f^{-1} B_{14}^{-2} P_{0,-2}^{8/5} \, \mathrm{cm} \tag{B16}$$

where $R_0 < v_t t_0$.

APPENDIX C: ADIABATIC AND RADIATIVE ENERGY LOSSES

Electrons injected at the termination shock R_{TS} with energy $\gamma_{\mathrm{e},i} m_e c^2$ at time t_i lose energy to adiabatic expansion of the nebular volume and synchrotron radiation. Their energy evolves in time according to equation (51), which can be written in terms of the adiabatic expansion or radius-doubling time, $t_{\mathrm{ad}}(t) = t/a$, and the synchrotron cooling time, $t_{\mathrm{syn}}(\gamma_e, t) = t_{c,0}(t)/\gamma_e$ where $t_{c,0}(t) = 1/[bB^2(t)] = 6\pi m_e c/[\sigma_T B^2(t)]$,
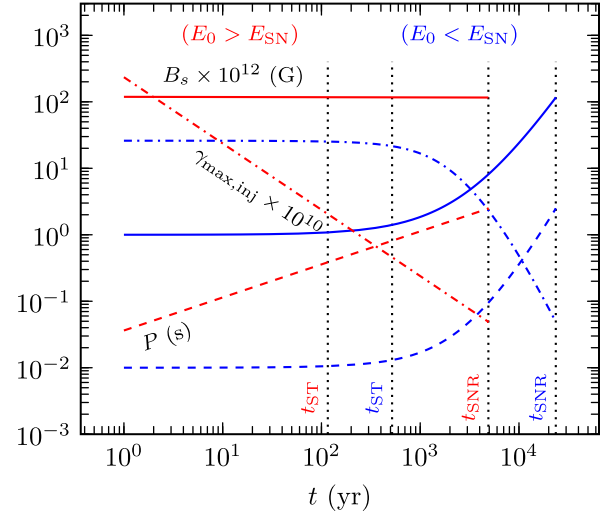
$$\frac{\mathrm{d} \ln \gamma_e}{\mathrm{d}t} = -\frac{1}{t_{\mathrm{ad}}(t)} - \frac{1}{t_{\mathrm{syn}}(\gamma_e, t)} = -\frac{a}{t} - \frac{\gamma_e}{t_{c,0}(t)}. \tag{C1}$$

After being compressed by the reverse shock and after establishing pressure equilibrium with the SNR, the MWN re-expands slowly as a power law in time given by equation (44), with $a = 3/2(5 - k)$, i.e. $R(t > t_{\mathrm{ST}})/R_f = (t/t_{\mathrm{ST}})^a$. Therefore, the magnetic field in the nebula for a constant σ scales as its energy density, $B^2 \propto E/R^3 \propto R^{-4} \propto t^{-4a}$ so that $B^2(t) = B_{\mathrm{ST}}^2(t/t_{\mathrm{ST}})^{-4a}$ where $B_{\mathrm{ST}} = B(t_{\mathrm{ST}})$, and $t_{c,0}(t) = t_{c,0}(t_{\mathrm{ST}})(t/t_{\mathrm{ST}})^{4a}$. For injection times $t_i > t_{\mathrm{ST}}$ equation (C1) can be solved analytically by switching variables to $y(t) = \gamma_e(t)^{-1}$,

$$\frac{\mathrm{d}y}{\mathrm{d}t} = \frac{a}{t} y + \frac{1}{t_{c,0}(t)}. \tag{C2}$$

The solution to the above equation for an initial value $y(t_i) = y_i = 1/\gamma_i$ is

$$y(t_i, t, y_i) = t^a \left[y_i t_i^{-a} + I(t_i, t) \right], \tag{C3}$$

where γ_i is the initial Lorentz factor of the electron injected into the nebula at R_{TS} at injection time t_i, and

$$I(t_i, t) = \int_{t_i}^t \frac{t'^{-a} \mathrm{d}t'}{t_{c,0}(t')} = \frac{t_{\mathrm{ST}}^{4a}}{t_{c,0}(t_{\mathrm{ST}})} \left(\frac{t_i^{1-5a} - t^{1-5a}}{5a - 1} \right),$$

$$t^a I(t_i, t) = \frac{t}{t_{c,0}(t)} \left[\frac{\left(\frac{t}{t_i} \right)^{5a-1} - 1}{5a - 1} \right]. \tag{C4}$$

This solution can be expressed back in terms of γ_e,

$$\gamma_e(t_i, t, \gamma_i) = \gamma_i \left(\frac{t}{t_i} \right)^{-a} \left[1 + \frac{t_i}{t_{\mathrm{syn}}(\gamma_i, t_i)} \left(\frac{1 - \left(\frac{t}{t_i} \right)^{1-5a}}{5a - 1} \right) \right]^{-1}$$

$$= \gamma_i \left[\left(\frac{t}{t_i} \right)^a + \frac{t}{t_{\mathrm{syn}}(\gamma_i, t)} \left(\frac{\left(\frac{t}{t_i} \right)^{5a-1} - 1}{5a - 1} \right) \right]^{-1}. \tag{C5}$$

It is of relevance here to only look at the cooling evolution of the maximum energy electrons that were injected at time $t_i > t_{\mathrm{ST}}$. The maximum injection energy depends on the strength of the surface magnetic field and the spin period at time of injection, as given in equation (92),

$$\gamma_{\max} = 2.6 \times 10^9 B_{14} P_{\mathrm{sec}}^{-2} \tag{C6}$$

In Fig. C1, we show the evolution of the surface magnetic field, spin period, and maximum Lorentz factor of electrons injected into the nebula after the crushing and during the re-expansion phase for $t > t_{\mathrm{ST}}$. We show the spin-down evolution for two cases. (a) When $E_0 > E_{\mathrm{SN}}$, the magnetar is assumed to have been born rotating very fast with initial spin period $P_0 = 1$ ms and initial surface field $B_0 = B_s = 1.16 \times 10^{14}$ G (assuming $f = 1$). From Fig. A2, it is clear

Figure C1. Evolution of the surface magnetic field B_s (solid), spin period P (dashed), and maximum Lorentz factor of injected electrons $g_{\max}$ (dot–dashed). The *red* lines correspond to the case where $E_0 > E_{\mathrm{SN}}$ with initial $P_0 = 1$ ms, constant surface field $B_s = B_0 = 1.16 \times 10^{14}$ G as inferred from the measured P and $\dot{P}$, and system age $t_{\mathrm{SNR}} = \tau_c = 4.9$ kyr. The *blue* lines are for the case where $E_0 < E_{\mathrm{SN}}$ with initial $P_0 = 10$ ms, initial surface field $B_0 = 10^{12}$ G which then grows to the current surface field over the system age $t_{\mathrm{SNR}} = 23.6$ kyr (see equation 2). The dotted lines show the Sedov–Taylor times t_{ST} and system ages for the two cases. Other assumed parameters are: $n = 3$, $n_{\mathrm{ext}} = 1\,\mathrm{cm}^{-3}$, $M_{\mathrm{ej}} = 3\mathrm{M}_\odot$, $E_{\mathrm{SN}} = 10^{51}$ erg, $f = 1$.

that any field decay scenario predicts $t_{\mathrm{SNR}} < \tau_{\mathrm{c}}$, which implies that the object has to be very young. Moreover, physical field decay time-scales $t_B \gtrsim 10^3$ are only obtained when $t_{\mathrm{SNR}} \lesssim 400\,\mathrm{yr}$. However, this age estimate is in strong contradiction with the age estimate derived in equation (2) based on the current size of the radio SNR. Therefore, one is forced to consider a constant surface field scenario (with the alternative being the field growth case) with $t_{\mathrm{SNR}} = \tau_{\mathrm{c}} = 4.9\,\mathrm{kyr}$. (b) When $E_0 < E_{\mathrm{SN}}$, we consider the field growth scenario

where the magnetar has initial spin period $P_0 = 10\,\mathrm{ms}$ and surface field $B_0 = 10^{12}\,\mathrm{G}$. Over the age of the system $t_{\mathrm{SNR}} = 23.6\,\mathrm{kyr}$ (see equation 2 for the choice of age), the surface field and spin period of the magnetar grow to the currently measured values.

This paper has been typeset from a TEX/LATEX file prepared by the author.